8-2019

Unveiling the Cosmic History of Light

Abhishek Amitbhai Desai
Clemson University, abhishd@g.clemson.edu

Unveiling the cosmic history of Light

A Dissertation
Presented to
the Graduate School of
Clemson University

In Partial Fulfillment
of the Requirements for the Degree
Doctor of Philosophy
Physics and Astronomy

---

by
Abhishek A. Desai
August 2019

Accepted by:
Dr. Marco Ajello, Committee Chair
Dr. Dieter Hartmann
Dr. Bradley Meyer
Dr. Gerald Lehmacher

Abstract

The Universe was created with a Big Bang ∼13.7 billion years ago while the first stars and galaxies came after ∼400 million years. All the light that was ever emitted in the Universe at ultraviolet, optical, and infrared wavelengths from the period of those first stars till present date makes up the Extragalactic Background Light (EBL). This diffuse background interacts with photons emitted by distant high energy sources, in the GeV and TeV regime, via photon-photon interaction annihilating the high energy photon and producing an electron-positron pair. This gives researchers a powerful and highly effective technique to study the EBL by analyzing the imprint it leaves on the spectra of distant gamma-ray sources. For my PhD thesis project, I made use of this method to study the attenuated spectra of two major high energy sources - gamma ray bursts and active galactic nuclei - observed using the *Fermi*-Large Area Telescope and Cherenkov Telescopes. While similar studies have been performed in the past, most of the derived measurements came from just scaling the optical depth due to the EBL according to the observed spectra, making the estimated EBL spectral intensity uncertain. To tackle this, we have recently developed a dedicated technique which deconvolves the EBL into smaller energy and redshift bins. Using this technique along with an extensive GeV+TeV source sample, we were able to obtain the first homogeneous set of measurements of the EBL spectral intensity covering the UV-IR wavelengths. Additionally, we used this result to investigate several, still debated, astrophysical topics like measurements of the star formation history of the Universe, Hubble constant (H_0) and matter density (Ω_m).

Dedication

I would like to dedicate my work to my father, *Amit Desai* for inspiring me to pursue my dreams; my mother *Jyoti Desai* for her constant loving care and motivation; and my sister *Shwetangi* for standing by me and believing in me.

Acknowledgments

I would like to thank primarily my advisor, *Dr. Marco Ajello*, for introducing me to this ever-interesting topic and for imparting the valuable knowledge and experience needed for working on this research. I would like to thank, *Dr. Dieter Hartmann*, for being an excellent critic allowing me to improve my work at every stage, *Dr. Gerald Lehmacher* for giving me an opportunity to work with him and for briefly introducing me to the world of Atmospheric research and my professors *Dr. Bradley Meyer*, *Dr. Catalina Marinescu* for teaching me the important concepts of Physics. I am also grateful to *Dr. Alberto Dominiguez*, *Dr. Kari Helgason* and *Dr. Justin Finke* for their tremendous work and efforts while collaborating with me in all my research projects. I would like to specially thank *Dr. Vaidehi Paliya* for helping me understand many core concepts of astrophysics and for the consistent motivation required to pursue new research areas. I would also like to mention my friends: Argo, Achyut, Bishwambhar, Ethan, Stefano, Samalka, Maxwell, Lea, Aman, Nayere and Shantanu without whom this journey would not be the same. Finally I would like to thank the most, my complete family including my uncles, aunts and cousins for their love and support.

Contents

Title Page . . . . . **i**

Abstract . . . . . **ii**

Dedication . . . . . **iii**

Acknowledgments . . . . . **iv**

List of Tables . . . . . **vii**

List of Figures . . . . . **viii**

1 Introduction **1**
1.1 The History of the Universe 1
1.2 Cosmic background radiation 3
1.3 Extragalactic Background Light 6
1.4 EBL intensity measurement 7

2 Measurement of the EBL **10**
2.1 Direct Measurements 11
2.2 Galaxy Surveys 13
2.3 Indirect Measurements 15

3 Instruments **21**
3.1 *Fermi*-LAT 21
3.2 Cherenkov telescopes 26
3.3 CTA 28

4 EBL measurement using GRB **29**
4.1 Introduction 29
4.2 Data Analysis 32
4.3 EBL Study 36
4.4 Tests for Systematic Effects 38
4.5 Conclusion 42

5 EBL measurements using AGN observed using the*Fermi*-LAT **52**
5.1 Main Text of Article 53

5.2 Supplementary Materials 62

6 EBL measurements using AGN observed using Cherenkov Telescopes . 96
6.1 Introduction 96
6.2 Analysis 98
6.3 Reconstructing the EBL 101
6.4 Discussion 104

7 Redshift measurements of AGN 108
7.1 Introduction 108
7.2 Sample Selection 110
7.3 Observations and Data Analysis 111
7.4 Spectral Analysis 112
7.5 Conclusion 115

8 Conclusions and Discussion 123

Appendices 128
A Abbreviations used 129
B EBL attenuation brief overview 132
C Cosmology concepts used in this work 136

List of Tables

4.1 GRB used for analysis (GRBs are sorted increasingly by the time of the event) 47
4.2 Photons detected by the *Fermi*-LAT at an optical depth greater than 0.1 . . 48
4.3 Joint-likelihood results for different EBL models using GRB sources. 49
4.4 Combined results of GRB and BL Lac sources for different EBL models. . . . 50

5.1 Criteria, optimized on simulations, adopted to choose a spectral model. . . . 65
5.2 Joint-likelihood results for different EBL models ordered by decreasing value of the last column. 68
5.3 EBL Optical Depths $\tau_{\gamma\gamma}$ in bins of redshift and energy as reported in Figure 5.7. 72
5.4 Spectral intensity[a] (λI_λ) of the EBL as a function of redshift and wavelengths as reported in Figure 6.3. 85
5.5 The Cosmic star-formation history as reported in Figure 5.3. 91

6.1 Results of EBL models tested using VHE data 100

7.1 List of sources and their properties sorted in the order of increasing R.A. (Right ascension) values. (1): 3FHL catalog (Ajello et al., 2017) name for the source. (2): optical, IR, X-ray or radio counterpart of the source. (3) Right ascension. (4) Declination. (5) $E(B-V)$ value obtained using the measurements of Schlafly & Finkbeiner (2011) and the NASA/IPAC Infrared Science Archive online tool. (6) V band magnitude. (7) Date of observation. (8) Exposure time (in seconds).(9)Slope of continuum fit obtained from the observed fits file 117
7.2 Results obtained from spectral analysis discussed in Section 7.4. The redshift measurement values marked with a * are tentative z measurements. 118

List of Figures

1.1 Timeline of the Universe . . . 2
1.2 Intensity of the cosmic background radiation . . . 4
1.3 EBL intensity as predicted by EBL models . . . 8

2.1 EBL intensity measurements . . . 11
2.2 IGL measurements of the EBL . . . 14
2.3 Attenuation due to EBL . . . 15
2.4 EBL opacity as a function of energy and redshift . . . 17
2.5 Unified AGN model . . . 18

3.1 Schematic view of GBM on *Fermi* . . . 23
3.2 Schematic view of LAT on *Fermi* . . . 24
3.3 Fermi LAT all sky gamma ray map . . . 25
3.4 Working of a Cherenkov Telescope . . . 26

4.1 Redshift distribution of used GRB sample . . . 33
4.2 Cosmic Gamma ray Horizon plot . . . 34
4.3 Individual and Stacked TS vs b curve of GRBs . . . 39
4.4 Optical Depth constraints using GRB . . . 43
4.5 Renormalized EBL model predictions using GRB results . . . 45
4.6 Distribution obtained from simulations of the ΔTS . . . 51

5.1 The Cosmic Gamma Ray Horizon (Updated) . . . 56
5.2 EBL spectral intensity and its evolution . . . 57
5.3 Derived Cosmic Star Formation Rate History . . . 59
5.4 Derived limits on the UV luminosity density . . . 60
5.5 Redshift distribution of blazar Sample . . . 64
5.6 Stacked TS vs b curve obtained from blazar sample . . . 67
5.7 Optical depth measurements from *Fermi*-LAT data . . . 70
5.8 GRB 080916C Spectrum . . . 73
5.9 Stacked TS vs b curve of Blazars in Monte Carlo Simulations . . . 74
5.10 Impact of time resolved analysis for Blazar sample . . . 76
5.11 Derived cosmic emissivity . . . 81
5.12 EBL SED at redshift z=0 . . . 83
5.13 Evolution of cosmic emissivity . . . 88
5.14 The effects of dust extinction on the derived SFH . . . 93
5.15 The star-formation history of the Universe . . . 94

5.16 Ratio of emissivities of AGN vs total emission at 0.16 μm 95

6.1 Stacked TS profile for TeV Blazars and derivation of optical depth 99
6.2 Redshift binned optical depth measurements derived using GeV and TeV blazar data 101
6.3 EBL SED at redshift z=0 updated using GeV+TeV+IGL 102
6.4 The build-up of the local EBL 105

7.1 Normalized V-band magnitude distribution of blazar sample used for redshift determination 116
7.2 Optical spectra of the observed candidates 119
7.2 Continued from Fig 7.2 120
7.2 Continued from Fig 7.2 121
7.3 Zoomed ptical spectra of the observed candidates 122

8.1 Measurement of the Hubble constant and matter density using EBL attenuation measurements 126
1 Above plot depicts $\sigma_{\gamma\gamma}$ as a function of increasing β. 133
2 Intensity of the optical component of the EBL modeled using a diluted blacbody function. 134
3 Photon density of the EBL in the optical regime, modeled using the EBL intensity shown in Figure 2. 134
4 Optical depth of the EBL computed using the modeled intensity and number density. 134
5 Comparison of an attenuated and unattenuated gamma ray spectrum. The unattenuated spectrum is modeled using a simple Power Law. 135

Chapter 1

Introduction

1.1 The History of the Universe

The standard Big Bang model states that the universe began from an extremely hot and dense point about ∼13.7 billion years ago. In a short period of $\sim 10^{-35}$ seconds, the Universe inflated at an astonishing rate ($\sim 10^{26}$ times). This period of the Universe that took place after the Big Bang is known as inflation. After inflation, the Universe was a hot dense concoction of particles like electrons and quarks which gradually cooled to form the first protons and neutrons. These protons and neutrons then combined together about three minutes after the Big Bang when its temperature was $\sim 10^{9}$ K, dubbed as the era of neucleosynthesis, to form the first hydrogen and helium nuclei.

Soon after the formation of the first hydrogen and helium nuclei, the first neutral atoms were formed, however due to the energetic radiation the atoms were fully ionized. After about $\sim 375,000$ years from the Big Bang the Universe cooled enough to a temperature of ~ 3000 K for the electrons to bind to the atomic nuclei allowing ionized hydrogen and helium to recombine with electrons. During this period of recombination, the Universe became neutral, which enabled the trapped radiation left over from the Big Bang to be seen allowing researchers to measure the redshift (z) of the era to be equal to $z = 1100$. This radiation is known as the Cosmic Microwave Background (CMB). After the recombination

era the Universe entered a period called the "Cosmic Dark age" as the first stars and galaxies were yet to form. The Cosmic Dark age ended after ∼400 million years and at z ∼20 when the first stars were formed. During this period, known as the epoch of reionization, the neutral intergalactic medium was reionized due to the formation of the first stars which then led the Universe to become transparent to light. After the epoch (i.e. z ∼6) the Universe cooled down and expanded even further forming more stars and galaxies with a peak in star formation activity at $z \sim 2$, followed by a decline down to the present day). The timeline of the universe from the inflation till present day is shown in Figure 1.1.

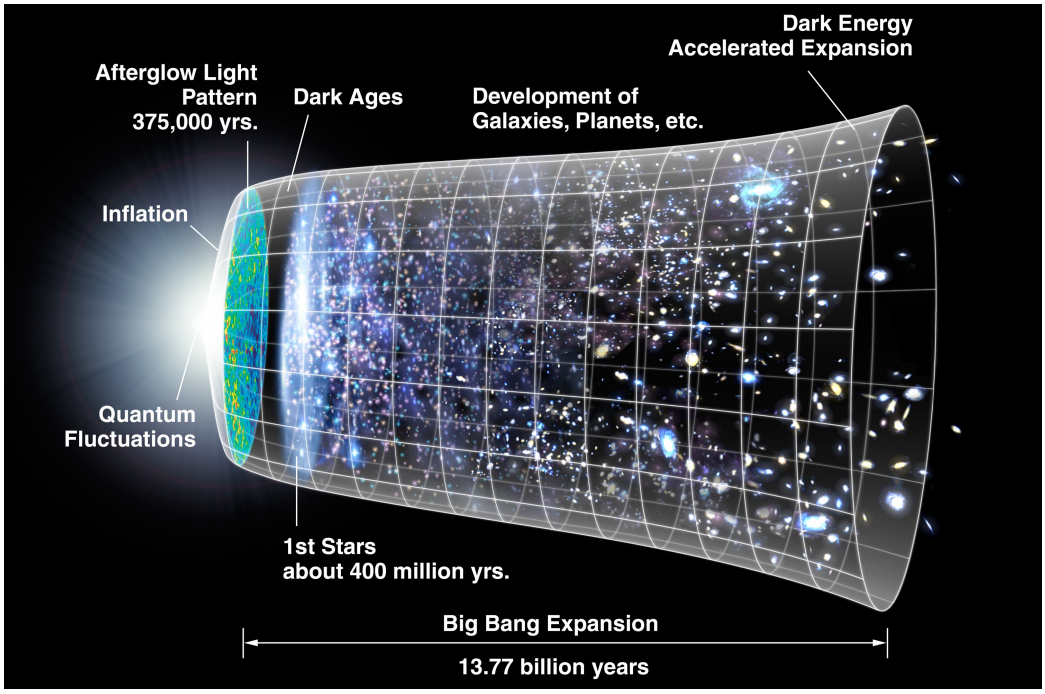

Figure 1.1 A diagram showing the history of the Universe. Credit: NASA/WMAP Science Team.

While the evidence of the early Universe is obtained from the study of the CMB, the processes that took place during the epoch of reionization are only partially understood due to a lack of observations. While recent telescopes have been able to observe amazing

distances, direct detections have not been able to provide us with a complete knowledge of the early Universe, yet. For example, the farthest known galaxy, GN-z11, was seen at a redshift of $z \sim 11$ by the NASA's Hubble Space Telescope meaning it was present only 400 million years after the Big Bang (and 13.4 billion years in the past). However the process of formation of GN-z11 is still unclear. While a fresh look using the highly anticipated James Webb Space Telescope (JWST) will shed light on this mystery (see Oesch et al., 2016), a simpler ready to use tool to study this early period of time is making use of the cosmic background radiation (CBR) which is defined as all the collective electromagnetic radiation over the whole spectrum ever radiated from the Big Bang to present time. The next section describes various components of the CBR and how studying them will help us understand the early Universe.

1.2 Cosmic background radiation

The collective diffuse emission over the history of the Universe forms the cosmic background. The cosmic background in subdivided into predominantly five major components: 1. Cosmic radio background (CRB); 2. Cosmic Microwave Background (CMB); 3. Extragalactic Background Light (EBL) made up of cosmic infrared/optical/ultraviolet background (CIB/COB/CUB); 4. Cosmic X ray background (CXB) and 5. Cosmic gamma ray background (CGB). The intensity of the CBR and all its components can be seen graphically in Figure 1.2, taken from Cooray (2016).

The CRB spans the 3 to 90 GHz regime of the cosmic background and is measured using balloon borne radio experiments like ARCADE-2 (Kogut et al., 2011). This measurement was performed after correcting for the contribution from the CMB and galactic emission. A excess in the measured radio flux (measured by the experiment) was also seen and was suggested to due to emission caused by decaying WIMP (Weakly Interacting Massive Particle) dark matter particles (Fornengo et al., 2011). A reanalysis of the galactic syncrotron emission model displayed that this excess emission was accounted for and there

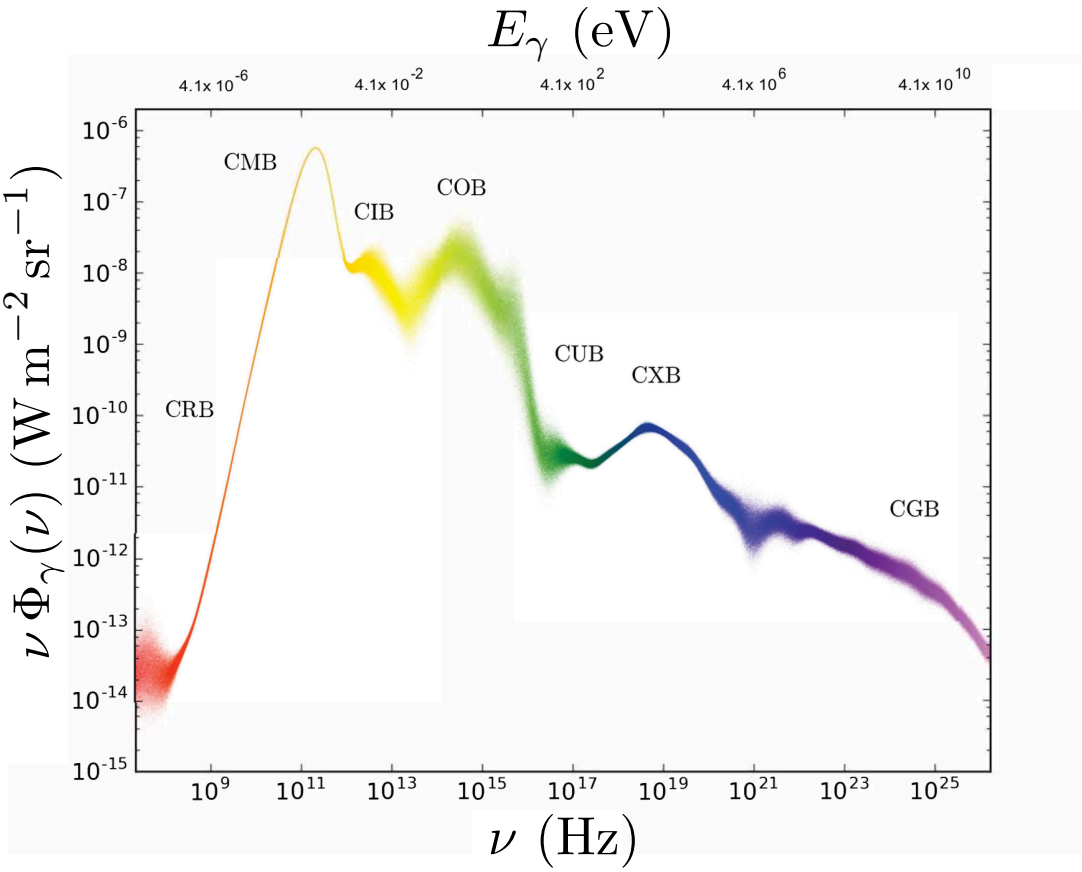

Figure 1.2 The intensity of the cosmic background radiation from radio to gamma rays as reported by Anchordoqui (2019) The shaded regions depict the errors in the measurement of the intensities.

is no leftover emission due to dark matter particles (Cooray, 2016). Future observations of the CRB focusing close to the 100 MHz frequency will be able to help separate out the background emissions from the large galactic foreground and understand the dark matter contribution to the background. The CRB also consists of weak radio emission from the epoch of reionization (Furlanetto, 2006; Burns et al., 2012) which will be measured using future missions like the Dark Ages Radio Explorer (DARE).

The CMB is the most dominant portion of the cosmic background emission peaking at an intensity of 960 nWm^{-2}sr^{-1}. As discussed in the previous section, the CMB is the leftover radiation from the Big Bang, and is formed during the recombination epoch. The

CMB was accidentally discovered in 1964 by Arno Penzias and Robert Wilson using a radiometer with the purpose of aiding NASA communication satellite experiments and radio astronomy (Penzias & Wilson, 1965). Since its accidental discovery, the best CMB measurement, described as a Planck function with a blackbody temperature of 2.72 K comes from COBE/FIRAS (Fixsen, 2009). Minor fluctuation in the nanokelvin regime exist for this temperature measurement and is studied by missions like WMAP and PLANCK. Because of the importance of properly studying these fluctuations, its measurement forms the basis of the mission statement for next generation CMB experiments. A lot of key cosmological studies have been performed after the detection of the CMB as it gives us a view of the Universe when it was ∼375,000 years old. These studies include, but are not limited to, understanding the Big Bang processes, inflation in the early Universe, fluctuations, lensing of CMB to study structure formation and neutrinos, e.t.c (Cooray, 2016; Planck Collaboration et al., 2016).

The CXB spans the ∼100 eV to ∼300 keV region of the cosmic background radiation and stands to be the first background radiation that was discovered. In 1962, the CXB was detected during a rocket flight measurement with the aim to study X-ray emission from the moon which instead found the CXB (Giacconi et al., 1962). After this initial breakthrough, many observations of the CXB took place using instruments like HEAO1 in the 2 to 30 keV and 100 to 400 keV regime (e.g. Marshall et al., 1980), SWIFT/BAT and integral at 30 keV (Ajello et al., 2008; Churazov et al., 2007) and XMM-Newton in the 0.5 to 2 keV and 2 to 9keV regime (e.g. Worsley et al., 2005). Owing to the tremendous progress made in the study of the CXB due to all these observations using modern detectors, it has been well established that the background is the collective emission from individual X-ray sources like AGN and starburst galaxies (Hasinger et al., 2005; Treister et al., 2009; Ueda et al., 2014).

The CGB at energies $\gtrsim$0.3 MeV GeV has been studied using different missions like SAS-2 (Small Astronomy Satellite 2; Fichtel et al., 1978), EGRET (Energetic Gamma Ray Experiment Telescope; Strong et al., 2004) and recently *Fermi*-Large Area Telescope (LAT) (Ackermann et al., 2015b). The CGB spectrum is made up of gamma ray emissions from

extragalactic sources like AGN, star forming galaxies and radio galaxies as well as a minute contribution from truly diffuse processes (Ajello et al., 2015). A cutoff is seen in the spectrum at higher energies due to the pair production processes explained in the next section. Contributions from millisecond pulsars, supernovae, galaxy clusters and possibly dark matter decay (Bertone et al., 2005) also forms a small portion of the CGB. The *Fermi*-LAT has been extensively used to study the CGB and its fluctuations verifying that the CGB intensity in the 0.1 to 820 GeV regime is truly comprised of AGN, pulsars and star burst and radio galaxies (see also Ackermann et al., 2012a; Di Mauro et al., 2013; Ajello et al., 2015). Additionally the upcoming Cherenkov Telescope Array (CTA) will be able to resolve the average CGB allowing researchers to compare it with existing measurements from *Fermi* to determine the total amount of extragalactic gamma rays produced (Gaté et al., 2017).

1.3 Extragalactic Background Light

The Extragalactic Background Light (EBL) is the diffuse background radiation accumulated over the cosmic history at ultraviolet (UV), optical and infrared (IR) wavelengths (Dwek & Krennrich, 2013; Desai et al., 2019a). The EBL is the second brightest component of the cosmic background after CMB (see Figure 1.2) with its intensity peaking twice (at ~ 1 μm and at ~ 100 μm). The first peak in the EBL spectrum is due to the light emitted by stars and accreting compact objects which also makes up the UV and optical component of the EBL. Cosmic dust in the vicinity of these sources absorbs some fraction of their light and re-emits it in the infrared part of the electromagnetic spectrum forming the IR portion of the EBL peaking at ~ 100 μm (Brun, 2013; Desai et al., 2017; Desai et al., 2019a). The resulting double hump structure (seen as the shaded yellow and green regions in Figure 1.2) of the EBL intensity is a function of redshift, and is determined by parameters like the cosmic star formation history, stellar initial mass function and photon escape fraction (Hauser & Dwek, 2001; Kashlinsky, 2005; Desai et al., 2017). Moreover as mentioned in Desai et al. (2017), (see also Chapter 4), in addition to these standard sources of light, the EBL could

also comprise photons from dark matter particle decay and other potential exotic energy releases (Maurer et al., 2012; Domínguez & Prada, 2013a). Thus, a thorough understanding of the EBL and its spectral intensity can be used to better understand not only early star formation and evolution processes but also galaxy formation and evolution tracing back to the epoch of reionization.

1.4 EBL intensity measurement

A direct measurement of the the EBL intensity is extremely difficult due to contamination from foreground emissions. To counter this and obtain strict lower limits on the EBL intensity, the lower limit of the combined light emitted from galaxies can be estimated using galaxy number counts (Fazio et al., 2004; Béthermin et al., 2010). However, these measurements can only serve as a lower limit due to the limitation of how deep the galaxy surveys are which would determine the number of faint galaxies observed (e.g. Béthermin et al., 2012). To counter this, an accurate measurement of the EBL can be performed using an indirect approach where the EBL is studied via the absorption that it leaves in the spectra of distant gamma-ray sources like Active Galactic Nuclei (AGN) and Gamma Ray Bursts (GRB). All these methods are discussed in more detail in Chapter 2).

Using these measurements and/or the understanding of the fundamental quantities that contribute to the EBL intensity, various EBL models have been constructed (e.g. Kneiske & Dole, 2010; Finke et al., 2010; Domínguez et al., 2011; Gilmore, 2012; Helgason & Kashlinsky, 2012a). These models calculate the total luminosity density coming from starlight and reprocessed light from dust and how it evolves using different methodologies. As discussed by Domínguez et al. (2011) and Gilmore et al. (2012) the EBL models can be subdivided into four major types according to the methodology used to calculate the luminosity density: (1) Forward evolution; (2) Backward evolution; (3) Evolution of inferred galaxy properties; (4) Direct observations galaxy properties and their evolution. Because of these differences in the modeling methodology there are many discrepancies between the

EBL models, especially at high redshifts (see Figure 1.3)

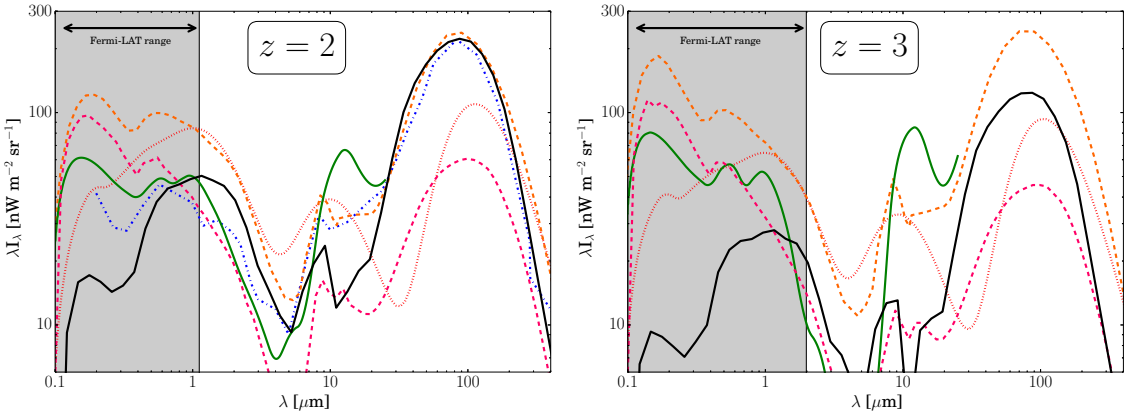

Figure 1.3 Intensity of the EBL at redshift $z = 2$ and $z = 3$ versus rest-frame wavelength. Note the wavelength range (in gray) that the *Fermi* observations of this research will sample. At these high redshifts the UV-optical background is uncertain by a factor >10. The lines show predictions from several models: (Domínguez et al., 2011, black), (Franceschini et al., 2008, blue dash-dotted), (Helgason & Kashlinsky, 2012b, green), (Gilmore et al., 2012, orange dashed), (Inoue et al., 2013, pink dashed), and (Finke et al., 2010, orange short dashed).

To reduce the discrepancy in the calculation of the EBL intensity, various measurements of the EBL have been carried out using the indirect method (e.g. Ackermann et al., 2012b; Abramowski et al., 2013a; Biteau & Williams, 2015; Ahnen et al., 2016). This PhD thesis primarily focuses on improving this measurement of the EBL intensity even further by making use of both GRBs (Desai et al., 2017) and AGNs (The Fermi-LAT Collaboration, 2018; Desai et al., 2019a) using the *Fermi*-LAT and Cherenkov telescopes. While the GRB and AGN data observed in the GeV regime using the *Fermi*-LAT helped constrain the UV and optical EBL intensity, Cherenkov Telescope data, observed in TeV, helped measure the infrared EBL. The EBL measurements from the GeV data came from the spectra of 759 AGNs and 22 GRBs (Gamma Ray Burst) observed up to a redshift z=4.35 which by extension led to a measurement of the EBL spectral intensity and a measurement of the star formation density as a function of time (The Fermi-LAT Collaboration, 2018). To improve this measurement of the EBL spectral intensity even further (not only in the Ultraviolet and optical regime but also at the near-Infrared wavelengths), TeV data from Cherenkov telescopes were used (reported by Biteau & Williams, 2015) and combined with the results derived from Fermi observations (explained in more detail in Chapter 6).

While our final measurement of the EBL intensity in the local Universe (Desai et al., 2019a) and its evolution extending to a redshift of $z \sim 6$ (The Fermi-LAT Collaboration, 2018) is currently the most updated quantification of the EBL, there is still a slight room for improvement in the future. This can be achieved with the help of a larger sample size or better observing instruments and measurement techniques. As we will discuss in Chapters 4 and 7, a larger sample size can be obtained by increasing the number of sources with known redshift measurements using spectroscopic campaigns similar to Marchesi et al. (2018); Desai et al. (2019b). An improvement in the sample size and the measurement of the EBL will also be significantly achieved with the observations from the upcoming CTA. Owing to the higher sensitivity of the CTA to gamma rays in the 10 GeV to 100s of TeV (Mazin et al., 2013; Gaté et al., 2017), a highly accurate measurement of the EBL attenuation in the blazar spectra will be seen. Moreover, the results obtained with CTA will allow us to put stronger constraints on the EBL intensity not only at optical wavelengths but also for IR wavelengths will be seen. Indeed the much awaited James Webb Space Telescope (JWST) will also contribute significantly to the direct measurement of the EBL and help constrain the EBL even further.

In Chapter 2, we discuss the different EBL measurement techniques in more detail along with the primary sources (GRB and AGN) used in our study. Chapter 4 reports the work done in Desai et al. (2017) for EBL measurement using GRBs. Chapter 5 and Chapter 6 reports the EBL measurement work done by The Fermi-LAT Collaboration (2018) and Desai et al. (2019a) using AGN respectively. To improve upon the EBL measurements, we report the results of a spectroscopic campaign (Desai et al., 2019b) in Chapter 7. Finally, Chapter 8 discusses the key results obtained from the cumulative work presented in this thesis and discusses the future implications of these results.

Chapter 2

Measurement of the EBL

Many efforts have been made to quantify the EBL intensity due the vast amount of scientific knowledge that can be derived from its measurement. These measurements can be primarily divided into three subsections: Direct measurements, Integrated galaxy counts and Indirect measurements. Direct measurements aims to directly measure the background in the UV, optical and IR regime using measurements obtained from missions like Hubble, Spitzer, UVS/STIS and DIRBE. Integrated galaxy or source counts provide the lower limit of the EBL intensity using the number count of galaxies (see Driver et al., 2016). The most effective EBL intensity measurement comes from indirect techniques which makes use of the attenuation found in the gamma ray spectra of distant high energy sources. The EBL intensity measured using these techniques, reported by Cooray (2016) is shown in Figure 2.1 and is described in detail below.

As mentioned in Cooray (2016) the points in Figure 2.1 are given as follows: DIRBE: red circles (Wright, 2004, 2001), stars (Cambrésy et al., 2001; Gorjian et al., 2000; Levenson et al., 2007), open squares (Hauser et al., 1998); IRTS: purple crosses (Matsumoto et al., 2005); Spitzer: open triangle (Levenson & Wright, 2008); Hubble: green circles (Bernstein, 2007); UVS/STIS: blue upper limits (Edelstein et al., 2000; Brown et al., 2000); CIBER: blue circles (Zemcov et al., 2014); FIRAS: black line (Lagache & Puget, 2000; Fixsen et al., 1998); IRAS: blue square (Miville-Deschênes et al., 2002). The lower limits to the EBL

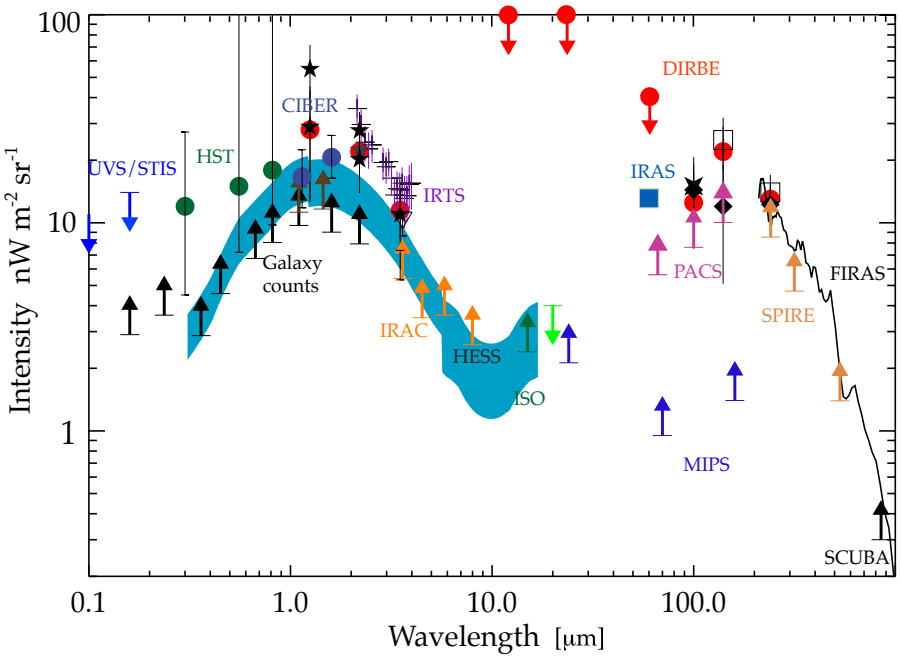

Figure 2.1 The measurement of the EBL intensity as reported by Cooray (2016) using the EBL and integrated counts measurements presented by Dole et al. (2006).

are from integrated or source counts using Hubble, Spitzer/IRAC, ISO, Spitzer/MIPS, Herschel/PACS, Herschel/SPIRE (Gardner et al., 2000; Madau & Pozzetti, 2000; Fazio et al., 2004; Berta et al., 2010; Béthermin et al., 2012). Blue shaded region: Estimate using the HESS data (Abramowski et al., 2012).

2.1 Direct Measurements

As EBL is the diffuse background emission, direct measurements are performed by measuring the foreground using either modeling methods or observations and then subtracting it from the total observed emission. However the prime difficulties faced by this method is the interference because of the bright atmospheric (for ground based telescopes) and zodiacal light. While the atmospheric light is made up airglow seen in the ionosphere and scattered radiation from the troposphere, the zodiacal light is composed of solar radiation scattered by interplanetary dust(see Mattila & VÃisÃnen, 2019). If measured beyond

the interplanetary dust cloud, integrated starlight plays a major role acting like a bright foreground for direct measurements. In addition to these major bright foregrounds, diffuse galactic light, scattered light due to interstellar dust and emission by interstellar gas still remains an issue (Hauser et al., 1998; Matsumoto et al., 2005; Matsuoka et al., 2011; Mattila et al., 2017).

The first photometeric measurement of the EBL was made in 1968 where, due to interference from galactic dust extinction, the intensity of the EBL was taken to be decreasing closer to the galactic plane (E. Roach & L. Smith, 1968). However this measurement was contaminated due to the bright diffuse galactic light and integrated starlight foreground which also depend on the galactic plane. Many similar measurements were made after 1968 using different techniques and model estimations along with better instruments to measure the EBL (Hauser et al., 1998; Bernstein, 2007; Matsumoto et al., 2005). A major highlight in the background observation was seen when the Pioneer 10 and 11 spacecrafts passed the asteroid belt in 1972 and 1974 respectively. For the EBL measurements, out of the major foregrounds, only the diffuse galactic emission and integrated starlight remained while the zodiacal light dropped to negligible values. An EBL detection was made with $\lambda_{I_{EBL}} = 7.9 \pm 4.0$ at 440 nm and $\lambda_{I_{EBL}} = 7.7 \pm 5.8$ at 640 nm with a $1.5 - 2\sigma$ significance (Matsuoka et al., 2011). However to derive this measurement a number of stellar catalogs had to be assembled, making the measurement uncertain. Recently, Matsumoto et al. (2018) report the instrumental offsets and noise in the pioneer data-sets and classify the data to be used to measure the mean EBL intensity rather than the absolute measurement. Other direct measurements made of the UV to IR background is shown in Figure 2.1. The Zodiacal light in the DIRBE observations is removed using modeling techniques (Kelsall et al., 1998) or variations (Wright, 2001), while HST makes use of spectroscopy to estimate the column density of dust and use it to remove the zodiacal emission (Bernstein et al., 2002). Future observations from the CIBER sounding rocket experiment Zemcov et al. (2013), is expected to measure the zodiacal light intensity with more accuracy thereby giving us a more accurate measurement of the EBL from direct detect ions after subtracting the zodiacal light.

Furthermore, as reported by Cooray (2016), Spitzer/IRAC shutter operations should also be able to contribute effectively to the absolute EBL measurements.

2.2 Galaxy Surveys

As the EBL is the record of the total emission from the age of the first stars to present day, the total integrated light emitted from all the galaxies can serve as a suitable lower limit (see Figure 2.1). As discussed in Mattila & VÃisÃnen (2019), this Integrated Galaxy Light (IGL) can be calculated using the following integral which must be summed over different types of galaxies:

$$IGL = \frac{1}{4\pi} \int_0^{z_f} \frac{dl}{dz} \frac{F}{(1+z)^3} dz \tag{2.1}$$

where, F is the emissivity of the galaxy of a given galaxy type, at a given redshift z and at a frequency of $v = v_0(1+z)/(1+z_0)$. The dl/dz term accounts for the cosmological dependencies of the model. This integrated galaxy light can also be calculated by using the number of galaxies $N(m)$ observed per magnitude bin.

After extrapolating the integrated light at a given brightness using this approach, the total integrated light measurement can be obtained. However, until quite recently, direct detection methods appeared more reliable as compared to galaxy counts due to lack of detection of galaxies with very faint fluxes. With the deep field data observed using new age ground and space based telescopes like Galaxy Evolution Explorer (GALEX), Hubble Space Telescope (HST) Spitzer and Hershel, direct measurements and galaxy counts measurements have become comparable. Béthermin et al. (2012) reports the measurement of the integrated source counts to account for over 75% of the directly measured EBL in the infrared regime. As reported by Driver et al. (2016), the remaining discrepancy can be accounted for by a combination of contribution from lensed systems together with extrapolation of source counts. However in the optical regime the direct measurements are still a factor of 5 times larger than the galaxy count estimates (Keenan et al., 2010). EBL measurement using

gamma ray data (discussed in next section) has shown to favour the galaxy count data by providing a much lower measurement as compared to direct methods. Recently Driver et al. (2016), reported an updated IGL, EBL measurement over the complete wavelength range using a combination of existing source count data and using a new modeling approach (see Figure 2.2. This measurement provides a strict lower limit to the EBL intensity which can be used along with other measurement methods to more accurately measure the EBL.

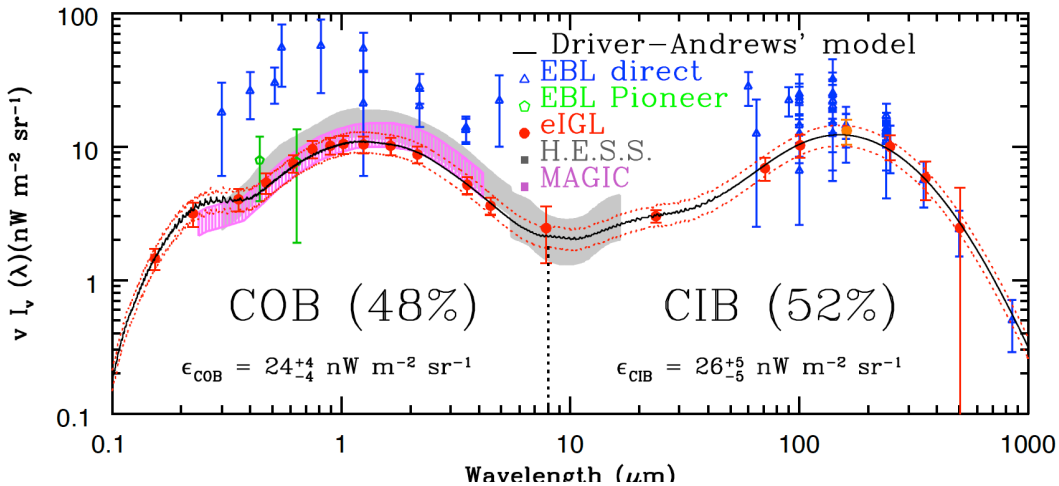

Figure 2.2 EBL measured using IGL as reported by Driver et al. (2016) compared with measurements obtained using HESS and MAGIC instruments. The blue stars depict Biteau & Williams (2015) constraints.

As discussed above, contamination from foreground emissions and galactic dust emissions have proven to be a significant issue while measuring the EBL. As these emissions have to be estimated using different modeling methods and observations, it becomes difficult to properly constrain the EBL. Fortunately, there exists a third method for the measurement of the EBL, discussed in the next section, which is dubbed as indirect measurement method and which makes the use of the gamma ray spectra of distant high energy sources.

2.3 Indirect Measurements

Some parts of the following section are taken from Desai et al. (2017). As reported by Stecker et al. (1992); Dwek & Krennrich (2013),etc, an indirect approach of probing the EBL and its redshift evolution is through the γ-γ absorption it imprints in the spectra of distant high-energy γ-ray sources. The high-energy part of their spectral energy distributions (SEDs) is attenuated due to annihilation with background photons (γ-$\gamma \Rightarrow e^{+}$-e^{-} pair creation; see Figure 2.3) as discussed by Nikishov (1961) and Gould & Schréder (1967a,b). Because of the dependence of the pair-production cross section on the threshold energy (see Appendix B, γ rays (of a given energy) will most likely interact with EBL photons of given wavelengths: e.g. γ rays with E$\gtrsim$50 GeV (and from z$\gtrsim$1) are attenuated mainly by photons of the optical-UV background (>1 eV).

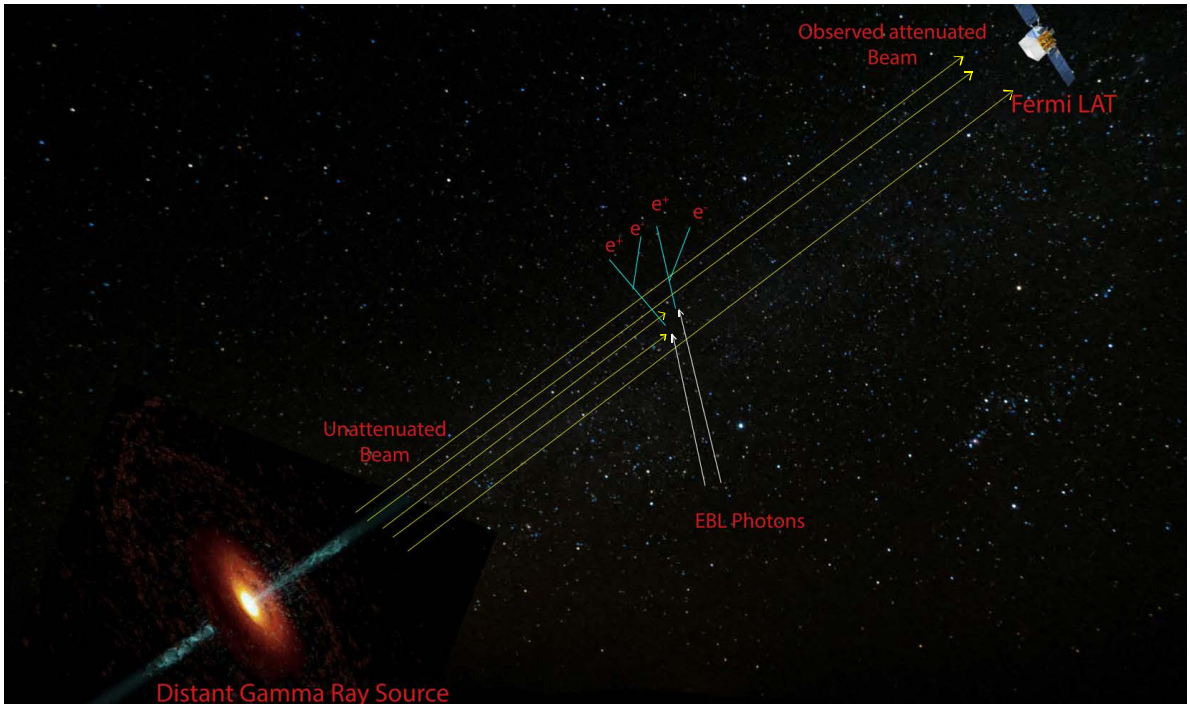

Figure 2.3 A simple figure depicting the pair production that takes place between an incoming gamma ray photon with a photon from the EBL attenuating the source spectrum.

The primary condition for this pair production to take place can be better understood

with the help of the following equation:

$$E_{EBL}^{threshold} = \frac{2(m_e c^2)^2}{E_\gamma(1 - cos\theta)} \tag{2.2}$$

where, $E_{EBL}^{threshold}$ is the minimum required Energy of the EBL photon to interact with an incoming gamma ray photon of energy E_γ at an angle of θ. In the equation, m_e depicts the mass of an electron and c gives the speed of light in vacuum. The amount of photons annihilated because of this pair production process and the effective observed attenuation in the spectrum of the source can be calculated by using the EBL optical depth. The optical depth of a medium is defined as the amount of energy that gets absorbed when a photon, emitted from a particular distance, is passing though that medium, which in our case is the EBL. The EBL optical depth (τ_{EBL}) is found from a proper cosmological integration over redshift, which requires an understanding of how the EBL builds up with cosmic time (Dwek & Krennrich, 2013). For an incoming gamma ray photon emitted at redshift distance of z with energy E_γ the EBL optical depth τ_{EBL} can be then be modeled

$$\tau_{EBL} = c \int_0^z \frac{dt}{dz'} dz' \int_{-1}^{1} (1 - \mu) \frac{d\mu}{2} \int_{E_{EBL}^{threshold}}^{\infty} \sigma(E', E_\gamma, \mu) n(E', z') dE' \tag{2.3}$$

where, $E_{EBL}^{threshold}$ is derived from Equation 1, $\mu = cos\theta$, $\sigma(E', E_\gamma, \mu)$ is the interaction cross section and $n(E', z')$ is the photon number density. The EBL optical depth curve is similar to the shape of the number density curve (increasing with z and E_γ) as seen in Figure 2.4. The EBL attenuation is then quantified using the following relation between τ_{EBL} and photon flux density:

$$\frac{dN}{dE}_{int} = \frac{dN}{dE}_{obs} e^{-\tau_{EBL}} \tag{2.4}$$

where $\frac{dN}{dE}$ is the photon flux density intrinsic (int) to the source spectrum and observed (obs) by gamma ray telescopes. A measurement of the attenuation ($e^{-\tau_{EBL}}$) is then obtained by

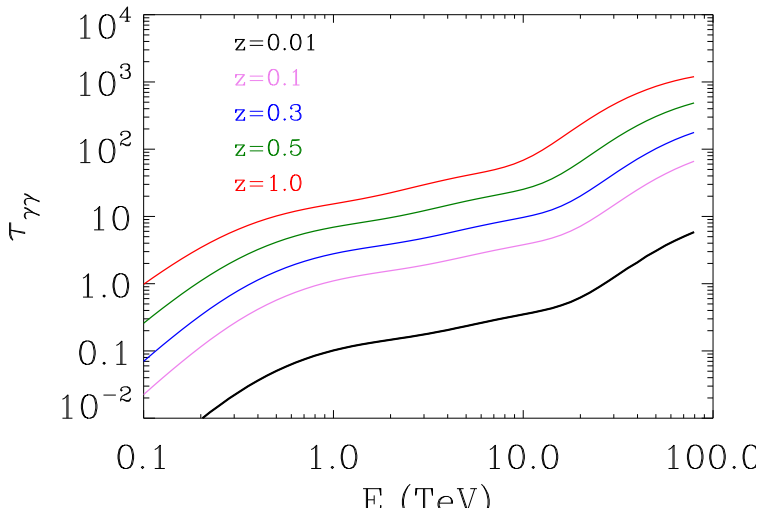

Figure 2.4 Figure taken from Dwek & Krennrich (2013) who use the EBL model of Finke et al. (2010) to plot the EBL opacity as a function of energy for different redshifts.

comparing the observed source spectrum with the intrinsic spectrum. This attenuation allows the use of γ rays of different energies (and originating from sources at different redshifts) to explore the SED of the EBL and its evolution with redshift. While the Galactic emissions and zodiacal light constitute a problem for direct measurements, they make no difference for the γ-ray technique as the mean free path of photons in the MeV to TeV regime is much larger (>10 Mpc) than Galactic or solar scales (Adams et al., 1997).

During my research work I made use of Gamma Ray Bursts (GRB) and Active Galactic Nucluei (AGN) to measure the EBL using this method. Three different set of sources were used: 1. GRBs observed by the *Fermi*-LAT in the 100 MeV to 500 GeV regime (see Chapter 4); 2. AGN observed by the *Fermi*-LAT in the 100 MeV to 1000 GeV regime (see Chapter 5) and 3. AGN observed by Cherenkov telescopes in the 100 GeV to 21 TeV regime (see Chapter 6). These sources are described in the next subsection briefly following a discussion of the gamma ray instruments used to make the detection in Chapter 3.

2.3.1 AGN

AGNs are super-massive black holes found in the center of galaxies and are highly luminous because of matter falling into the blackhole. Due to this accreting matter, often, an extremely luminous jet consisting of relativistic particles is ejected from the center of the AGN. Also based on the classification of AGN and the unified AGN model (e.g Beckmann & Shrader, 2012; Acero et al., 2015)AGNs with their relativistic jets pointed towards the observer, form a subclass of luminous gamma-ray sources commonly known as blazars which dominate the observable γ-ray Universe (see Figure 2.5).

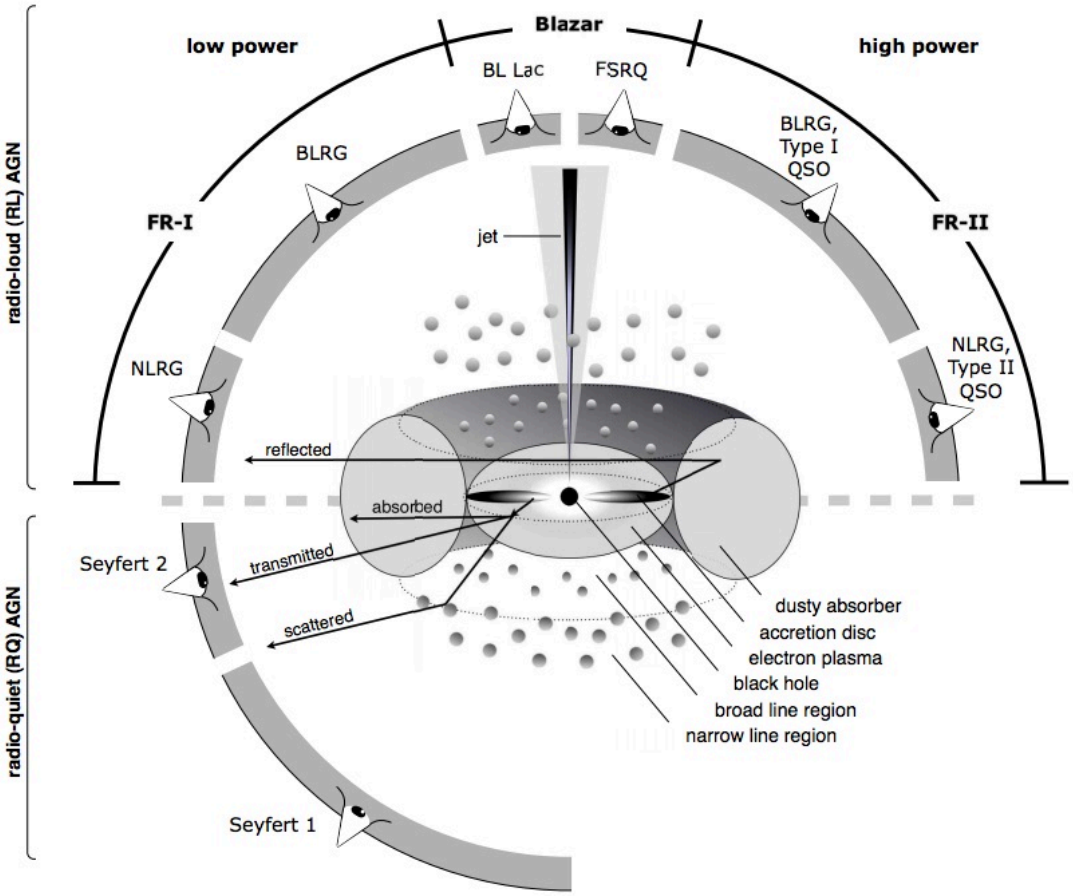

Figure 2.5 The unified AGN model depicting the various classes of AGN based on the viewing angle of the jet emitted from the central black hole. Figure taken from Beckmann & Shrader (2012).

The blazar properties are a result of non-thermal emitting plasma traveling towards the observer causing relativistic amplification of flux. This amplified flux is measured in the GeV and TeV regimes using the *Fermi*-LAT and cherenkov telescopes. This makes blazar sources ideal candidates for EBL measurement. Measurements made using the blazar source sample is discussed in more detail in Chapters 5 and 6.

As we report in Desai et al. (2017), the extremely luminous blazar source sample has been extensively used in the past to constrain the EBL. Inspite of using different methods to model the intrinsic source spectrum (Abramowski et al., 2013b; Ackermann et al., 2012a; Mazin et al., 2017; The Fermi-LAT Collaboration, 2018),there remain some doubts whether γ-ray measurements of the EBL using blazars are completely trustworthy (Essey & Kusenko, 2010; Essey et al., 2011). It has been proposed that the observed γ-ray absorption may be affected by line-of-sight interaction of cosmic rays (accelerated in jets of BL Lacs) with the CMB/EBL would produce secondary γ-rays. The line of sight interaction of cosmic rays (accelerated in jets of BL Lacs) with the CMB/EBL would generate a secondary γ-ray component, which, being much closer to the observer would suffer less EBL attenuation and would lead to underestimation of the true EBL energy density. The detection at TeV energies of BL Lacs with unusually hard de-absorbed spectra (e.g. Horns & Meyer, 2012; Furniss et al., 2013) has been interpreted also in this framework. These possibilities were discounted by Biteau & Williams (2015) who find that the spectra reconstructed after de-absorption are not too hard with respect to expectations. A similar conclusion was reached by Domínguez & Ajello (2015) who do not find any deviation of the predicted EBL attenuation in the LAT blazar data. In addition to these theoretical uncertainties, the sample of BL Lacs suffers from a significant drop in sample size beyond a redshift of $\sim$1.0. To account for these shortcomings GRB data are also used as probes of the EBL, discussed in the next section.

2.3.2 GRB

GRBs are highly energetic short bursts of radiation caused due to violent cosmic processes like supernova explosions or neutron start-neutron star merger. As the intrinsic

spectral properties of GRBs are relatively easier to determine as compared to Blazars and as they are detected at high redshifts, they become the ideal candidate for EBL studies. However because of the short duration of the burst, an accurate redshift measurement for all the detected GRBs cannot be made, making the effective sample of sources which can be used for the EBL study exceedingly small. This again makes blazars currently a preferred source sample to constrain the EBL. Indirect EBL measurement using GRBs is discussed in more detail in Chapter 3.

Chapter 3

Instruments

In our study of EBL attenuation we make use of the *Fermi*-LAT to observe GRBs and Blazars in the range of 100 MeV to 500 GeV (High energy; HE regime)and Cherenkov telescopes to observe Blazars in the range of 100 GeV to 21 TeV (Very High energy; VHE regime). In this section we discuss the working of these telescopes and also discuss the upcoming CTA telescope which will also observe in the VHE regime with increased sensitivity.

3.1 *Fermi*-LAT

This section reports the working and mission of the *Fermi*-LAT as described in *https://glast.sites.stanford.edu/*. Originally known as the Gamma-Ray Large Area Space Telescope (GLAST), the Fermi Gamma Ray Space Telescope was renamed to honor the physicist Enrico Fermi. The *Fermi* telescope was launched in June 2008 with a mission operation goal of 10 years. Recently in 2018 the *Fermi* telescope completed 10 successful years of data taking. As given on the NASA Fermi website[1], *Fermi* mission statement includes studying the cosmos in the high energy regime from 10 keV to 300 GeV to explore the most extreme environments in the Universe, search for signs of new laws of physics, explaining the concept behind AGN jets and access topics like pulsars or the origin of

[1] https://glast.sites.stanford.edu/nasa-mission

cosmic-rays.

The two instruments on board the *Fermi* telescope are: The Gamma-ray Burst Monitor (GBM) and the Large Area Telescope (LAT) which are discussed in more detail below:

3.1.1 GBM

As described on the National Space Science and Technology Center (NSST), Fermi GBM website[2], the operation and data analysis of the GBM is a collaborative effort between the NSST and Max Planck Institute for Extraterrestrial Physics. The main aim of the GBM is to perform a periodic survey of the complete visible sky and provide burst triggers and locations. The GBM is made up of 12 Sodium Iodide (NaI) scintillation detectors, to cover the energy range from a few keV to about 1 MeV, and 2 Bismuth Germanate (BGO) scintillation detectors covering the ∼150 keV to ∼30 MeV energy regime. These detectors as seen in Figure 3.1 sit in between the LAT and the solar panels thereby not interfering with the operations of any instrument. The NaI detectors are mounted in 4 separate banks each with a set of three detectors to maximize the azimuth range and elevation angles observed.

The observing field of view of the GBM is 9.5 steradians with a gamma ray burst location accuracy of 3" and a timing accuracy of 2 μs (Meegan et al., 2009). As summarised by Thompson (2018), all the successful years of operation of the *Fermi* telescope has allowed the GBM to observed a total of 1405 GRBs, the results of which are listed in the third Fermi GBM Gamma-Ray Burst Catalog (Bhat et al., 2016). Additionally, a time resolved catalog of 81 GRBs (Yu, Hoi-Fung et al., 2016), a GBM Magnetar Catalog presenting data on flares from magnetars (Collazzi et al., 2015), a GRB X-ray burst catalog of 1084 X-ray Bursts (Jenke et al., 2016) and a catalog of over 4000 terrestrial gamma ray flashes (Roberts et al., 2018) were reported by the GBM.

[2]https://gammaray.msfc.nasa.gov/gbm/

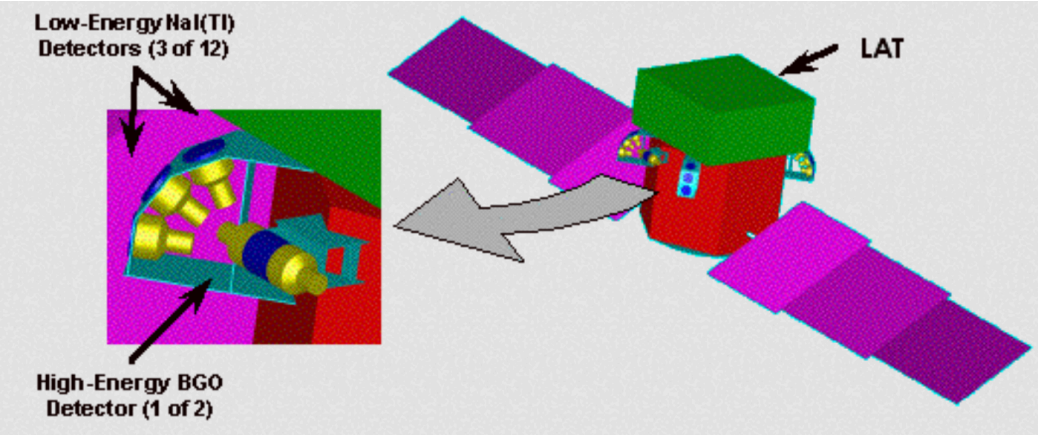

Figure 3.1 A schematic view of the GBM on board the *Fermi* telescope. Image Credit: *https://f64.nsstc.nasa.gov/gbm/instrument/*

3.1.2 LAT

The main aim of the LAT is the detection of incoming high energy gamma rays which cannot be refracted or focused using a lens or mirror like visible light. Thus, the gamma rays are detected using an electron positron pair production method akin to the one used in high-energy particle accelerators. To achieve this, a thin plastic anticoincidence detector causes the incoming gamma rays to pass freely but charged cosmic rays to cause a flash of light separating out the relatively rare gamma rays. Next there are 18 tungsten covered foils which cause the gamma ray to convert into an electron and positron pair. These particles are detected by silicon strip detectors which alternate in the X and Y direction tracking the progress of the particles thought the telescope. The particles are then finally stopped and their energy is measured by a cesium iodide calorimeter at the bottom part of

the instrument (see Figure 3.2 for details). The combined information from the detector, tracker and calorimeter is then used to determine the direction and energy of the incoming gamma ray photon.

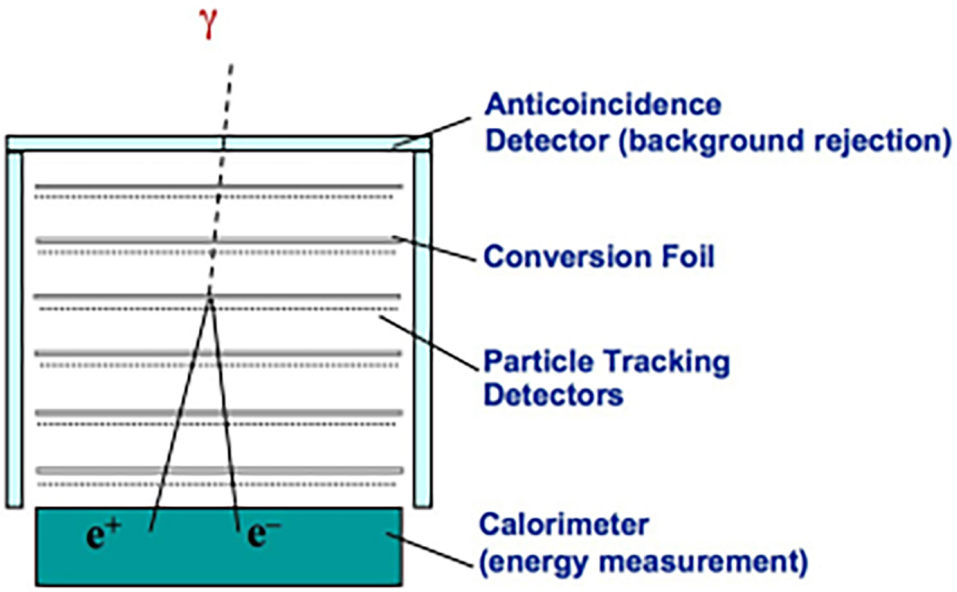

Figure 3.2 A schematic view of the LAT on board the *Fermi* telescope. Image Credit: *https://glast.sites.stanford.edu/instrument*

To make use of the large FoV of the LAT, the *Fermi* spacecraft, orbits the earth in about 96 minutes with the LAT pointed upwards at all times to remove interference from earth. Moreover the spacecraft is made to rock in the right and left directions thereby allowing the telescope to survey the whole sky in two orbits. During just the first year of operation, the LAT detected more than 150 million gamma rays and has produced amazing results ever since. The LAT has been able to churn out a number of groundbreaking discoveries in the galactic and extragalactic regime. Some of these discoveries include an all sky gamma ray view of the sky (see Figure 3.3), Detection of unknown blobs of energy perpendicular to the galactic plane known as Fermi Bubbles, study of AGN and Blazar variability, study of GRBs, radio galaxies, starburst galaxies and globular clusters, etc.

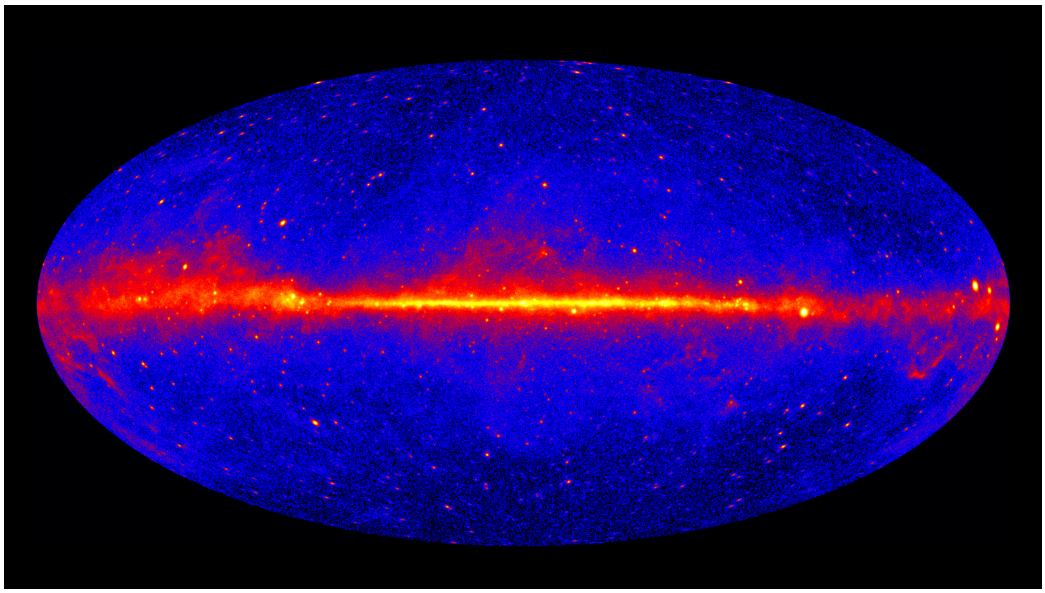

Figure 3.3 The Fermi LAT all sky gamma ray map collected by making use gamma rays observed at energies > 1 GeV over a period of 60 months. The bright diffuse glow along the map's center is the center of our milky way galaxy. Image credit: NASA/DOE/Fermi LAT Collaboration

3.1.3 Pass 8:

The analysis of the raw data collected by the LAT relies on reconstruction using Instrument Response Function (IRF) which is a parameterization of the performance of the LAT. Recently the LAT team of researchers developed a new event analysis and selection criteria dubbed "Pass 8". This new event analysis provides a better reprocessing of the entire dataset collected by the LAT by providing improved event reconstruction, better separation of observed gamma rays from cosmic rays, more accurate energy measurements over a wider energy range and an improved position accuracy. In our analysis of the observed data to measure the attenuation of the EBL, we make use of this improved Pass 8 event analysis allowing us to measure the EBL optical depth with a decreased uncertainty (see Chapters

4 and 5).

3.2 Cherenkov telescopes

VHE photons from sources like AGN interact with the atmosphere to induce a cascade of subatomic particles. This cascade of charged particles similar to a particle shower travel faster than the speed of light in air causing a blue flash of light known as Cherenkov light. This cherenkov light or cherenkov radiation similar to a sonic boom was first discovered in 1934 by Pavel Cherenkov.

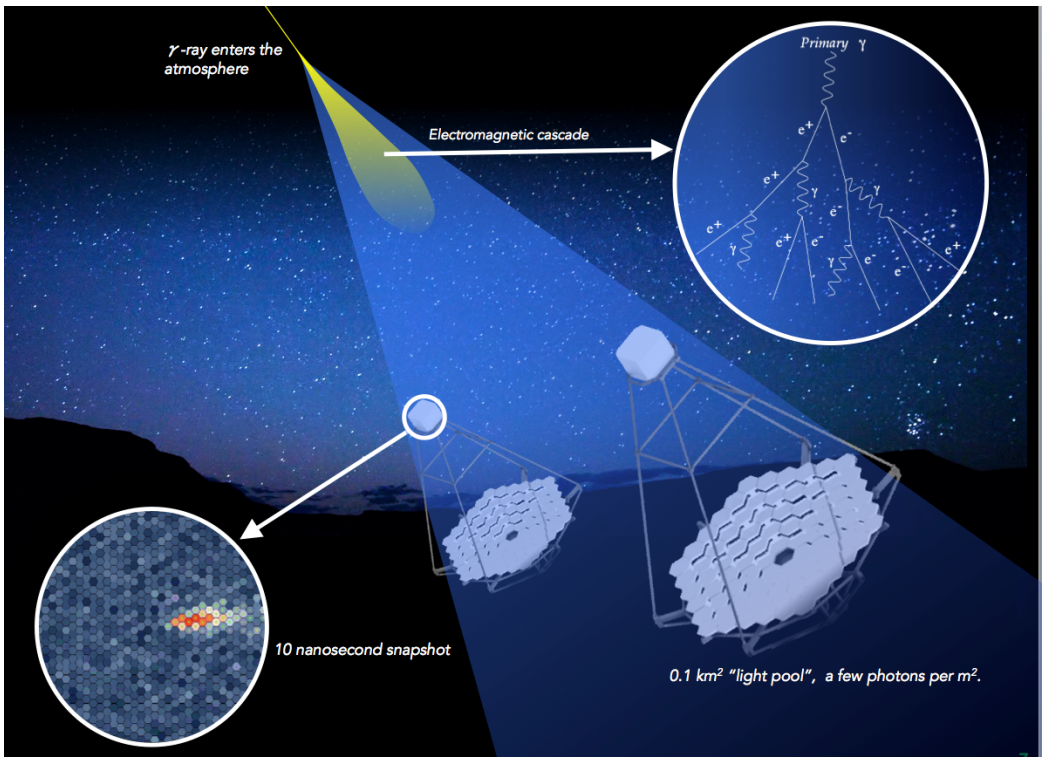

Figure 3.4 Figure depicting the working of a cherenkov telescope. Image Credit: "https://www.cta-observatory.org/about/how-cta-works/"

As shown in Figure 3.4, a light cone is formed by this particle shower and is spread over a large area on the surface of the earth (∼250 m). However, as the cascade lasts for a

short amount of time, in the order of few billionths of a second, its too faint to be detected by human eye but is captured by the cherenkov telescope detector. The energy and angle of the cascade is then used to determine the energy of the incoming gamma ray photon that interacts with the atmosphere and the position of the sky from which it was emitted.

Using the concept of the cherenkov shower generated by gamma rays interacting with the atmosphere, telescopes like HESS (High Energy Stereoscopic System), MAGIC (Major Atmospheric Gamma Imaging Cherenkov Telescopes) and VERITAS (Very Energetic Radiation Imaging Telescope Array System) are able detect photons with a maximum sensitivity from 100 GeV to 10s of TeV. These telescopes use an different combinations of highly sensitive imaging optical reflectors with fast readout light sensors like photomultiplier tubes spread out in the cone of radiation seen in Figure 3.4 to detect the radiation. A detailed discussion of the working of all of these telescopes can be seen in Park (2018).

The EBL attenuation in AGN has been extensively studied using Cherenkov telescopes in the past (e.g. Mazin et al., 2017; Abramowski et al., 2013b; Orr, 2011; Biteau & Williams, 2015). As the optical and infrared EBL photons (depending on the redshift of the observed source; see Chapter 1) interact with the TeV photons from AGN causing the attenuation, these measurements with Cherenkov telescopes is key not only to measure the optical portion of the background but also some part of the IR background. However, a major concern in working with telescopes lies in the selection of the unattenuated intrinsic model of the observed source. To tackle this issue, an accepted method is to fit the observed spectrum using different intrinsic models and with an fixed EBL optical depth (obtained from a generally accepted EBL model) to account for the EBL attenuation. The intrinsic model with the highest probability is then selected as the intrinsic model for that source (see also Biteau & Williams, 2015; Desai et al., 2019a). Using this intrinsic source method and the novel method described in The Fermi-LAT Collaboration (2018) for constraining the EBL optical depth in different redshift and energy bins we provide a most up-to-date measurement of the EBL intensity, to be discussed in more detail in Chapter 6.

3.3 CTA

A major improvement in the gamma ray data collected using Cherenkov telescopes will be seen with the upcoming CTA. With the goal to improve the sensitivity by a factor of 10 as compared to existing telescope, CTA will consist of more than 100 telescopes spread across the northern and southern hemisphere (Actis et al., 2011). The vast number of telescopes used by the CTA and the different sizes of the telescopes (decided based on sensitivity) will allow CTA to cover an energy range of 20 GeV to 300 TeV with a focus on a core energy range of 100 GeV to 10 TeV.

Many exciting scientific results will be derived using CTA data not only in the scientific field of Astrophysics but also in particle physics and quantum physics. The vast number of topics that will be addressed, for example, dark matter and its distribution; high energy particle acceleration in the Universe; processes behind the working of neutron stars, AGNs and blackholes; a precise measurement of the EBL and understanding the origin of cosmic particles (CTA Consortium, 2019). Focusing on the measurement of the EBL using CTA, we will be able to see a tremendous improvement in the measurement of the EBL intensity especially in the Infrared regime. This will be because CTA will have the capability to observe AGN sources with high redshiftz (z >2) and high energies targeting the spectral regime of AGNs in which the EBL attenuation would be due to interaction of TeV source photons with infrared EBL photons. This updated measurement of the EBL will also improve our understanding of the the formation and evolution of the first stars and galaxies and the role of dark matter in these early processes (Mazin et al., 2013).

The construction of the CTA has already begun, with existing working prototypes. The beginning of data collection is scheduled for 2022[3].

[3]https://www.cta-observatory.org/project/status/

Chapter 4

EBL measurement using GRB

This chapter presents the EBL measurement done using GRBs. This chapter is taken from Desai et al. (2017) [1].

4.1 Introduction

Light emitted by stars and accreting compact objects, through the history of the Universe, is encoded in the intensity of the extragalactic background light (EBL). Cosmic dust in the vicinity of these sources absorbs some fraction of their light and re-emits it in the infrared part of the electromagnetic spectrum. The resulting multi-component spectral energy density is a function of redshift, determined by cosmological parameters, stellar initial mass function, the cosmic star formation rate history and the dust content in galaxies (Hauser & Dwek, 2001; Kashlinsky, 2005). Therefore an understanding of the EBL evolution allows us to probe these astrophysical ingredients. In addition to these standard sources of light, the EBL could also comprise photons from dark matter particle decay and other potential exotic energy releases (Maurer et al., 2012; Domínguez & Prada, 2013a). The evolving EBL in the high redshift domain ($z \gtrsim 6$) is of particular importance as it traces the re-ionization epoch (Inoue et al., 2014). Contributions from the first generation of stars

[1] https://doi.org/10.3847/1538-4357/aa917c

(Pop III), might have originated from very massive stars, which cannot be observed directly with present day observatories or even with the soon to be launched James Webb Telescope. These topics have been discussed widely in the literature (Bond et al., 1986; Dwek et al., 2005; Raue et al., 2009; Gilmore, 2012; Kashlinsky et al., 2005, 2012; Inoue et al., 2013; Dwek, 2014)

Recognizing the importance of the EBL and its evolution with redshift, many efforts have been made to measure its photon intensity. Indeed, direct measurements of the EBL are difficult because of the bright foregrounds like Galactic emission and zodiacal light (Hauser et al., 1998; Matsumoto et al., 2005; Matsuoka et al., 2011; Mattila et al., 2017), resulting in estimates of the intensity of the EBL that are up to a factor of 10 larger than lower limits obtained by integrating the light of galaxies resolved in deep surveys (Madau & Pozzetti, 2000; Keenan et al., 2010; Driver et al., 2016). Studies of background fluctuations in the EBL suggest lower, although non-zero, levels of unresolved EBL intensity (Kashlinsky et al., 2012; Zemcov et al., 2014).

An indirect approach of probing the EBL and its redshift evolution is through the γ-γ absorption it imprints in the spectra of distant high-energy γ-ray sources. The high-energy part of their spectral energy distributions (SEDs) is attenuated due to annihilation with background photons (γ-$\gamma \Rightarrow e^{+}$-e^{-} pair creation) as discussed by Nikishov (1961) and Gould & Schréder (1967a,b). Because of the shape of the pair-production cross section, γ rays (of a given energy) will most likely interact with EBL photons of given wavelengths: e.g. γ rays with E$\gtrsim$50 GeV (and from z$\gtrsim$1) are attenuated mainly by photons of the optical-UV background (>1 eV). The total optical depth to a source is then found from a proper cosmological integration over redshift, which requires an understanding of how the EBL builds up with cosmic time (Dwek & Krennrich, 2013).

This extinction process therefore allows the use of γ rays of different energies (and originating from sources at different redshifts) to explore the SED of the EBL and its evolution with redshift. While the Galactic emissions and zodiacal light constitute a problem for direct measurements, they make no difference for the γ-ray technique as the mean free

path of photons in the MeV to TeV regime is much larger (>10 Mpc) than Galactic or solar scales (Adams et al., 1997). Observations over the $0.2 < z < 1.6$ redshift range with the *Fermi* Large Area Telescope (LAT) have resulted in the detection of the EBL attenuation in a collective sample of 150 BL Lacertae objects (BL Lacs, see Ackermann et al., 2012b). Ground-based measurements of low-redshift blazars ($z \lesssim 0.6$) in the TeV regime have resulted in optical depth estimates using High Energy Spectroscopic System (H.E.S.S.), Major Atmospheric Gamma Imaging Cherenkov Telescopes (MAGIC) and Very Energetic Radiation Imaging Telescope Array System (VERITAS) data (e.g. Abramowski et al., 2013b; Domínguez et al., 2013; Biteau & Williams, 2015). All measurements in the $0 \lesssim z \lesssim 1.6$ range point to a level of the UV-to-NIR EBL that is compatible with that inferred from galaxy counts as estimated by recent models (e.g. Franceschini et al., 2008; Finke et al., 2010; Domínguez et al., 2011; Stecker et al., 2012; Helgason & Kashlinsky, 2012b; Stecker et al., 2016).

All measurements of the γ-ray opacity measured above rely on BL Lacs as probes of the EBL. Because it has been proposed that the observed γ-ray absorption may be affected by line-of-sight interaction with cosmic rays (accelerated in jets of BL Lacs) producing secondary γ-rays, there remain some doubts whether γ-ray measurements of the EBL using blazars are trustworthy (Essey & Kusenko, 2010; Essey et al., 2011). Line of sight interaction of cosmic rays (accelerated in jets of BL Lacs) with the CMB/EBL would generate a secondary γ-ray component, which, being much closer to the observer would suffer less EBL attenuation and would lead to underestimation of the true EBL energy density. The detection at TeV energies of BL Lacs with unusually hard de-absorbed spectra (e.g. Horns & Meyer, 2012; Furniss et al., 2013) has been interpreted also in this framework. These possibilities were discounted by Biteau & Williams (2015) who find that the spectra reconstructed after de-absorption are not too hard with respect to expectations. A similar conclusion was reached by Domínguez & Ajello (2015) who do not find any deviation of the predicted EBL attenuation in the LAT blazar data. In addition to these theoretical uncertainties, the sample of BL Lacs suffers from a significant drop in sample size beyond a

redshift of ∼1.0.

In this work we overcome these limitations using the γ-ray bursts (GRBs) detected by the LAT during a 7-year period and for which redshift measurements are available (Hartmann, 2007). The short duration of the bursts ensures that the observed γ-ray emission is generated locally at the source, which renders GRBs clean probes of the EBL. Furthermore, GRBs are also observed at much larger redshifts (i.e., z =4.3 for GRB 089016C as reported by Greiner et al., 2009a) thus expanding the study of EBL attenuation to larger distances (see e.g. Kashlinsky, 2005).

This paper is organized as follows: § 6.2 presents the data processing and analysis, § 4.3 reports the methodology and results of the EBL study, § 4.4 considers systematic effects of the methodology, while § 6.4 discusses the results.

4.2 Data Analysis

There are more than 130 GRBs detected by *Fermi*-LAT (Vianello et al., 2016), out of which twenty-two GRBs measured between September 2008 and June 2015 have an associated redshift measurement, which comprise our source sample. These GRBs are reported in Table 4.1 along with their corresponding parameters. Table 4.2 reports the number of photons detected with the *Fermi*-LAT at an EBL optical depth greater than 0.1 (obtained using the model of Finke et al. (2010)-model C and corresponding redshift measurement for each GRB). In order to show how much the number of photons above a given optical depth varies when the EBL model is changed, we also report the number of photons detected at τ >0.1 using the models of Domínguez et al. (2011) and Kneiske & Dole (2010) (a more transparent and more opaque model than the one of Finke et al. 2010 respectively). The redshift distribution for our sample ranges from 0.15 to 4.35 and is shown in Figure 5.5 compared to the distribution for BL Lacs from the sample used by Ackermann et al. (2012b). Figure 4.2 shows the highest energy photons detected from these GRBs together with prediction of the cosmic γ-ray horizon from different models.

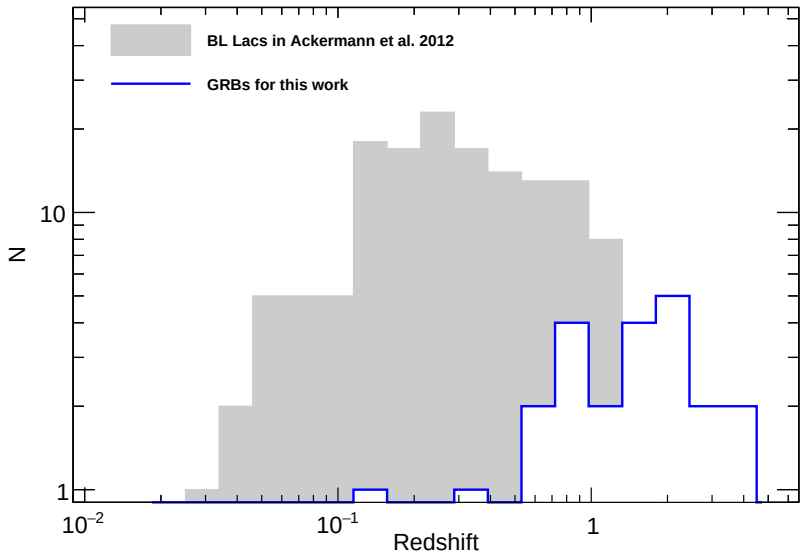

Figure 4.1 Redshift distribution for the sample of twenty-two GRBs used here compared to the sample of 150 BL Lacs used in Ackermann et al. (2012b).

For each GRB, we extract transient-class Pass 8 photons detected with the *Fermi*-LAT between 65 MeV and 500 GeV within 10° of the source. The start time (in UTC) and duration of each burst (reported in Table 4.1) is obtained from the LAT first GRB catalog (Ackermann et al., 2013c), on-line GRB table[2] and individual burst papers (Abdo et al., 2009b; de Palma et al., 2009; Kumar & Barniol Duran, 2010; Ackermann et al., 2011; Tam et al., 2013). There are no diffuse models available at energies less than 65 MeV and the effective area of *Fermi*-LAT decreases steeply at low energies, reducing the overall sensitivity. So, to obtain maximum signal strength, we took 65 MeV as the lower limit for the analysis. The maximal energy must be $\gtrsim$ 10 GeV as photons having energy greater than 10 GeV interact with the EBL to produce electron-positron pairs. The Universe is transparent below ∼10 GeV (Stecker et al., 2006) meaning that the measured spectrum will be equal to the intrinsic spectrum for E < 10 GeV. To retain sensitivity to EBL attenuation, we adopt 500 GeV as the upper limiting energy.

[2] *http* : *//fermi.gsfc.nasa.gov/ssc/observations/types/grbs/lat_grbs/table.php*

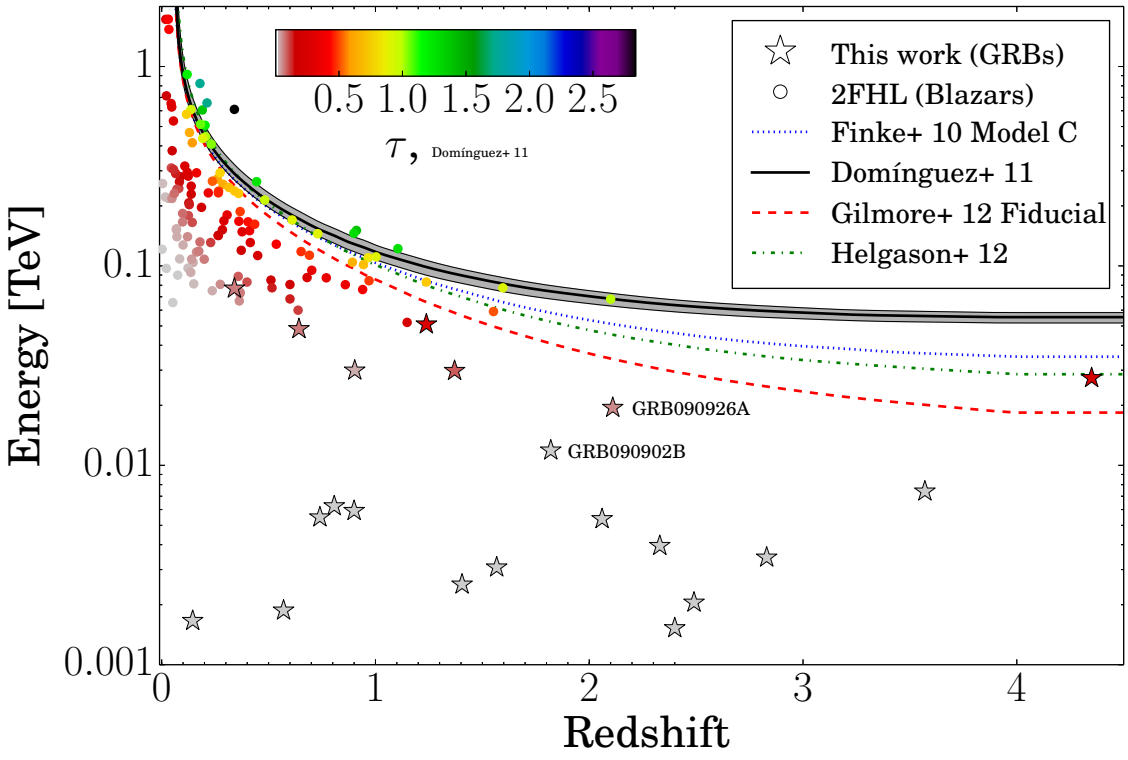

Figure 4.2 Prediction of the cosmic γ-ray horizon (i.e. the redshift and energy at which $\tau_{\gamma\gamma} = 1$) from different models (see legend) along with the highest energy photons from AGNs and GRBs at different redshifts. The GRBs from our sample are denoted by stars, AGNs by dots while the estimates from EBL models are denoted by lines. The two most constraining GRBs in our analysis are labelled in the plot for reference.

The burst data for each GRB are analyzed using *Fermi Science-Tools* (version v10r0p5)[3]. These data are filtered, removing the photons having a zenith angle greater than 105°, to limit the contamination due to Earth's limb (this analysis is robust against changes in zenith angle cuts[4]). The photons collected by the LAT when it is in the South Atlantic Anomaly (SAA) are also filtered out. The spectral analysis of the burst is done by an unbinned likelihood maximization of a sky model created for each GRB. The sky model

[3] *http : //Fermi.gsfc.nasa.gov/ssc/data/analysis/scitools/*
[4] Adopting a more stringent zenith angle cut of 85° produces negligible impact on our analysis.

consists of a central point source, the GRB, whose spectrum is modeled as a power law, and the diffuse (Galactic and isotropic) models. The Galactic and isotropic models are modeled using the gll_iem_v06.fits and iso_P8R2_TRANSIENT020_V6_v06.txt templates[5] respectively (Acero et al., 2016). We use the $P8R2\_TRANSIENT020$ instrument response function.

The Minuit[6] optimizer is used to determine the best-fit spectral parameters and the error estimate for the unbinned likelihood maximization analysis. GRB spectra are generally described using the "Band function" (Band et al., 1993), which consists of two power laws joined by a exponential cut-off, or a Comptonized model, which consists of a power law with exponential cut-off (Ackermann et al., 2013d). According to Ackermann et al. (2013d) and Vianello et al. (2015), the "Band function" alone is inadequate to model GRB spectra over the keV- GeV energy range observed by *Fermi* and a power-law component is required in all bright LAT bursts to account for the high-energy data (> 100 MeV). This component may be produced by synchrotron radiation resulting in a power-law like spectrum (as reported by Tam et al. 2013 and discussed also by Kumar & Barniol Duran, 2009, 2010; Ghisellini et al., 2010; Wang et al., 2010). We thus approximate the intrinsic spectrum of GRBs with a power law and assess in §4.4.2 how well this assumption works.

The power law used for our intrinsic point source spectra is given by

$$\frac{dN_0}{dE} = \frac{N_0(\alpha+1)E^{\alpha}}{E_{max}^{\alpha+1} - E_{min}^{\alpha+1}} \tag{4.1}$$

where N_0 gives the normalized flux in units of $\mathrm{cm}^{-2}\mathrm{s}^{-1}\mathrm{MeV}^{-1}$ between E_{min} and E_{max} taken as 65 MeV and 500 GeV respectively, while α is the photon index. For the likelihood analysis of each GRB, 3 parameters (N_0 and α of the point source and the normalization of the isotropic diffuse source) are left free to vary while the rest are fixed. Because of the short time integration of bursts and lack of photons to constrain both background emissions, the Galactic diffuse emission is fixed. The log likelihood value obtained from the

[5] $http://Fermi.gsfc.nasa.gov/ssc/data/access/lat/BackgroundModels.html$
[6] $http://lcgapp.cern.ch/project/cls/work-packages/mathlibs/minuit/doc/doc.html$

null case (LL_{null}), where the source is not present, is compared with the log likelihood value obtained from the source model (LL) using the Test Statistic (TS) given by $2(LL - LL_{null})$. The TS value along with the estimated flux and photon index are reported, for all GRBs, in Table 4.1. The source significance, which gives us the confidence level for the detection of each GRB, is obtained by taking the square root of the TS value $n_\sigma = TS^{1/2}\sigma$ (Mattox et al., 1996).

4.3 EBL Study

4.3.1 Likelihood Methodology

Our EBL analysis aims to find out the attenuation due to the EBL in the spectra of GRBs. To measure the EBL attenuation, in this work we test separately the normalization and shape of optical depth curves predicted by several EBL models. The normalization of the optical depth is tested following a procedure similar to the one of Ackermann et al. (2012b) by performing the likelihood ratio test (see also Abramowski et al. 2013 and Ahnen et al. 2016), while the shape is tested as discussed in Section 6.4. Owing to the limited signal-to-noise ratio of the measurement within the considered energy range, the shapes of most EBL models are found to be similar to each other (also discussed in Section 6.4). This similarity makes the LAT data more sensitive to the normalization than to the shape of the models. Moreover this approach is compatible (and allows for an easy comparison) with the method adopted also by e.g. MAGIC, H.E.S.S, and VERITAS (Mazin et al., 2017; Abramowski et al., 2013b; Orr, 2011). The EBL absorption is parametrized as $e^{-b\cdot\tau_{model}}$ where the optical depth $\tau_{model}= \tau(E, z)$ is derived by 13 EBL models (see Table 4.3 e.g. Kneiske et al., 2004; Finke et al., 2010; Domínguez et al., 2011; Stecker et al., 2012; Helgason & Kashlinsky, 2012b) and depends on the photon energy E and source redshift z under consideration. This EBL optical depth is scaled to fit the data using the b parameter. The

observed spectrum is then given by:

$$F(E)_{observed} = F(E)_{intrinsic} \cdot e^{-b \cdot \tau_{model}} \tag{4.2}$$

where, $F(E)_{intrinsic} = dN_0/dE$ gives the intrinsic GRB spectrum.

A stacking analysis is used to determine the significance of the EBL attenuation in the observed GRB spectra and to overcome the limitation of low statistics from single GRB sources. In this analysis, the best-fit value of the scaling parameter b is determined through a simultaneous fit to all GRBs. The spectral parameters of each GRB were allowed to vary independently during the fitting with the exception of b (i.e. the scaled EBL attenuation is common to all GRBs) while the parameter of the isotropic component is fixed at its best-fitting value (found analyzing each single ROI) and those of the Galactic model are kept fixed at their nominal, non-optimized, values. Therefore, a total of 45 parameters are left free to vary (2 parameters for each GRB and 1 parameter given by b).

We define two test statistics TS_0 and TS_1 that are used to assess, respectively, the significance of the EBL detection and the inconsistency of a given EBL model with the LAT data. These are defined as $TS_0 = -2[LL(b_{bestfit}) - LL(b = 0)]$ and $TS_1 = -2[LL(b_{bestfit}) - LL(b = 1)]$, where $LL(b_{bestfit})$, $LL(b = 0)$, and $LL(b = 1)$ are the log-likelihoods of when b was left free to vary, and fixed at 0 and 1 respectively. The TS_0 value is obtained by comparing the null case, which indicates no EBL attenuation, to the best-fit case. The significance is calculated using $\sqrt{TS_0}\sigma$ which gives the confidence level for the detection of the EBL attenuation. The TS_1 value represents a measurement of the significance of the rejection of a given EBL model. A high value will mean that the model is rejected as it predicts an attenuation that is larger than observed, with a significance of the model rejection given by $\sqrt{TS_1}\sigma$. We also use the TS_0 and TS_1 to calculate the p values of a χ^2 distribution with one degree of freedom using $p = \int_{TS}^{\infty} d\chi^2 PDF(\chi^2, DOF = 1)$ where PDF stands for probability density function and DOF stands for degrees of freedom.

4.3.2 Results

Out of the 13 EBL models tested, the EBL analysis discussed in § 4.3.1 gave a maximum TS_0 value of 8.04 for the EBL model of Domínguez et al. (2011) with a best-fit value (with $1\,\sigma$ uncertainty) of $b = 2.21^{+1.48}_{-1.83}$. This rules out the absence of EBL attenuation ($b = 0$) at $\sim 2.8\,\sigma$ ($p = 4.6 \times 10^{-3}$). The plot of TS_0 for different b values obtained using the Domínguez et al. (2011) model is shown in Figure 4.3. Note that the major contribution to the TS comes from GRB090902B and GRB090926A. If these two bursts are excluded from the analysis, we obtain a $b = 1.3^{+1.91}_{-1.21}$ and $TS_0 = 3.04$ for the model of Domínguez et al. (2011).

The TS_0 and TS_1 values along with the p_0 and p_1 values, which show the EBL detection and model rejection respectively, for all the EBL models tested in this analysis are reported in Table 4.3. We also report the difference between the significance of detection (TS_0) and the significance of rejection (TS_1). Using the definitions of TS_0 and TS_1 it is easily seen that their difference will be given by $\Delta TS = -2[LL(b = 0) - LL(b = 1)]$. ΔTS represents the improvement in the fit when the nominal (for a given EBL model) estimate of the EBL attenuation is used with respect to the case of no EBL attenuation. A higher value will imply a more significant detection of the EBL at the level nominally derived by the model being tested. The EBL models accepted by our analysis are the models having TS_1 less than 9, meaning that the model is accepted within a $3\,\sigma$ confidence level. So all the EBL models shown in Table 4.3 are compatible with the *Fermi*-LAT GRB data. For most of the models, the average TS_0 is around $\sim$7.3.

4.4 Tests for Systematic Effects

4.4.1 Intrinsic Spectral Curvature

A spectral break was first seen in GRB 090926A at a cut-off energy of ~ 1.4 GeV (Ackermann et al., 2011). Recently, Tang et al. (2015) found 6 GRBs showing similar spectral features with cut-off energies ranging from $\sim$10 to $\sim$500 MeV (much lower than the

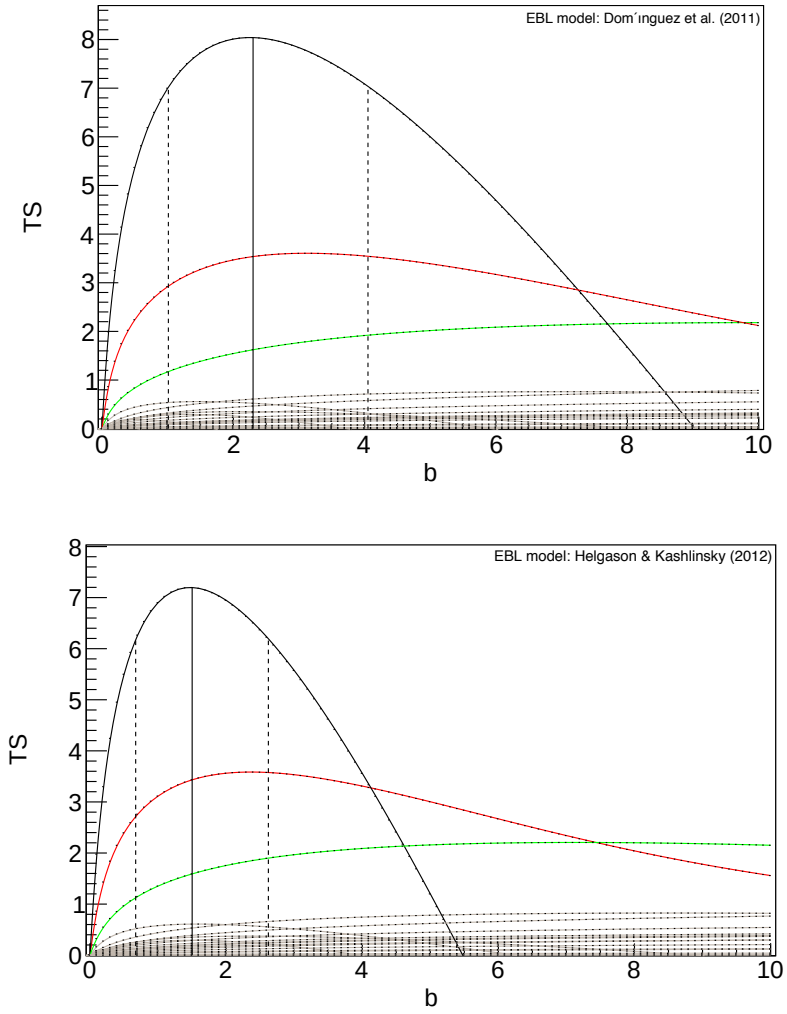

Figure 4.3 A combined measurement (shown by a solid black line) of the TS_0 values of twenty-two GRBs as a function of b is displayed for the EBL models of Domínguez et al. (2011) (top) and Helgason & Kashlinsky (2012b) (bottom) along with the measurements for individual GRBs. The solid red and green lines show the maximum contributions to the EBL analysis obtained from GRB090902B and GRB090926A respectively while the solid gray lines show contributions from the remaining 20 GRB sources. The best fit value for the scaling parameter with $1\,\sigma$ uncertainty values is also shown by the vertical solid and dashed lines respectively.

energy at which EBL attenuation takes place). To assess the impact of intrinsic spectral curvature on our EBL analysis, we performed a series of tests modeling the intrinsic source spectrum with a power law with an an exponential cut-off component, modeled as e^{-E/E_C},

dependent on cut-off energy (E_C). The individual source spectrum used for all the GRBs in the likelihood fit is given by:

$$\frac{dN}{dE} = N_0 \left(\frac{E}{E_0}\right)^{\gamma} \exp\left(-\frac{E}{E_c}\right) \tag{4.3}$$

where N_0 is the normalization in units of $\mathrm{cm}^{-2}\mathrm{s}^{-1}\mathrm{MeV}^{-1}$, γ is the index, E_0 is the scaling energy fixed at 200 MeV and E_C is the cut-off energy. In the source spectrum, N_0, γ and E_C are left free to vary while for the isotropic diffuse source, the normalization parameter is left free.

In the first test, EBL attenuation is included at the nominal value using Finke et al. (2010), model-C, owing to the low uncertainty and high TS_0 values obtained from our analysis. The scaling parameter (b) for the EBL model is fixed at 1. So, in all, 4 parameters are optimized for each GRB. The maximum likelihood is compared with the likelihood obtained by fixing the cut-off energy at 3 TeV, which is outside the *Fermi*-LAT energy range and is thus equivalent to having no cut-off in the GRB spectrum (i.e. a simple power-law spectrum). The Test statistic value obtained from this comparison is denoted by TS_C and is used to evaluate the presence of a cut-off in the GRB spectra.

The TS_C value for GRB 090926A is found to be 0.7 from our analysis, which results in a null detection of curvature in the integrated spectrum. This result is different from Ackermann et al. (2011) because we used a longer time interval (4889 seconds) for the GRB sample as compared to the "prompt" interval (3-21 seconds) used by Ackermann et al. (2011). A TS_C value greater than 1.9 is found for only two of the twenty-two GRBs in our sample. GRB 120624 has a TS_C value of 3.24 and a best-fit value of 1.23 GeV for the cut-off energy and GRB 131108 has a TS_C value of 4.02 and a best-fit value of 1.13 GeV. The cut-off energies found for both GRBs are significantly lower than the energy at which EBL attenuation takes place, and modeling these two sources as exponentially absorbed power laws has negligible impact on the significance of the detection of the EBL attenuation reported in Table 4.3.

Secondly, we repeated the above test, adopting an energy range that is restricted

for every GRB so that the EBL attenuation is negligible[7]. In this way our analysis of the curvature of the GRB intrinsic spectra is not affected by EBL attenuation. This confirms the results of the previous analysis, deriving a TS_C of 3.54 and 4.16 for GRB 120624 and GRB 131108. Again modeling the spectra of these sources to include the exponential cut-off has negligible impact on the EBL.

Thirdly, if the curvature of the intrinsic spectrum were not well modeled (by e.g. neglecting exponential cut-offs), this effect would be visible as a shift to lower values of the best-fitting b parameter as a function of increasing minimum energy adopted in the analysis. We thus repeated the entire analysis adopting a minimum energy of 1 GeV (instead of 65 MeV) and measured a TS_0=5.9 and $b = 1.20^{+1.50}_{-0.85}$ for the Finke et al. (2010) model, which is in very good agreement with the results in Table 4.3. This again shows that modeling the intrinsic GRB spectra with a power law is a reasonable assumption and that intrinsic curvature, if present, is not biasing the result of this analysis.

Finally, we also computed the TS_0 and b values for the Finke et al. (2010) model modeling all the GRB intrinsic spectra with an exponentially cut-off power law. A TS_0 of 0.87 with a $b = 0.53$ was obtained, which is significantly lower than the result found using a simple power-law model as an intrinsic spectrum for all GRBs (See Table 4.3). However this model employs twenty-two additional free parameters (a cut-off energy per source) while producing a similar log-likelihood as the EBL absorbed power-law model. Model simplicity leads us to prefer the scenario where the power-law emission of GRBs is attenuated by the EBL (a phenomenon already observed in BL Lacs) rather than a more complex intrinsic spectrum. This leads us to conclude that for the EBL analysis using GRBs, a simple power-law spectrum is a reasonable assumption and it is statistically preferred, globally, over an exponentially cut-off power-law spectrum.

[7]Each spectrum was fitted up to a maximum energy that is derived from each GRB when the attenuation, as predicted from Finke et al. (2010), is negligible ($< 5\,\%$).

4.4.2 Time resolved spectral analysis

GRBs are known to display substantial spectral evolution during the prompt phase (Zhang et al., 2011; Ackermann et al., 2013b). This calls for an additional time-resolved spectral analysis to justify the usage of time-integrated spectra for the detection of EBL attenuation (Guiriec et al., 2017). We again use Finke et al. (2010)-model C as the EBL model for this test. Again we choose GRB 090902B for this test owing to its relatively high contribution to the TS_0 value. The spectrum of GRB 090902B is created for 7 separate time binned intervals obtained from Abdo et al. (2009a). We use a simple power law to model the intrinsic spectrum for each time bin. The process discussed in Section 6.2 and 4.3.1 is followed to obtain TS_0 as a function of b for each time bin. These results are stacked together to obtain a final combined value of $TS_0 = 3.4$ corresponding to a best fit $b = 1.9^{+3.9}_{-1.4}$ in agreement to the time-integrated result of $TS_0 = 3.5$ and $b = 1.8^{+2.8}_{-1.3}$ obtained from Section 4.3. This agreement shows that using time integrated spectra of GRBs does not have any impact on the detection of the EBL attenuation.

4.5 Conclusion

The interaction of γ rays from sources at cosmological distances (e.g. GRBs, blazars, radio galaxies and star forming galaxies) with EBL photons creates electron-positron pairs causing absorption of γ rays (Stecker et al., 2006). Using *Fermi*-LAT we searched for the imprint of the EBL in the spectra of twenty-two GRBs detected by the LAT and for which redshift measurements exist. The low number of photons detected from each single GRB at high energy, predominantly due to the steep decline (with energy) of the LAT effective area, renders the detection of the EBL attenuation in the spectrum of a single source challenging. To overcome this, we analyze the combined set of GRB spectra (stacking) which allows us to reject the null hypothesis of no EBL attenuation at $\sim 2.8\,\sigma$ confidence.

The constraint on the γ-ray optical depth as derived from this analysis is reported in Figure 4.4. We report this constraint for an effective redshift of $\sim$1.8. This value is derived

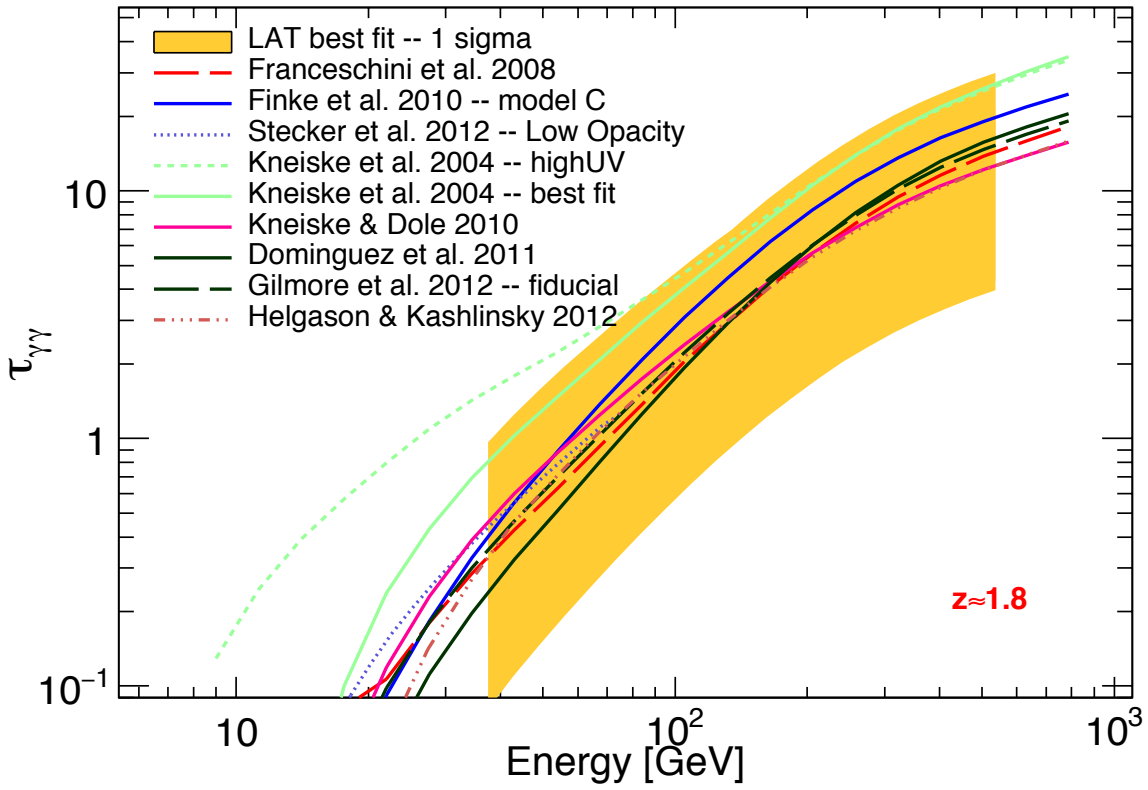

Figure 4.4 Constraint on the optical depth at a redshift of $z \sim 1.8$, at $1\,\sigma$ confidence level (68%), derived for our GRB sample, compared with model estimates. The models of Franceschini et al. (2008) and (Stecker et al., 2012, high and low opacity), not included in the numerical analysis (mentioned in Sec. 4.3), are included in the figure for completeness.

by separating the source sample into two redshift bins and finding the value of the redshift separating the bins for which the TS_0 is similar in both bins. This helps us to identify the effective redshift based on the contribution from each GRB. Moreover, dividing the source sample into redshift bins of $0 < z < 1.8$ and $1.8 < z < 4.35$, $TS_0 = 2.45$ for $0 < z < 1.8$ and $TS_0 = 5.78$ for $1.8 < z < 4.35$ are obtained, while dividing it into bins of $0 < z < 1.9$ and $1.9 < z < 4.35$ gives $TS_0 = 5.82$ and 2.18 respectively. This additional test shows that the effective redshift of our sample is $z \sim 1.8$. Also, if GRB090902 at redshift 1.82 is removed

from the sample, then the TS values for both the redshift bins are close to equal. This effective redshift is slightly higher than the sample average of 1.63 reflecting the leverage gained by the high-redshift sources in our sample. Figure 4.4 demonstrates that all the recent EBL models that are in agreement with galaxy counts are also in agreement with the *Fermi*-LAT constraint. The γ-ray horizon (τ=1) at this effective redshift occurs in the range 40 to 180 GeV, consistent with the range found by Domínguez et al. (2011) and Ackermann et al. (2015a). As the GRB results are found to be consistent with those derived for BL Lacs, we conclude that secondary γ-rays are not important for moderate optical depths ($\tau \sim 1$), as also argued by Biteau & Williams (2015) and Domínguez & Ajello (2015).

The constraints reported in our analysis can also be combined with those reported by Ackermann et al. (2012b) that relied on 150 BL Lacs. These are reported in Table 4.4. While the baseline model of Stecker et al. (2006) and the "high-UV" model of Kneiske et al. (2004) were already found inconsistent with the *Fermi*-LAT BL Lac data, we now find that also the "best-fit" model of Kneiske et al. (2004) is ruled out at the $3\,\sigma$ level when compared to the combined *Fermi*-LAT GRB and BL Lac data.

Photons of energy $\lesssim$100 GeV and from redshift $z > 1$ interact preferentially with photons of the UV background. These deviations are appreciated in Figure 4.5, which shows the models of Table 4.4 renormalized to fit the *Fermi* data. It is apparent that all best-fitting (renormalized) models occupy a narrow region of the τ *vs* energy plot. The optical depth curve predicted by the "high-UV" model of Kneiske et al. (2004) has a shape which is markedly different than the rest of the models, over-predicting the optical depth at <60 GeV and under-predicting it above that energy. This clearly shows that the *Fermi*-LAT offers the capability to probe the UV background at redshifts $\sim$2, a cosmic epoch during which the star formation rate density was near maximum (Madau et al., 1996; Bouwens et al., 2015a).

So far studies have been limited to re-normalizing the EBL models to fit γ-ray data (Ackermann et al., 2012b; Abramowski et al., 2013b). This analysis shows that the shape of the optical depth curve of some models may be better than others, even when renormalized

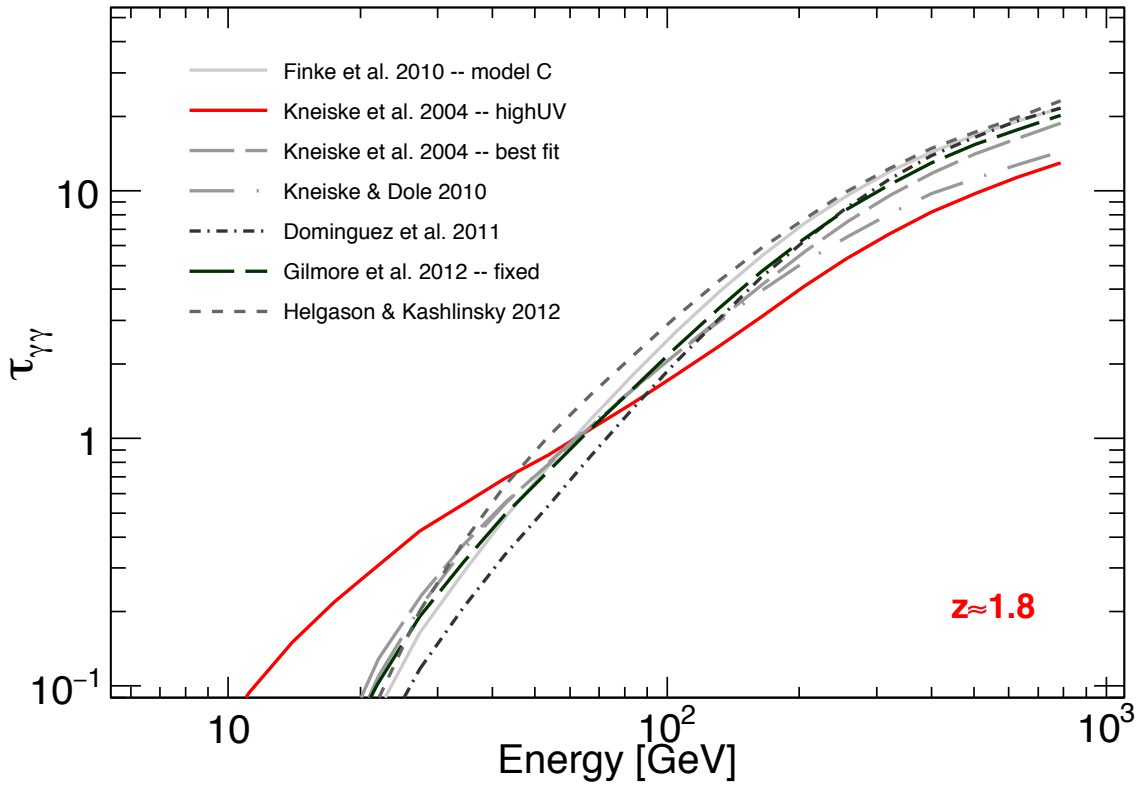

Figure 4.5 EBL models renormalized to fit the *Fermi*-LAT data. The high-UV model of Kneiske et al. (2004) can be rejected (at $3\,\sigma$ level) on the basis of the shape of its predicted optical depth curve.

to fit the LAT data. For example, the Kneiske et al. (2004)−˘high UV model implies a significantly different shape, particularly in the UV (and correspondingly 10-50 GeV), as can be seen from Figure 4.5. In our analysis we allowed every model to be rescaled by a wavelength-independent factor. Because of the SED shape differences, some models produce significantly better fits than others even after one allows for different renormalization factors. This indicates that the analysis presented here is sensitive to the energy dependence of the EBL thus providing a valuable diagnostic tool. This can be assessed by taking differences of

TS_0 values in Table 3. For example the shape (not the normalization) of the optical depth curve as derived by Domínguez et al. (2011) is better than the one of the "high-UV" model of Kneiske et al. (2004) at $\Delta\mathrm{TS}_0$=10.4. However, because the models are not nested, one needs to calibrate the probability of observing $\Delta\mathrm{TS}_0$=10.4, or larger, by chance. We used Monte Carlo simulations of a set of 22 GRBs whose spectra have been attenuated by the EBL as predicted by the high-UV model Kneiske et al. (2004). Figure 4.6 shows the distribution of $\Delta\mathrm{TS}_0$ defined as the difference between the TS_0 produced with the Kneiske et al. (2004) high-UV model and the Domínguez et al. (2011) model. We derive that a $\Delta\mathrm{TS}_0 > 10.4$ is observed in $\sim 1\,\%$ of the cases corresponding to a $3\,\sigma$ evidence that the shape of the optical depth is better represented by the Domínguez et al. (2011) model rather than the high-UV model of Kneiske et al. (2004). This and Figure 4.5 show that the LAT is mostly sensitive to the EBL in the UV band, which is traditionally a very difficult component to model and understand because of the absorption of light in star-forming galaxies (Helgason & Kashlinsky, 2012b).

We have shown for the first time that a combined sample of GRBs can be used as an excellent probe of the EBL. The analysis presented here is based on the relatively small sample of twenty-two GRBs with known redshifts. However, if we scale the significance of the EBL attenuation by the number of sources, GRBs appear to have more constraining power than the BL Lacs used in Ackermann et al. (2012b). This is due to their more simple intrinsic spectrum and high signal-to-noise spectra that are accumulated over a very short time, as well as higher redshift as compared to BL Lacs in Ackermann et al. (2012b). Thus, it is desirable to extend our analysis to a larger burst sample underlining the importance of obtaining redshift determinations for future GRBs.

Table 4.1. GRB used for analysis (GRBs are sorted increasingly by the time of the event)

GRB Name	Date (MST)	R.A. Deg., J2000.0	Decl Deg., J2000.0	Redshift	T start (UTC)	Duration seconds [a]	Flux (10^{-5}) [b] ph·cm^{-2}·s^{-1}	Photon index [b]	TS [b]
080916C	16 September 2008	119.85	−56.60	4.35	00:12:45.6	1775.9	7.89±0.49	2.25±0.06	1140.7
090323	23 March 2009	190.71	17.10	3.57	00:02:42.6	5615.9	1.42±0.19	2.28±0.13	205.0
090328	28 March 2009	90.67	−42.00	0.74	09:36:46.5	7485.6	0.52±0.07	2.10±0.11	253.6
090510	10 May 2009	333.55	−26.60	0.90	00:22:59.9	177.8	34.11±2.11	2.05±0.05	1234.6
090902B	2 September 2009	264.94	27.32	1.82	11:05:08.3	749.5	14.32±0.70	1.91±0.04	2219.0
090926A	26 September 2009	353.40	−66.32	2.11	04:20:26.9	4889.3	4.61±0.28	2.08±0.05	1267.2
091003	3 October 2009	251.52	36.63	0.90	04:35:45.5	451.6	2.17±0.40	2.04±0.15	192.3
100414A	14 April 2010	192.11	8.69	1.37	02:20:21.9	5622.5	0.39±0.07	1.77±0.11	188.8
100728A	28 July 2010	88.76	−15.26	1.57	02:17:30.6	693.7	0.65±0.19	1.92±0.21	69.9
110731A	31 July 2011	280.50	−28.54	2.83	11:09:29.9	561.3	3.20±0.45	2.22±0.12	194.3
120624B	24 June 2012	170.87	8.93	0.57	22:23:53.0	1104.3	3.86±0.35	2.46±0.10	456.3
120711A	11 July 2012	94.69	−71.00	1.41	02:44:53.0	5307.2	0.56±0.12	1.93±0.15	136.7
130427A	27 April 2013	173.14	27.71	0.34	07:47:6.0	10000	4.19±0.18	1.99±0.03	2755.8
130518A	18 May 2013	355.67	47.47	2.49	13:54:37.0	302.9	5.38±0.94	2.54±0.19	106.0
130702A	2 July 2013	217.31	15.77	0.15	00:05:23.0	384.5	0.04±0.02	1.56±0.32	42.8
130907A	7 September 2013	215.89	45.61	1.24	21:42:19.0	16600	0.91±0.56	2.10±0.46	12.8
131108A	8 November 2013	156.50	9.66	2.40	20:41:55.0	1333.5	4.52±0.32	2.63±0.09	559.0
131231A	31 December 2013	10.59	−1.65	0.62	04:45:16.1	5605.6	0.34±0.07	1.73±0.12	229.1
141028A	28 October 2014	322.60	−0.23	2.33	10:55:03.08	414.2	2.33±0.50	2.22±0.21	86.7
150314A	14 March 2015	126.68	63.83	1.76	04:54:50.0	250	2.24±0.88	2.66±0.41	19.4
150403A	3 April 2015	311.51	−62.71	2.06	21:54:10.9	1678.3	0.22±0.08	1.87±0.23	42.1
150514A	14 May 2015	74.88	−60.91	0.81	18:35:05.4	600	0.09±0.07	1.30±0.42	28.3

[a]Duration of the GRB considered for our analysis.

[b]Parameters obtained from analysis described in Section 6.2

Table 4.2. Photons detected by the *Fermi*-LAT at an optical depth greater than 0.1

GRB Name	Redshift	Number of photons Finke et al. (2010) [a]	Number of photons Domínguez et al. (2011) [b]	Number of photons Kneiske & Dole (2010) [c]	Corresponding energy of photons (GeV) [d]
080916C	4.35	2	0	2	12.4,27.4
090323	3.57	0	0	0	–
090328	0.74	0	0	0	–
090510	0.90	0	0	0	–
090902B	1.82	2	0	2	39.9,21.7
090926A	2.11	1	0	1	19.5
091003	0.90	0	0	0	–
100414A	1.37	1	0	2	29.8
100728A	1.57	0	0	0	–
110731A	2.83	0	0	0	–
120624B	0.57	0	0	0	–
120711A	1.41	0	0	0	–
130427A	0.34	1	3	2	94.1
130518A	2.49	0	0	0	–
130702A	0.15	0	0	0	–
130907A	1.24	1	0	1	50.9
131108A	2.40	0	0	0	–
131231A	0.62	0	0	1	–
141028A	2.33	0	0	0	–
150314A	1.76	0	0	0	–
150403A	2.06	0	0	0	–
150514A	0.81	0	0	0	–

[a]Number of LAT Photons detected at $\tau > 0.1$ (obtained using EBL model Finke et al. (2010)$-modelC$).

[b]Upper limit of the number of LAT Photons detected at $\tau > 0.1$ (obtained using EBL model Domínguez et al. (2011)).

[c]Lower limit of the number of LAT Photons detected at $\tau > 0.1$ (obtained using EBL model Kneiske & Dole (2010)).

[d]Energy of the photons detected at $\tau > 0.1$ (obtained using EBL model Finke et al. (2010)$-modelC$).

Table 4.3. Joint-likelihood results for different EBL models using GRB sources.

Model	TS_0[a]	p_0[b]	b[c]	TS_1[d]	p_1[b]	ΔTS[e]
Kneiske et al. (2004) – high UV	6.5	2.55	$0.43^{+0.24}_{-0.28}$	3.5	1.87	3.0
Kneiske et al. (2004) – best-fit	7.4	2.72	$0.80^{+0.51}_{-0.61}$	0.1	0.32	7.3
Primack et al. (2005)	4.7	2.17	$0.51^{+0.34}_{-0.38}$	1.5	1.22	3.2
Gilmore et al. (2009)	7.1	2.66	$1.25^{+0.82}_{-0.95}$	0.1	0.32	7.0
Finke et al. (2010) – model C	7.7	2.77	$1.27^{+0.84}_{-0.99}$	0.1	0.32	7.6
Kneiske & Dole (2010)	7.4	2.72	$1.29^{+0.80}_{-0.95}$	0.2	0.45	7.2
Domínguez et al. (2011)	8.0	2.83	$2.21^{+1.48}_{-1.83}$	1.0	1.00	7.0
Gilmore et al. (2012) – fixed	7.3	2.70	$1.43^{+0.93}_{-1.13}$	0.3	0.55	7.0
Gilmore et al. (2012) – fiducial	6.5	2.55	$0.63^{+0.40}_{-0.46}$	0.7	0.84	5.8
Helgason & Kashlinsky (2012b)	7.2	2.68	$1.44^{+0.95}_{-1.18}$	0.3	0.55	6.9
Scully et al. (2014) – Low Opacity	6.9	2.62	$1.16^{+0.69}_{-0.79}$	0.1	0.32	6.8
Scully et al. (2014) – High Opacity	6.7	2.59	$0.42^{+0.25}_{-0.29}$	3.3	1.82	3.4
Inoue et al. (2013)	6.4	2.53	$0.72^{+0.43}_{-0.50}$	0.4	0.63	6.0

[a]TS obtained from the comparison of the null hypothesis (b=0) with the likelihood obtained with best-fit value for b.

[b]The p_0 and p_1 values are denoted in units of standard deviation of a normal Gaussian distribution.

[c]This column lists the best-fit values and $1\,\sigma$ confidence ranges for the opacity scaling factor.

[d]Here the compatibility of the predictions of EBL models with the *Fermi* observations is shown (b=1 case constitutes the null hypothesis). Large values mean less likely to be compatible.

[e]$\Delta TS = TS_0 - TS_1$

Table 4.4. Combined results of GRB and BL Lac sources for different EBL models.

Model[a]	TS_0 [b]	p_0[c]	b[d]	TS_1 [e]	p_1[c]	ΔTS[f]
Kneiske et al. (2004) – high UV	32.5	5.70	0.38±0.08	38.3	6.19	-5.8
Kneiske et al. (2004) – best-fit	41.0	6.40	0.54±0.12	10.4	3.22	30.6
Primack et al. (2005)	35.0	5.91	0.73±0.14	5.0	2.23	30.0
Gilmore et al. (2009)	40.7	6.38	0.99±0.21	0.1	0.32	40.6
Finke et al. (2010) – model C	41.3	6.43	0.88±0.22	0.3	0.55	41.0
Kneiske & Dole (2010)	39.9	6.32	0.92±0.18	0.19	0.44	39.7
Domínguez et al. (2011)	42.8	6.54	1.04±0.23	0.04	0.20	42.8
Gilmore et al. (2012) – fixed	40.7	6.38	1.04±0.22	0.04	0.20	40.7
Gilmore et al. (2012) – fiducial	40.1	6.33	0.92±0.20	0.16	0.40	39.9

[a]Only models common to Ackermann et al. (2012b) and our analysis are listed here.

[b]Same as table 2 but combined TS obtained from GRB and BL Lac observations

[c]The p_0 and p_1 values are denoted in units of standard deviation of a normal Gaussian distribution.

[d]Maximum likelihood values and uncertainty obtained by performing a weighted average of GRB and BL Lac data

[e]Same as table 2 but combined TS obtained from GRB and BL Lac observation.

[f]$\Delta TS = TS_0 - TS_1$

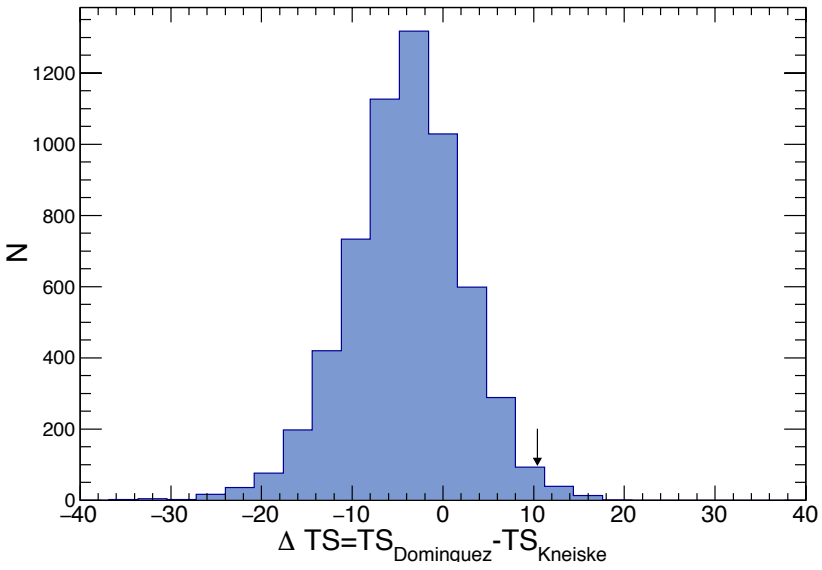

Figure 4.6 Distribution obtained from simulations of the ΔTS, when comparing the TS_0 of two different models, in the null hypothesis regime. In this case the simulation adopted the high-UV EBL model of Kneiske et al. (2004). The arrow shows the ΔTS=10.4 value observed in the real data (see Table 4.4).

Chapter 5

EBL measurements using AGN observed using the*Fermi*-LAT

As seen is the Chapter 4, it is highly beneficial to constrain the EBL using GRBs however due to their low sample size and comparatively fewer detected gamma ray photons at low redshifts, blazars can still be used as a primary source for probing the EBL. The GRBs still can offer very valuable insight at higher redshifts where there are almost no detected gamma ray photons from Blazars. A combined GRB+Blazar sample, takes care of all these shortcomings and provide the ideal measurement of the EBL optical depth both at high and low redshifts. Our collaborative work, The Fermi-LAT Collaboration (2018), makes use of such a sample to determine not only the EBL optical depth and correspondingly the EBL intensity, but also the star formation rate of the Universe. This work made use of 759 blazars in a combined stacking analysis similar to the one described in Section 4.3, to determine the EBL optical depth in a redshift (z) range of $0.03 < z < 3.1$ distributed across 12 redshift bins. This, along with the EBL optical depth measurement made using GRB 080916C at $z = 4.35$ (see Chapter 4), allowed us to reconstruct the EBL intensity at distinct epochs. The reconstructed EBL was consequently used to determine the Star Formation History of the Universe (with strong constrains up-to $z \approx 5$) using two independent methods combined with extrapolation techniques. This chapter is taken from, The Fermi-LAT Collaboration

(2018). Reprinted with permission from AAAS

5.1 Main Text of Article

Stars produce the bulk of the optical light in the Universe and synthesize most of the elements found in galaxies. The cosmic star-formation history (SFH), i.e. the stellar birth rate as a function of the Universe's age, summarizes the history of stellar formation since the Big Bang (Madau & Dickinson, 2014). The rate of star formation is commonly estimated by measuring direct emission of light from massive short-lived stars, typically in the ultraviolet (UV) and (or) by detecting the reprocessed radiation from dusty star-forming regions in the infrared (IR). The conversion from the UV light emitted by a minority of stars to the stellar mass formed per year relies on assumptions about the mass distribution of the newly formed stellar population (the initial mass function, IMF), the element enrichment history of the interstellar medium, and obscuration by dust. Such estimates of the SFH rely on the detection of many individual galaxies in deep surveys (Grogin et al., 2011; Illingworth et al., 2013; Lotz et al., 2017). Because not even the most powerful telescope can detect all the galaxies in a representative field, one of the largest sources of uncertainty in the SFH is estimating the amount of light from undetected galaxies, and the star formation associated with them. This difficulty becomes particularly relevant within the first billion years after the Big Bang when a large population of faint, still undetected, galaxies existed (McLure et al., 2013). These galaxies are expected to drive the re-ionization of the Universe: the period when energetic UV photons from young stars escaped into intergalactic space and ionized the neutral hydrogen of the intergalactic medium. Similarly, recent (i.e. within one billion years from the present age) star formation measured using space-borne UV observatories is based on surveys extending over small solid angles (Schiminovich et al., 2005), and are therefore subject to density fluctuations in the large-scale structure, an effect known as cosmic variance.

Observational estimates of the SFH are sufficiently uncertain that measurements

with multiple independent methodologies are desirable. Starlight that escapes galaxies is almost never destroyed and becomes part of the extragalactic background light (EBL), the total light accumulated by all sources over the lifetime of the Universe (Hauser & Dwek, 2001; Kashlinsky, 2005; Dwek & Krennrich, 2013). While extremely important, accurate measurements of this diffuse all-sky background at UV to IR wavelengths, and particularly its build-up over time, have only just become possible (Andrews et al., 2017).

We present an alternative approach to measure the SFH based on the attenuation that the EBL produces in the γ-ray spectra of distant sources. γ rays with sufficient energy can annihilate when they collide with EBL photons and produce electron-positron pairs (i.e. the reaction $\gamma\gamma \rightarrow e^{+}e^{-}$), effectively being absorbed as a result of the interaction (Nikishov, 1962). Above a given threshold energy, the attenuation experienced by every γ-ray source at a similar distance depends on the number density of the EBL target photons integrated along the line of sight; observations of γ-ray sources at different distances (as measured by the sourcesâ redshifts) can be used to measure the density of EBL photons at different cosmic times.

We analyze γ-ray photons detected by the Large Area Telescope (LAT) instrument on the *Fermi* Gamma-ray Space Telescope, over 9 years of operations. Our sample of suitable objects for this analysis consists of 759 blazars, galaxies hosting a super-massive black hole with a relativistic jet pointed at a small angle to the line of sight. The distances of these blazars correspond to lookback times of 0.2-11.6 billion years according to the standard cosmological model [1] We perform a likelihood analysis to find the EBL attenuation experienced by all blazars whilst simultaneously optimizing the spectral parameters independently for each blazar (Ackermann et al., 2012b). This is accomplished individually for each source, by defining a region of interest that comprises all γ rays detected within 15° of the source position and creating a sky model that includes all sources of γ rays in the field. The parameters of the sky model are then optimized by a maximum likelihood method. For every blazar, the fitting is performed below an energy at which the EBL attenuation is

[1]We adopted the following values for the Hubble and cosmological parameters: H_0=70 km s^{-1} Mpc^{-1}, Ω_M=0.3, and Ω_Λ=0.7.

negligible and thus yields a measurement of the intrinsic (i.e., unabsorbed) blazar spectrum. The intrinsic spectra are described using simple empirical functions [2] and extrapolated to higher energy, where the γ rays are expected to be attenuated by the EBL.

Potential EBL absorption is added to the fitted spectra as follows:

$$\left(\frac{\mathrm{dN}}{\mathrm{dE}}\right)_{obs} = \left(\frac{\mathrm{dN}}{\mathrm{dE}}\right)_{int} \times e^{-b\cdot\tau_{\gamma\gamma}(E,z)} \tag{5.1}$$

where $\left(\frac{\mathrm{dN}}{\mathrm{dE}}\right)_{obs}$ and $\left(\frac{\mathrm{dN}}{\mathrm{dE}}\right)_{int}$ are the observed and intrinsic blazar spectra respectively, $\tau_{\gamma\gamma}(E,z)$ is the EBL optical depth as estimated from models (at a given energy E and redshift z) and b is a free parameter. The data from all blazars are combined to yield the best-fitting value of b for each model. A value of $b = 0$ implies no EBL attenuation is present in the spectra of blazars, while $b \approx 1$ implies an attenuation compatible with the model prediction. Twelve of the most recent models that predict the EBL attenuation up to a redshift of $z = 3.1$ have been tested in this work. We detect the attenuation due to the EBL in the spectra of blazars at $\gtrsim 16$ standard deviations (σ) for all models tested (see Table S2).

Our analysis leads to detections of the EBL attenuation across the entire $0.03 < z < 3.1$ redshift range of the blazars. From this, we identify the redshift at which, for a given energy, the Universe becomes opaque to γ rays, known as cosmic γ-ray horizon (Figure 5.1). With the optical depths measured in six energy bins ($10 - 1000$ GeV) across twelve redshift bins (see Supplementary Materials) we are able to reconstruct the intensity of the EBL at different epochs (Figure 6.3). We model the cosmic emissivity (luminosity density) of sources as several simple spectral components at UV, optical, and near-IR (NIR) wavelengths. These components are allowed to vary in amplitude and evolve with redshift independently of each other to reproduce, through a Markov Chain Monte Carlo (MCMC) analysis, the optical depth data. The emissivities as a function of wavelength and redshift allow us to reconstruct the history of the EBL over $\sim 90\,\%$ of cosmic time.

At $z = 0$ the energy spectrum of the EBL is close to the one inferred by resolving in-

[2] Materials and methods are available as supplementary materials on Science Online.

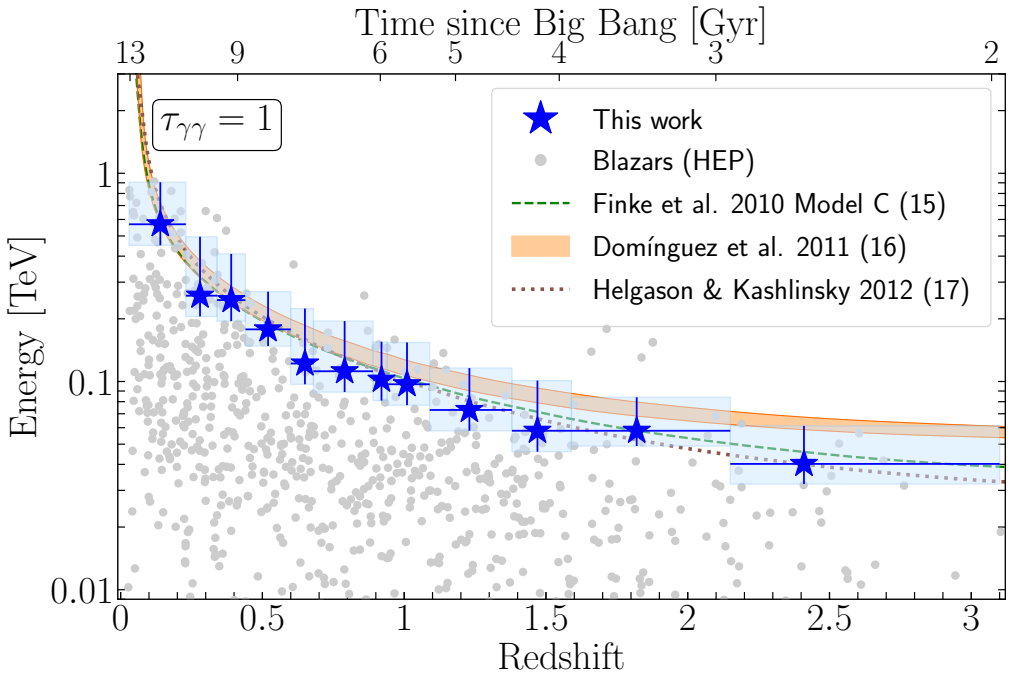

Figure 5.1 The cosmic γ-ray horizon. Measurement of the cosmic γ-ray horizon ($\tau_{\gamma\gamma} = 1$, i.e. the point after which the Universe becomes opaque to γ rays) as a function of redshift (blue stars and boxes, the latter representing the redshift bin size and the uncertainty on the energy) compared with predictions from three different EBL models (Finke et al., 2010; Domínguez et al., 2011; Helgason & Kashlinsky, 2012b). The gray points show the highest-energy photon (HEP) detected from each blazar considered in this work.

dividual galaxies in deep fields (Driver et al., 2016). At all other epochs, *Fermi* LAT is most sensitive to the UV-optical component of the EBL, and is only able to constrain the NIR component at more recent times (see Figure 6.3). The intensity of the UV background in the local Universe remains uncertain, with independent studies reporting differing values (Gardner et al., 2000; Xu et al., 2005; Voyer et al., 2011). Our determination of $2.56^{+0.92(2.23)}_{-0.87(1.49)}$ nW m^{-2} sr^{-1}, $1\sigma(2\sigma)$, at 0.2 μm favors an intermediate UV intensity in agreement with Voyer et al. (2011). In the NIR our measurement of $11.6^{+1.3(2.6)}_{-1.4(3.1)}$ nW m^{-2}sr^{-1}, 1σ (2σ), at 1.4 μm is consistent with integrated galaxy counts (Keenan et al., 2010; Ashby et al., 2013), leaving little room for additional components, contrary to some suggestions (Bernstein, 2007; Matsuura et al., 2017). This notably includes contributions from stars that have been stripped

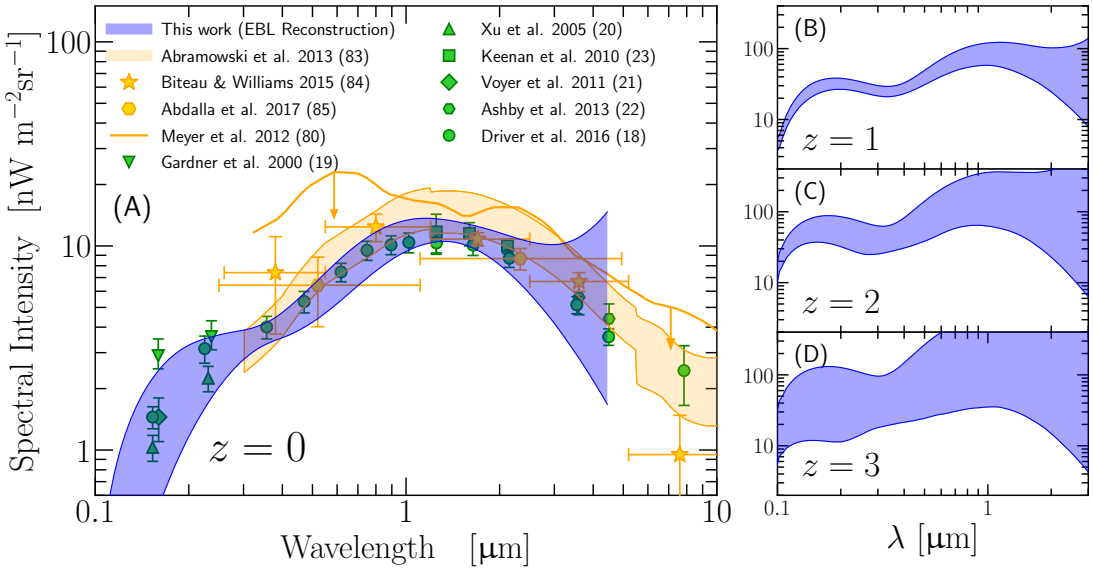

Figure 5.2 The spectral intensity of the EBL in the Universe today (A) and at redshifts $z = 1, 2, 3$ (B, C, and D). At $z = 0$ data from other γ-ray based measurements (orange symbols, see legend) and integrated galaxy counts (green symbols, see legend) are displayed. The blue areas show the $1\,\sigma$ confidence regions based on the reconstructed cosmic emissivity (see Supplementary Materials). At higher redshift (B, C, and D), the EBL is shown in physical coordinates. Figure 5.12 in Supplementary Materials includes a more complete set of measurements from the literature.

from galaxies as the technique presented here is sensitive to all photons (Zemcov et al., 2014; Burke et al., 2015).

At any epoch, the EBL is composed of the emission of all stars [3] that existed up to that point in time and can therefore be used to infer properties related to the evolution of galaxy populations. We focus on the cosmic SFH, which we determine using two independent methods. First, we use the reconstructed UV emissivity across cosmic time to derive the SFH from established relations between the UV luminosity and star-formation rate (Kennicutt Jr., 1998), taking into account the mean dust extinction within galaxies (Bouwens et al., 2012; Burgarella et al., 2013; Andrews et al., 2017). The second approach uses a physical EBL model of Finke et al. (2010) to calculate the optical depth due to the EBL directly from the SFH. The SFH is then optimized using a MCMC to reproduce the *Fermi*-LAT optical depth data (see Supplementary Materials). The two approaches yield consistent results for the SFH, which is well constrained out to a redshift of $z \approx 5$, i.e., to the epoch 1.5 billion years after the Big Bang (Figure 5.3).

Because the optical depth increases with the distance traveled by the γ rays, we obtain the tightest constraints in the redshift range $0.1 < z < 1.5$, beyond which our sensitivity decreases due to the lower number of observed blazars. To improve the constraint of the SFH beyond $z = 3$, we have complemented the blazar sample with a gamma-ray burst (GRB 080916C) at $z = 4.35$ (Abdo et al., 2009b). This allows us to place upper limits on the SFH at $z \gtrsim 5$, because photons generated at redshifts higher than the $z = 4.35$ limit of our sample remain in the EBL, become redshifted, and start interacting with the γ rays from the blazars and the GRB used here at $z < 4.35$.

At $z \gtrsim 6$ the far-UV background (photon energy $> 13.6\,\mathrm{eV}$) is responsible for the re-ionization of the neutral hydrogen in the Universe, but the nature of ionizing sources has not been conclusively identified. One possibility is that ultra-faint galaxies existing in large numbers can provide the required ionizing photons (Finkelstein et al., 2015a; Robertson et al., 2015). In this case, the galaxy UV luminosity function must be steep at the faint end.

[3] The contribution of active galactic nuclei is small in comparison, see Supplementary Materials.

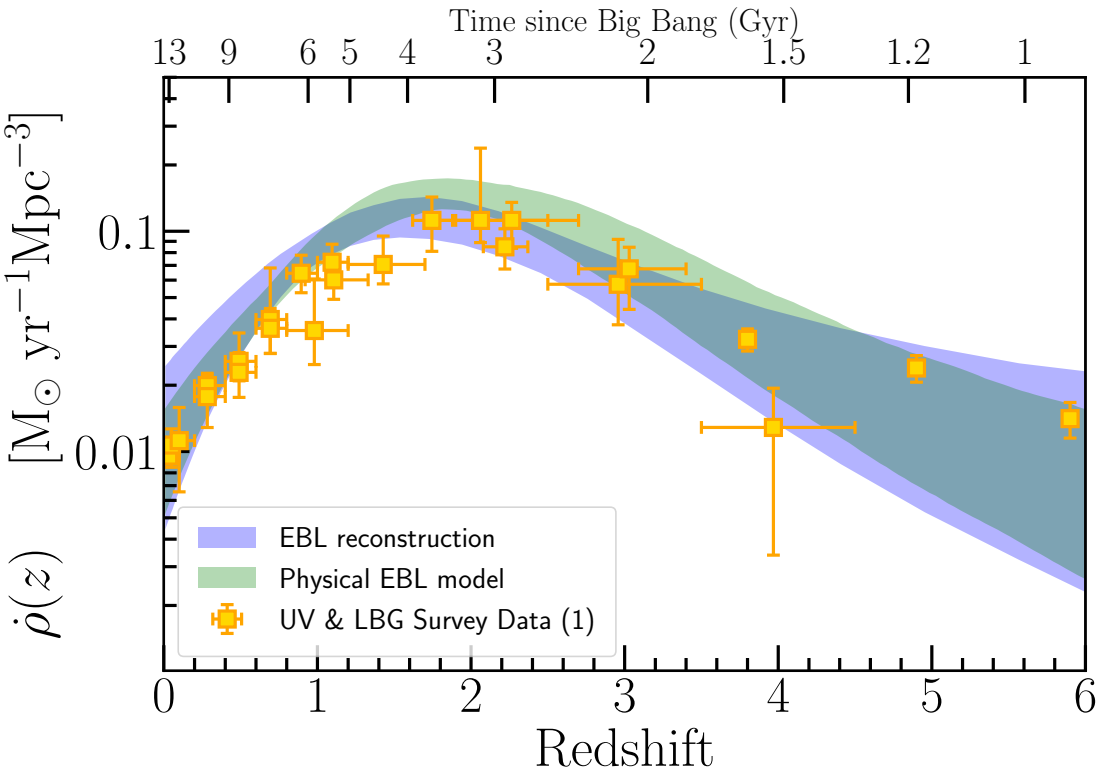

Figure 5.3 The cosmic star-formation history as constrained from the optical depth data. The shaded regions correspond to the 1σ confidence regions on the star formation rate density as a function of redshift, $\dot{\rho}(z)$, obtained from two independent methods, based on 1) a physical EBL model (green) and 2) an empirical EBL reconstruction (blue, see Supplementary Materials). The data points show the SFH derived from UV surveys at low z and deep Lyman Break Galaxy (LBG) surveys at high-z (see review of Madau & Dickinson (2014) and references therein). Figure 5.15 in Supplementary Materials includes a more complete set of data from different tracers of the star-formation rate.

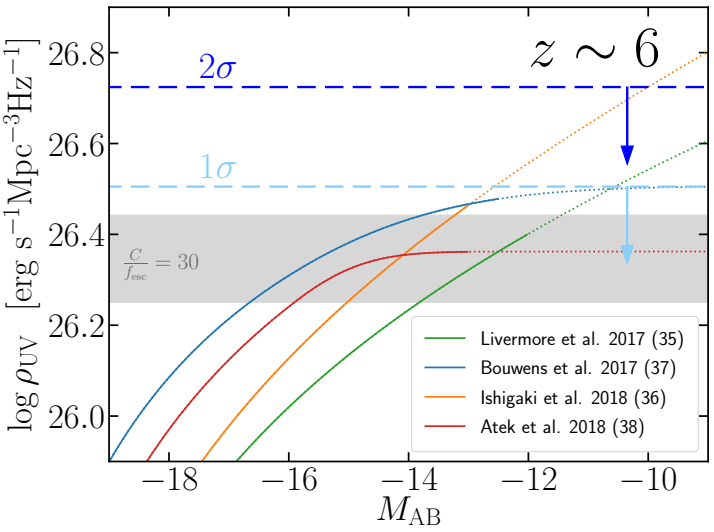

Figure 5.4 Upper limits on the UV luminosity density of galaxies at $z \sim 6$. The $1\,\sigma$ and $2\,\sigma$ limits are shown as dashed horizontal lines, light blue and dark blue respectively. The solid curves show the $z \sim 6$ UV emissivity from Livermore et al. (2017); Bouwens et al. (2017); Ishigaki et al. (2018); Atek et al. (2018) of the Hubble Frontier Fields (HFF) program as a function of the lower integration limit of the UV luminosity function. The dotted lines correspond to extrapolations beyond the limiting magnitude of the HFF analyses. The data from Bouwens et al. (2017) correspond to their "GLAFIC" case. The lines of Ishigaki et al. (2018) and Atek et al. (2018) have been shifted up by 0.15 dex to account for evolution of their combined $z \sim 6-7$ sample to $z \sim 6$. The grey area corresponds to the luminosity required to keep the Universe ionized at $z = 6$ assuming $C/f_{\rm esc} = 30$, where C is the clumping factor of ionized hydrogen and $f_{\rm esc}$ is the mean escape fraction of ionizing photons (see Supplementary Materials).

Recent measurements of the luminosity function in the deepest *Hubble* fields remain inconclusive at the faintest levels (absolute AB magnitude $M_{\rm AB} \gtrsim -15$) with some suggesting a continued steep faint-end slope Livermore et al. (2017); Ishigaki et al. (2018) and others claiming a turnover (Bouwens et al., 2017; Atek et al., 2018). Our upper limits at $z = 5-6$ on the UV emissivity $\rho_{\rm UV} < 3.2(5.3) \times 10^{26}$ erg s^{-1} Mpc^{-3} Hz^{-1} $1\,\sigma$ $(2\,\sigma)$, see Figure 5.4, suggest a turnover of the luminosity function at $M_{\rm AB} \sim -14$ in agreement with Bouwens et al. (2017) and Atek et al. (2018). This still allows for abundant photons to drive the re-ionization.

Acknowledgments

Funding

M. Ajello, V. Paliya., and A. Desai acknowledge support of NSF and NASA through grants AST-1715256, NNX16AR72G, and 80NSSC17K0506. K. Helgason. acknowledges support from the Icelandic Research Fund, grant number 173728-051. J. Finke. was supported by the Chief of Naval Research and by a grant of computer time from the Department of Defense High Performance Computing Modernization Program at the Naval Research Laboratory. A. Domínguez. thanks the support of the Juan de la Cierva program from the Spanish MEC.

Fermi-**LAT collaboration:** The *Fermi* LAT Collaboration acknowledges generous ongoing support from a number of agencies and institutes that have supported both the development and the operation of the LAT as well as scientific data analysis. These include the National Aeronautics and Space Administration and the Department of Energy in the United States, the Commissariat à l'Energie Atomique and the Centre National de la Recherche Scientifique / Institut National de Physique Nucléaire et de Physique des Particules in France, the Agenzia Spaziale Italiana and the Istituto Nazionale di Fisica Nucleare in Italy, the Ministry of Education, Culture, Sports, Science and Technology (MEXT), High Energy Accelerator Research Organization (KEK) and Japan Aerospace Exploration Agency (JAXA) in Japan, and the K. A. Wallenberg Foundation, the Swedish Research Council and the Swedish National Space Board in Sweden. Additional support for science analysis during the operations phase is gratefully acknowledged from the Istituto Nazionale di Astrofisica in Italy and the Centre National d'Études Spatiales in France. This work performed in part under DOE Contract DE-AC02-76SF00515.

Author contribution:

All authors meet the journal authorship criteria. M. Ajello designed the project and wrote most of the paper. V. Paliya performed the analysis of the γ-ray data, while

K. Helgason derived the constrains on the EBL and the star-formation history and wrote all the corresponding text. J. Finke derived the results of the stellar population method and wrote the corresponding text. A. Desai tested all the EBL models while A. Domínguez provided all the EBL-related data reported in the figures and wrote the corresponding text. All co-authors have read, provided comments and approved the manuscript.

Competing interests:

All co-authors declare that there are no competing interesting.

Data and materials availability:

The data used to derive the results presented in this paper are provided in tabular form in the supplementary materials. The *Fermi*-LAT data and software needed to analyze those are available from the *Fermi* Science Support Center `http://fermi.gsfc.nasa.gov/ssc`. The reconstructed optical depth templates, EBL, and SFH are also available at `http://www.hi.is/~helgason/ebl_fermi.html`. The tool to produce physical models of blazars' SEDs is available at `www.isdc.unige.ch/sedtool`.

5.2 Supplementary Materials

`www.sciencemag.org`

5.2.1 Sample Selection and Data Analysis

Our sample is selected starting from the objects reported in the third catalog of active galactic nuclei detected by the LAT, 3LAC, (Ackermann et al., 2015). We exclude all the blazars reported there with a double association and those lacking a redshift measurement. Most redshift measurements for BL Lacs reported in 3LAC come from Shaw et al. (2013). For each source we assess the significance of the detection (between 1 GeV and 1 TeV) defining a

test statistics (TS) as $TS = 2\Delta \log \mathscr{L}$, where $\mathscr{L}$ represents the likelihood function between models with and without the source of interest. We use this to exclude all sources that have a $TS < 25$ in this analysis. Our final sample comprises 434 FSRQs and 325 BL Lacs distributed (see Figure 5.5) between a redshift of 0.03 and 3.1.

The analysis relies on 101 months (Aug. 2008 to Jan. 2017) of Pass 8 (P8) class 'SOURCE' photons detected by the LAT between 1 GeV and 1 TeV. This dataset was filtered to eliminate times when the spacecraft was over the South Atlantic Anomaly and to remove photons detected at angles larger than 100° from the zenith. For the analysis of each source we use photons within 15° of the source position (region of interest, ROI). For each ROI we define a sky model that comprises the diffuse Galactic (Acero et al., 2016) and extragalactic emission [4] as well as the emission from background sources in the ROI. The latter includes sources detected in the third *Fermi*-LAT catalog, 3FGL, 3FGL as well as any new source that is detected because of the additional exposure (with respect to the 3FGL) used here. These sources are found generating a TS map and identified as excesses above a $TS = 25$ threshold and added to the sky model with a power-law spectrum. The LAT 'P8R2_SOURCE_V6' instrumental response function (IRF) and a binned likelihood method are used to fit the sky model to the data.

5.2.2 Intrinsic Spectra of Blazars

To capture the intrinsic curvature in the spectra of blazars we adopt the following strategy that has been optimized using simulations prior to the data analysis (see below). The data are fitted only to a maximum energy up to which the attenuation of the EBL is negligible. This is defined as the energy at which the optical depth $\tau_{\gamma\gamma}$<0.1 for the model of Finke et al. (2010). However, we tested that our analysis is robust against changes of EBL model used to define this maximum energy and changes to the threshold (from e.g. $\tau_{\gamma\gamma}$< 0.1 to $\tau_{\gamma\gamma}$< 0.05). The optical depth decreases sharply in this regime where not many EBL photons are expected due to a characteristic drop-off at the Lyman-limit (13.6 eV). Our

[4]The templates used are gll_iem_v06.fits and iso_P8R2_SOURCE_V6_v06.txt, see https://fermi.gsfc.nasa.gov/ssc/data/access/lat/BackgroundModels.html.

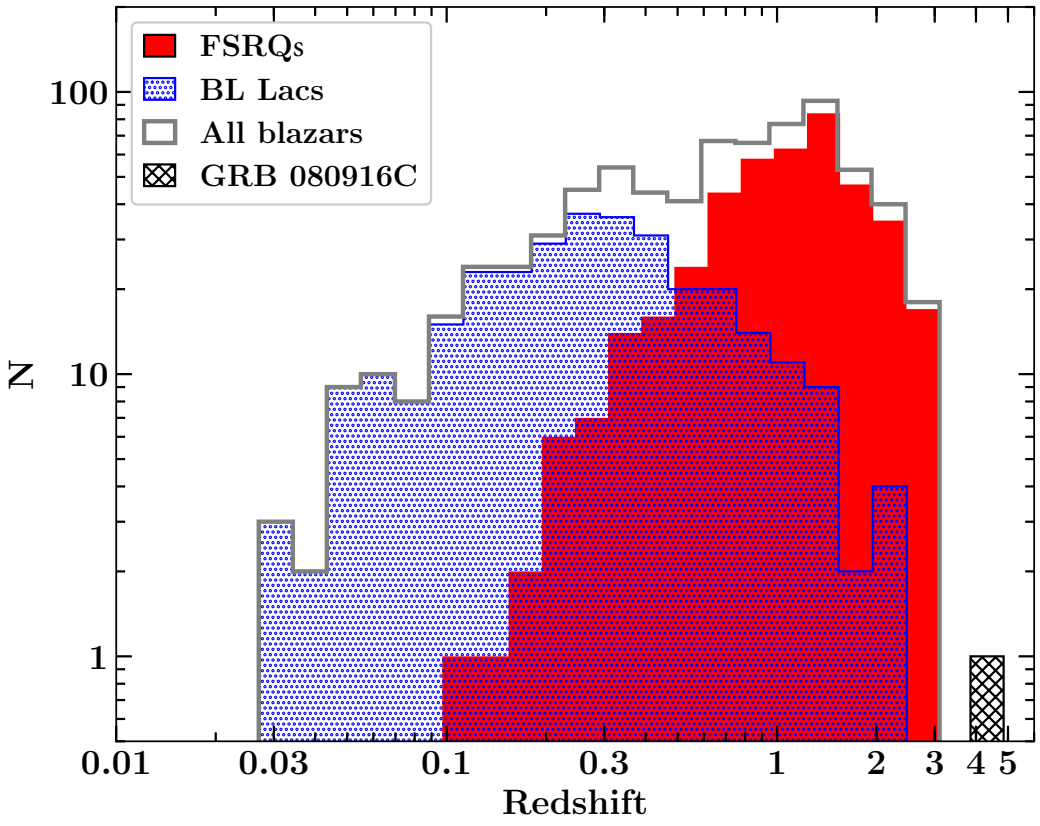

Figure 5.5 Redshift distribution of the sources used in this analysis on a logarithmic scale.

baseline model for the intrinsic blazar spectrum is a log-parabola:

$$\frac{\mathrm{d}N}{\mathrm{d}E} = N_0 \left(\frac{E}{E_b}\right)^{-\alpha+\beta\log(E/E_b)} \tag{5.2}$$

where N_0 (the normalization), α (photon index), β (curvature) are all free parameters and E_b is a scaling energy. We also test whether an exponential power law could be a better representation of the blazar spectrumand this is defined as:

$$\frac{\mathrm{d}N}{\mathrm{d}E} = N_0 \left(\frac{E}{E_c}\right)^{\alpha} e^{-(E/E_b)^{\gamma_1}} \tag{5.3}$$

where E_c (cut off energy) and γ_1 (the exponential index) are all free parameters. Smoothed broken power laws and broken power laws were also tested, but they were never found to

Table 5.1. Criteria, optimized on simulations, adopted to choose a spectral model.

$TS_{c,1}$	$TS_{c,2}$	Model Chosen
< 1	< 3	Log-parabola
> 1	< 3	Power law with exponential cut-off with γ_1=0.5
	> 3	Power law with exponential cut-off with γ_1 free

describe the blazar intrinsic spectrum better than the two models reported above in the energy range used in this work.

When testing the exponential cut-off model we perform a first fit with γ_1 fixed at 0.5 (justified from the observations of hundreds of FSRQs, see Ajello et al., 2012b)) and then another fit leaving γ_1 free to vary. We define two TS of curvature $TS_{c,1}$ and $TS_{c,2}$ as follows:

$$TS_{c,1} = 2(\log L_{exp,\gamma_1=0.5} - \log L_{\log-parabola}) \quad (5.4)$$

$$TS_{c,2} = 2(\log L_{exp,\gamma_1=free} - \log L_{\log-parabola}). \quad (5.5)$$

where $\log L_{exp,\gamma_1=0.5}$ and $\log L_{exp,\gamma_1=free}$ are the log-likehoods derived using the exponential cut-off model with $\gamma_1 = 0.5$ and γ_1 free to vary respectively and $\log L_{\log-parabola}$ is the log-likelihood of the log-parabola model.

We adopt the criteria reported in Table 5.1 to choose the model used to describe each blazar's intrinsic spectrum. In order to avoid convergence problems, in the analysis presented above, the exponential index γ_1 remains fixed at either 0.5 or the best-fitting value found at this step. The median of the distribution of fitted γ_1 values is $\approx$0.5.

5.2.3 Analysis

5.2.4 Results for Blazars

Once the choice of the intrinsic spectrum for the sources has been made, the analysis reverts to using the full, 1 GeV–1 TeV, energy band and the modeled spectra of all sources

include the EBL attenuation as reported in Equation 5.1, where b is a parameter, common to all sources, that is varied to fit the EBL model prediction to the data. A $b = 1$ would mean that the EBL model predictions are in agreement with the LAT data, while a $b = 0$ would imply that there is no evidence for attenuation due to absorption by EBL photons in the spectra of blazars.

Because of the complexity of the problem, the b parameter is not optimized in one stage. Instead, for each source we scan the likelihood function in very small steps of b creating a profile likelihood. In this process, the parameters of the diffuse emission, those of the brightest sources, and those of the source of interest (except γ_1) are all left free to vary. For each source, the best-fitting b value is the one that maximizes the log-likelihood. A TS of the detection of the EBL can be built comparing the log-likelihood values at the best-fitting $b = b_0$ and at $b = 0$ as $\mathrm{TS_{EBL}} = 2[\log L(b_0) - \log L(b = 0)]$. Because log-likelihoods (and thus TS) are additive, we can determine the b value that maximizes the global (for all sources) likelihood and produces the largest TS_{EBL}. In Figure 5.6, we plot the TS profile, as a function of b, for all sources (and separately for BL Lacs and FSRQs) for the model of Finke et al. (2010). A b=1.03 improves the fit by a TS of $\sim$300, which corresponds to $\sim 17\,\sigma$ for one degree of freedom. We note that the spectral evolution of the blazar class with redshift has a negligible effect on this analysis, as apparent from Figure 5.6, which shows that the level of EBL measured using (mostly) hard-spectrum BL Lacs is in very good agreement with that found using soft-spectrum FSRQs. As an additional test we report the values of the b parameter for the model of Finke et al. (2010) for BL Lacs with a synchrotron peak frequency $> 10^{16}\,Hz$ (called HSPs) and for the remaining BL Lacs; these are respectively $b_{HSPs} = 0.98^{+0.09}_{-0.13}$ (TS_{EBL}=125.8) and $b_{rest} = 0.86^{+0.16}_{-0.10}$ ($TS_{\mathrm{EBL}} = 45.1$). These highlight once more that there is no bias in the level of the EBL due to the spectral evolution of the blazar class.

One can also measure the compatibility of a model prediction with the *Fermi*-LAT data defining a TS as $TS_{b=1} = 2[\log L(b_0) - \log L(b = 1)]$. By definition a large $TS_{b=1}$ implies that the model predictions are in tension with the *Fermi*-LAT data; this typically

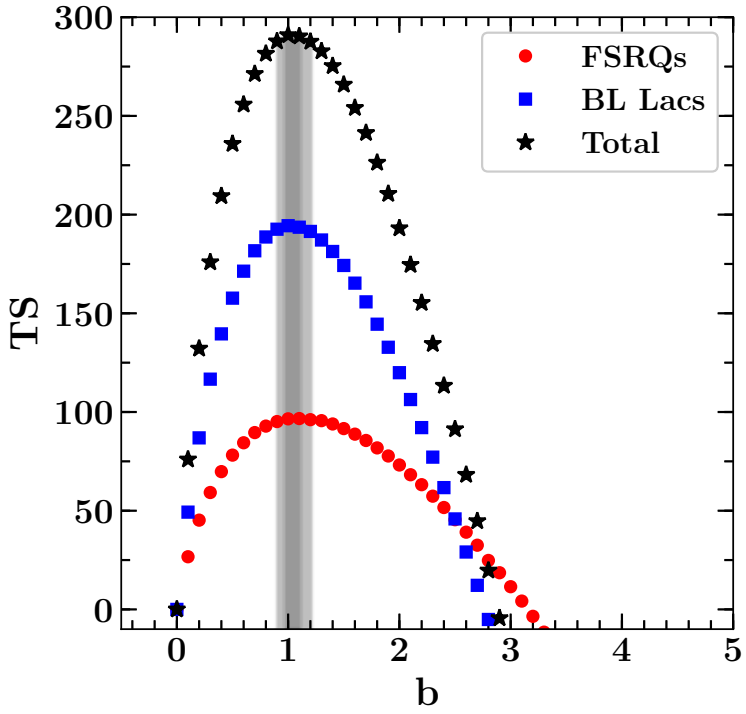

Figure 5.6 Detection of the attenuation of the EBL. Test statistics of the EBL as a function of the scaling parameter b adopting the model of Finke et al. (2010). The shaded regions show the $1\,\sigma$ and $2\,\sigma$ confidence intervals around the best fitting value of b. This TS profile was obtained by summing the TS profiles of every source, including variable sources.

happens when the model predicts a larger-than-observed attenuation. Table 5.2 shows the results of our analysis for some of the models available in the literature that have not been found in tension with previous γ-ray data. The table shows that the high model of Scully et al. (2014) and the best-fitting model of Kneiske et al. (2004) are excluded. Moreover, the models of Gilmore et al. (2012) and Domínguez et al. (2011) are found in tension at the $\sim 3\,\sigma$ level with the *Fermi*-LAT observations. All these models predict a larger optical-UV intensity of the EBL than the models compatible with the LAT data.

The optical depth as a function of energy and redshift can be measured by repeating the above procedure (i.e., renormalizing the optical depth predicted by a model), but in small energy and redshift bins. In this process, the uncertainty due to the small disagreement between different EBL models, about the shape of the optical depth curve within any given

Table 5.2. Joint-likelihood results for different EBL models ordered by decreasing value of the last column.

Model	Ref.	Significance of b=0 Rejection[a]	b[b]	Significance of b=1 Rejection[c]
Scully et al. (2014) – high	Scully et al. (2014)	16.0	0.42±0.03	17.4
Kneiske et al. (2004) – best -fit	Kneiske et al. (2004)	16.9	0.68±0.05	6.0
Gilmore et al. (2012) – fixed	Gilmore et al. (2012)	16.7	1.30±0.10	3.0
Gilmore et al. (2012) – fiducial	Gilmore et al. (2012)	16.6	0.81±0.06	2.9
Dominguez et al. (2011)	Domínguez et al. (2011)	16.6	1.31±0.10	2.9
Franceschini et al. (2017)	Franceschini & Rodighiero (2017)	16.4	1.25±0.10	2.5
Gilmore et al. (2009)	Gilmore et al. (2009)	16.7	1.03±0.08	2.4
Inoue et al. (2013)	Inoue et al. (2013)	16.2	0.87±0.06	2.1
Kneiske & Dole (2010)	Kneiske & Dole (2010)	16.8	0.94±0.08	1.7
Helgason et al. (2012)	Helgason & Kashlinsky (2012b)	16.5	1.10±0.08	1.3
Finke et al. (2010) – model C	Finke et al. (2010)	17.1	1.03±0.08	0.4
Scully et al. (2014) – low	Scully et al. (2014)	16.0	1.00±0.07	0.1

[a]Significance, in units of σ, of the attenuation in the spectra of blazars when a given EBL model is scaled by the factor b. In this case b=0 (i.e., no EBL absorption) constitutes the null hypothesis.

[b]This column lists the maximum likelihood values and $1\,\sigma$ confidence ranges for the opacity scaling factor.

[c]Here the b=1 case (i.e., EBL absorption as predicted by a given EBL model) constitutes the null hypothesis. This column shows the compatibility (expressed in units of σ) of the predictions of EBL models with the *Fermi*-LAT observations. Large values mean less likely to be compatible.

bin, has been included in the final uncertainty of the optical depth. The final uncertainty includes also the 10 % systematic uncertainty discussed below. The redshift bins were chosen so that similar values of TS_{EBL} were obtained in all the bins. Figure 5.7 shows measurements of the optical depth $\tau_{\gamma\gamma}$ due to EBL absorption in different redshift and energy bins. It is apparent from the figure that most of the constraining power is around $\tau_{\gamma\gamma} \approx 1$. Formally the $\tau_{\gamma\gamma}(E, z) = 1$ value marks the cosmic γ-ray horizon, i.e., the energy above which our Universe becomes opaque to γ rays for a given redshift (Fazio & Stecker, 1970; Domínguez et al., 2013). The energy at which $\tau_{\gamma\gamma}(E, z) = 1$ at any redshift can be found by renormalizing any EBL model to fit the data presented in Figure 5.7 and propagating the (statistical plus systematic) uncertainties. Figure 5.1 shows that *Fermi* LAT maps the horizon position with energy from low ($z \approx 0.03$) to high ($z \approx 3.1$) redshift. Figure 5.1 also shows the highest-energy photons detected from the blazars in our sample.

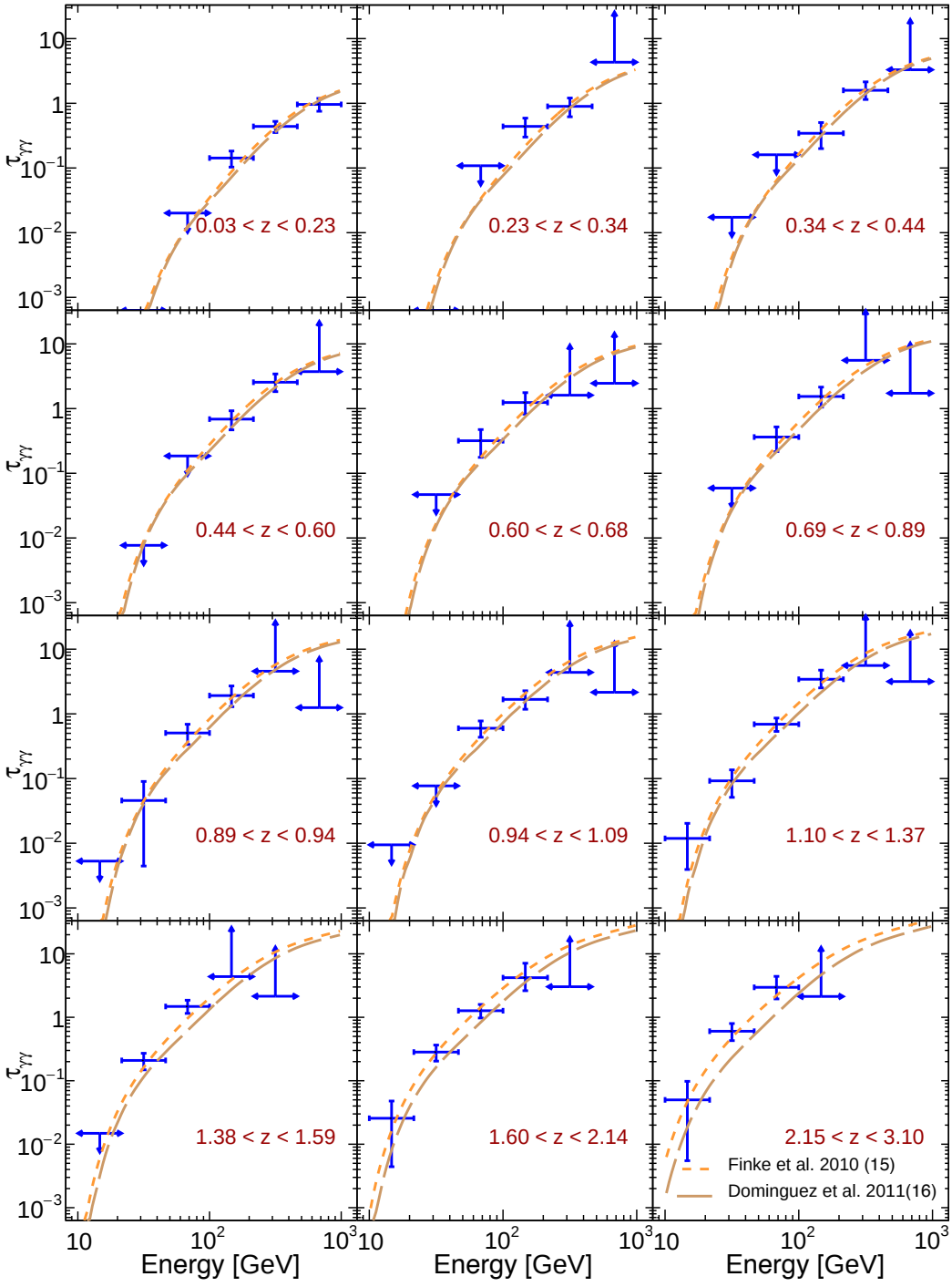

Figure 5.7 Measurements of the optical depth $\tau_{\gamma\gamma}$ due to the EBL in different redshift and energy bins. The lines show the predictions of two EBL models (Finke et al., 2010; Domínguez et al., 2011).

5.2.5 GRB 080916C

In order to constrain the EBL and SFH to the highest possible redshifts, we complement the blazar sample with a single gamma-ray burst (GRB), GRB 080916C, detected by *Fermi* LAT at z=4.35 (Abdo et al., 2009b; Greiner et al., 2009b). This was an extremely luminous event, whose hard spectrum has already produced constraints on the SFH at high redshift (Gilmore, 2012; Inoue et al., 2014). With respect to previous works, the release of the Pass 8 event-level analysis has allowed us to recover more high-energy photons, particularly one at 27.4 GeV, ≈146 GeV in the source frame, from GRB 080916C (Atwood et al., 2013).

The analysis is similar to the one reported by Desai et al. (2017). Transient-class photons between 0.1 GeV and 100 GeV were downloaded around a 10° position from the burst and from the time of the GRB until 1775.9 s later. Photons detected at a zenith angle greater than 105° were removed. The ROI model consists of the burst, the Galactic and isotropic templates[5]. We rely on the 'P8R2_TRANSIENT020' IRF.

The source intrinsic spectrum is represented (and fitted up to 10 GeV) by a single power law (with a photon index of 2.25±0.06) employing a time-averaged analysis. No curvature is observed in the *Fermi*-LAT spectrum. A time-resolved analysis does not yield any difference for this work (Desai et al., 2017). We produce a 95 % upper limit on the optical depth by adopting the same method as described above for blazars. This upper limit is $\tau_{\gamma\gamma} < 0.46$ at an energy of ≈17 GeV and z=4.35 and it does not depend on the EBL model used to derive it. This upper limit is a factor of two lower than that used by Inoue et al. (2014). This is due to the additional photons detected at >10 GeV and particularly to the 27.4 GeV photon. The probability that this photon belongs to the background, rather than to GRB 080916C, is only 5×10^{-5}. A so-called 'maximally conservative upper limit' based on the assumption that the intrinsic spectrum cannot be harder than a power law with an index $\Gamma = 1.5$ is even more constraining; however, it is not adopted here. The spectrum of GRB 080916C used here is shown in Figure 5.8.

[5]We used the following templates: gll_iem_v06.fits and iso_P8R2_TRANSIENT020_V6_v06.txt.

Table 5.3. EBL Optical Depths $\tau_{\gamma\gamma}$ in bins of redshift and energy as reported in Figure 5.7.

$\bar{z}$	z_{min}	z_{max}	[10.0-21.4] (GeV)	[21.4-46.4] (GeV)	[46.4-100.0] (GeV)	[100.0-215.4] (GeV)	[215.4-464.1] (GeV)	[464.1-1000] (GeV)
0.14	0.03	0.23	$\cdots$	$\cdots$	< 0.02	$0.14^{+0.04}_{-0.04}$	$0.44^{+0.09}_{-0.09}$	$0.96^{+0.23}_{-0.21}$
0.27	0.23	0.34	$\cdots$	$\cdots$	< 0.11	$0.44^{+0.15}_{-0.14}$	$0.90^{+0.31}_{-0.28}$	> 4.32
0.39	0.34	0.44	$\cdots$	< 0.02	< 0.16	$0.34^{+0.16}_{-0.14}$	$1.59^{+0.56}_{-0.44}$	> 3.30
0.52	0.44	0.60	$\cdots$	< 0.01	< 0.19	$0.69^{+0.24}_{-0.22}$	$2.55^{+0.88}_{-0.73}$	> 3.72
0.65	0.60	0.68	$\cdots$	< 0.05	$0.32^{+0.16}_{-0.14}$	$1.24^{+0.52}_{-0.42}$	> 1.61	> 2.46
0.79	0.69	0.89	$\cdots$	< 0.06	$0.36^{+0.16}_{-0.15}$	$1.54^{+0.61}_{-0.49}$	> 5.57	> 1.73
0.92	0.89	0.94	< 0.01	$0.05^{+0.04}_{-0.04}$	$0.51^{+0.18}_{-0.17}$	$1.92^{+0.78}_{-0.63}$	> 4.56	> 1.25
1.01	0.94	1.09	< 0.01	< 0.08	$0.60^{+0.18}_{-0.16}$	$1.67^{+0.60}_{-0.50}$	> 4.38	> 2.16
1.24	1.10	1.37	$0.01^{+0.01}_{-0.01}$	$0.09^{+0.04}_{-0.04}$	$0.69^{+0.17}_{-0.16}$	$3.43^{+1.32}_{-0.91}$	> 5.59	> 3.16
1.47	1.38	1.59	< 0.01	$0.21^{+0.06}_{-0.06}$	$1.48^{+0.38}_{-0.33}$	> 4.38	> 2.15	$\cdots$
1.82	1.60	2.14	$0.03^{+0.02}_{-0.02}$	$0.28^{+0.08}_{-0.08}$	$1.27^{+0.32}_{-0.30}$	$4.21^{+2.90}_{-1.59}$	> 3.03	$\cdots$
2.40	2.15	3.10	$0.05^{+0.05}_{-0.04}$	$0.60^{+0.19}_{-0.17}$	$2.97^{+1.45}_{-1.02}$	> 2.13	$\cdots$	$\cdots$

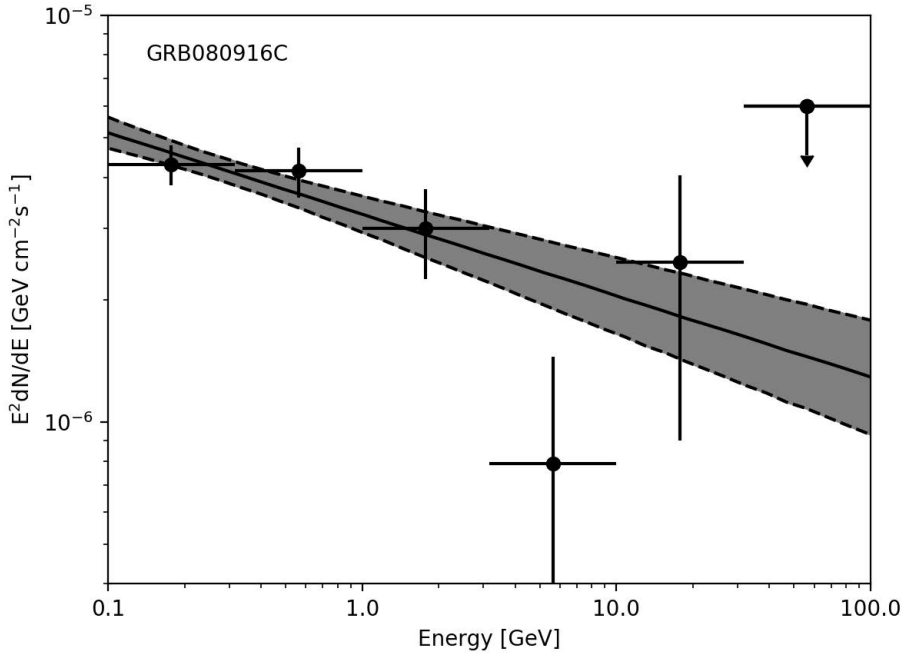

Figure 5.8 Spectrum of GRB 080916C between 0.1 GeV and 100 GeV.

5.2.6 Tests and Simulations

5.2.7 Simulations of Blazar SEDs

The analysis chain described in the previous section has first been tested and optimized on Monte Carlo simulation of synthetic spectral-energy distributions (SEDs) of blazars with properties matching those of blazars observed by *Fermi* LAT.

The SEDs are generated from physical models of blazars' emission that include synchrotron and synchrotron self-Compton as well as (for FSRQs) external Compton scattering and were generated with the numerical code presented in Tramacere et al. (2009) and Tramacere et al. (2011). These SEDs reproduce the range of peak frequencies very well (for both the synchrotron and γ-ray components), including peak curvatures and γ-ray photon indices observed in both *Fermi*-LAT BL Lacs and FSRQs. They include all known effects that contribute to determining the curvature of the intrinsic γ-ray spectrum of *Fermi* blazars. The

crucial transition from the Thomson to the Klein-Nishina cross section as well as (mostly important for FSRQs) absorption within the broad line region (for different distances of the emission region from the broad line region) are all taken into account and contribute to determine the shape of the blazars' spectra at high energy.

These SEDs, attenuated by the EBL for a range of redshifts similar to those of Figure 5.5, are then used to simulate LAT observations of these synthetic sources and have been used to optimize the analysis set-up presented above. In particular, the values of the minimum energy (E_{min}=1 GeV) and those of $TS_{c,1}$ and $TS_{c,2}$ have been derived from the analysis of simulations. Figure 5.9 shows that the analysis chain employed in this work can effectively recover the simulated level of EBL.

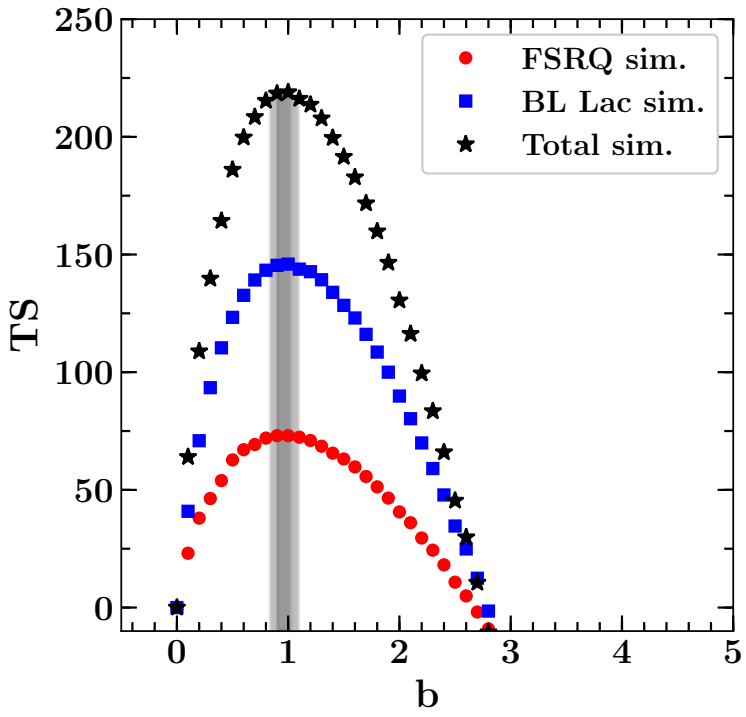

Figure 5.9 Detection of the EBL attenuation in Monte Carlo simulations. Test statistics of the EBL as a function of the scaling parameter b adopting the model of Finke et al. (2010) for our set of Monte Carlo simulations. The shaded regions show the $1\,\sigma$ and $2\,\sigma$ confidence intervals around the best fit.

5.2.8 Variability

Blazars are inherently variable objects (at all wavelengths) and variability may bias or complicate the measurement of the EBL attenuation. In order to cope with blazars' variability as well as possible, a time-resolved analysis is performed for all sources that are found variable at $> 10\,\mathrm{GeV}$ in the recent third catalog of hard sources, 3FHL, (Ajello et al., 2017). We rely on the time bins derived by the Bayesian block analysis presented in 3FHL as these are times when the sources were found to alter their state at $> 10\,\mathrm{GeV}$, which is the relevant energy range for detecting the EBL attenuation. In each time bin, the criteria reported in Table 5.1 are used to determine the best intrinsic spectral model. Because for a given source time-resolved spectra can be treated as independent observations, their contribution to the TS_{EBL} has been summed to the one of the remainder of the sample. Figure 5.6 includes the contribution from variable and non-variable sources. The level of EBL as determined from the variable sources alone is found to be in good agreement with the rest of the sample. Figure 5.10 shows the TS_{EBL} as a function of the b parameter (for the model of Finke et al. (2010)) for 4 variable BL Lacs and FSRQs and how that compares to the result of a time-averaged analysis. In general, we find a time-averaged analysis works well for objects which vary primarily in flux, while a time-resolved analysis is required for all those objects experiencing also spectral variability (see right versus left plots in Figure 5.10). Finally, we used the Fermi All-sky Variability Analysis tool (Ackermann et al., 2013a; Abdollahi et al., 2017) to search for significant residual spectral variability within Bayesian blocks, but none could be found.

5.2.9 Systematic Uncertainties

In order to gauge the systematic uncertainties of this analysis we have performed the tests reported below:

- Instead of using a variable maximum energy up to which to fit the intrinsic spectrum (chosen to be the energy corresponding to $\tau_{\gamma\gamma} < 0.1$ for the model of Finke et al.

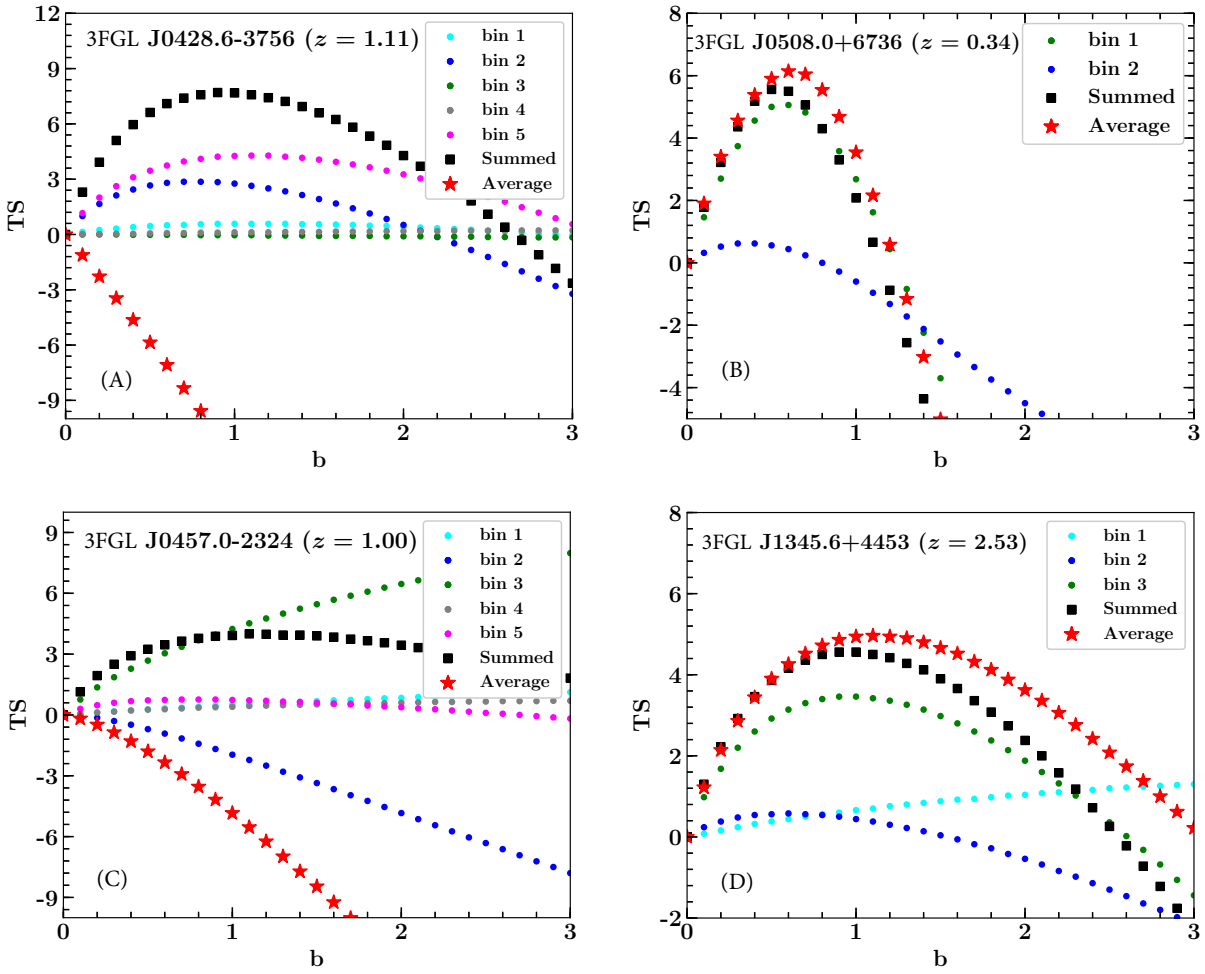

Figure 5.10 Impact of time-resolved analysis. Contribution to the TS_{EBL} as a function of scaling parameter b, adopting the model of Finke et al. (2010), for the time resolved (Summed) and time averaged (Average) analysis for two BL Lacs (top) and two FSRQs (bottom).

(2010)), we use a constant maximum energy of 10 GeV for all sources. Repeating the entire analysis we find $b = 1.09 \pm 0.08$ in agreement with the results presented in the main text.

- A similar result as above has been obtained using a maximum energy, to measure the intrinsic spectrum, defined as that obtained when $\tau_{\gamma\gamma} < 0.05$ ($b = 1.07 \pm 0.08$ for the model of Finke et al. (2010)).

- We use the IRF bracketing method as described in Fermi-LAT Collaboration (2012). By deriving two different sets of IRFs and repeating the entire analysis we find that the systematic uncertainty in the optical depth $\tau_{\gamma\gamma}$ is of the order $\sim$7 %.

The results presented in the above sections are fully confirmed and the systematic uncertainty on the optical depth $\tau_{\gamma\gamma}$ due to changing the energy threshold to characterize the intrinsic spectrum and IRF are, together, $\lesssim$10 %. A systematic uncertainty of $0.1 \times \tau_{\gamma\gamma}$ (added in quadrature) has been included in the uncertainties reported in Figures 5.1 and 5.7 and propagated to all results that use those data.

5.2.10 Reconstructing the evolving EBL

The optical depth for a γ ray of observed energy E_γ originating in a source at redshift z_s is related to the evolving number density of EBL photons, $n_{\rm EBL}(\epsilon, z)$, (Gould & Schréder, 1967b; Stecker, 1971; Brown et al., 1973):

$$\tau_{\gamma\gamma}(E_\gamma, z_s) = c \int_0^{z_s} \left|\frac{dt}{dz}\right| dz \int_{-1}^{1} (1-\mu)\frac{d\mu}{2} \int_{2m_e^2c^4/\epsilon_\gamma(1-\mu)}^{\infty} \sigma(\epsilon_{\rm EBL}, \epsilon_\gamma, \mu) n_{\rm EBL}(\epsilon, z) d\epsilon_{\rm EBL} \quad (5.6)$$

where the rest-frame energy of γ rays and EBL photons are denoted by $\epsilon_\gamma = E_\gamma(1+z_s)$ and $\epsilon_{\rm EBL} = E_{\rm EBL}(1+z_s)$ respectively, $\mu = \cos\theta$ denotes the angle of incidence between the two photons, and $|dt/dz|^{-1} = H_0(1+z)\sqrt{\Omega_M(1+z)^3+\Omega_\Lambda}$, where the Hubble and the cosmological parameters are $H_0 = 70\,{\rm km\ s^{-1}\ Mpc^{-1}}$, Ω_M=0.3, and Ω_λ =0.7. The cross section for the photon-photon interaction appearing in the last integral in Equation 5.6 is

$$\sigma(\epsilon_{\rm EBL}, \epsilon_\gamma, \mu) = \frac{3\sigma_T}{16}(1-\beta^2)\left[2\beta(\beta^2-2) + (3-\beta^4)\ln\left(\frac{1+\beta}{1-\beta}\right)\right], \quad (5.7)$$

with

$$\beta = \sqrt{1 - \frac{2m_e^2c^4}{\epsilon_{\rm EBL}\epsilon_\gamma(1-\mu)}}.$$

where $m_e c^2$ is the electron rest mass. In other words, for a given cosmology, the SED and evolution of the EBL uniquely specify the optical depth at all redshifts. Conversely, we

can use the measured optical depths $\tau_{\gamma\gamma}(E_\gamma, z)$ to reconstruct $n_{\rm EBL}(\epsilon, z)$.

The physical properties of galaxies, such as star-formation rate, stellar mass and metallicity, are encoded in their SED. Rather than the EBL, which is accumulated over cosmic time, it is more informative to study the instantaneous SED of the galaxy population as a whole i.e., the cosmic emissivity. The buildup of the EBL is related to the volume emissivity $j(\epsilon, z)$ (or equivalently, luminosity density) via:

$$n_{\rm EBL}(\epsilon, z) = (1+z)^3 \int_z^\infty \frac{j(\epsilon, z)}{\epsilon} \left| \frac{dt}{dz'} \right| dz'. \tag{5.8}$$

The EBL spectral intensity (see Figure 6.3) can be found from the number density by $\epsilon I(\epsilon, z) = \frac{c}{4\pi} \epsilon^2 n_{\rm EBL}(\epsilon, z)$.

5.2.11 Model for the Cosmic Emissivity

Our task is to reconstruct $j(\epsilon, z)$ based on the measured optical depths reported in Figure 5.7 without making assumptions on galaxy properties or their stellar population. We represent j_λ as the sum of several log-normal templates with a fixed peak position:

$$j(\lambda) = \sum_i a_i \cdot \exp\left[-\frac{(\log\lambda - \log\lambda_i)^2}{2\sigma^2} \right] \quad [\mathrm{erg \cdot s^{-1} cm^{-3-1}}] \tag{5.9}$$

where we fix $\sigma = 0.2$, $\lambda_i = [0.17, 0.92, 2.2, 8.0]\,\mu$m and the amplitudes a_i are left free to vary. We find that four log-normal templates allow for a sufficiently flexible spectral shape from UV to the mid-IR. A Lyman-break is imposed by cutting off the spectrum at $\epsilon > 13.6\,$eV where neutral hydrogen becomes opaque. We have chosen the fixed locations (λ_i) and width (σ) of the templates such that common features in galaxy SEDs, a flat far-UV continuum and a 4000Å/Balmer break, are easily captured. Each template is allowed to evolve independently with redshift based on a function similar to the SFH parametrization of Madau & Dickinson

(2014) leading to the full expression

$$j(\lambda_i, z) = \sum_i a_i \cdot \exp\left[-\frac{(\log\lambda - \log\lambda_i)^2}{2\sigma^2}\right] \times \frac{(1+z)^{b_i}}{1+\left(\frac{1+z}{c_i}\right)^{d_i}}. \tag{5.10}$$

At each of the fixed wavelengths λ_i, one parameter controls the amplitude, a_i, and three control the evolution, b_i, c_i and d_i, yielding a total of $4 \times 4 = 16$ free parameters. The number of optical depth data points is 64.

To explore the sensitivity to different functional forms for the evolution, we also test the parametrization from Cole et al. (2001):

$$j(\lambda_i, z) \propto \frac{a_i + b_i z}{1 + (z/c_i)^{d_i}} \ , \tag{5.11}$$

with free parameters a_i, b_i, c_i, and d_i which we display alongside our main results for the SFH in Figure 5.15.

5.2.12 Markov Chain Monte Carlo: Setup

We use the MCMC code `emcee` (Foreman-Mackey et al., 2013), a Python implementation of an affine invariant MCMC ensemble sampler (Goodman & Weare, 2010), to constrain the parameters controlling the emissivity. The likelihood function is estimated as $\mathscr{L} \propto \exp(-\chi^2)$ where χ^2 is given by

$$\chi^2 = \sum_{i=1}^{N}\sum_{j=1}^{M} \frac{[\tau_{\rm data}(E_i, z_j) - \tau_{\rm model}(\vec{\theta}|E_i, z_j)]^2}{\sigma_{i,j}^2} \tag{5.12}$$

where there are N energy (E_i) bins, M redshift (z_j) bins, $\tau_{\rm data}(E_i, z_j)$ is the measured absorption optical depth presented in Figure 5.7, $\tau_{\rm model}(\vec{\theta}|E_i, z_j)$ is the model absorption optical depth with parameters $\vec{\theta}$, and $\sigma_{i,j}$ is the (statistical plus systematic) uncertainty on the absorption optical depth measurements.

We choose flat priors on all parameters $\log a_i/(\mathrm{ergs^{-1}Mpc^{-3}Hz^{-1}}) = [22, 32]$, $b_i =$

$[-2, 10]$, $c_i = [1, 7]$, $d_i = [0, 20]$. We restrict the range of the evolution parameter controlling the location of the peak (or curvature) to $c_i = [1, 7]$ since our dataset has limited constraining power for shape changes at redshifts much larger than our sample coverage ($0 < z < 4$). Note however, that this does not force the presence of a peak and a turnover as the function reduces to a power-law $\propto (1 + z)^{b_i}$ when $d \to 0$.

With the emissivity specified as a function of wavelength and redshift, we calculate the resulting EBL and optical depth according to Equations 5.6–5.8 respectively for each proposed step in the MCMC. Each calculation of $\tau_{\gamma\gamma}$ involves integrating over wavelength, redshift and angle of incidence, but we only require $\tau_{\gamma\gamma}$ at six energies, for every redshift, making it computationally manageable. Our final results are based on MCMC chains from 120 walkers exploring the parameter space in 10,000 steps each. This results in 1,140,000 steps after a burn-in of 500 steps for each walker.

5.2.13 Results and Validation

In Figure 5.11 we display the 68% and 95% confidence regions for the total cosmic emissivity in several redshift bins. The *Fermi*-LAT dataset is tightly constraining at UV, optical and, at low-z, also near-IR wavelengths. The confidence regions get broader towards mid-IR wavelengths due to the energy range of *Fermi* LAT being limited to < 1 TeV. Figure 5.11 also shows that the *Fermi*-LAT dataset provides the tightest constraints around $z \simeq 0.15-1.5$ as the opacity increases for larger distances traveled. At $z \gtrsim 2$ we are limited by the number of bright blazars with substantial emission above $\sim$10 GeV in our sample. Comparing our cosmic emissivity with measurements of integrated galaxy luminosity functions shows that our results are in good overall agreement across the wavelength range. This implies that the bulk of the EBL is already accounted for by galaxy surveys.

We have validated this reconstruction method by creating ten sets of fake $\tau(E, z)$ data points in the same energy and redshift bins, and possessing the same fractional uncertainties, as the original dataset. The simulated datasets are generated by drawing random sets of values for the 16 parameters of Equation 6.3, within their assumed priors, and cal-

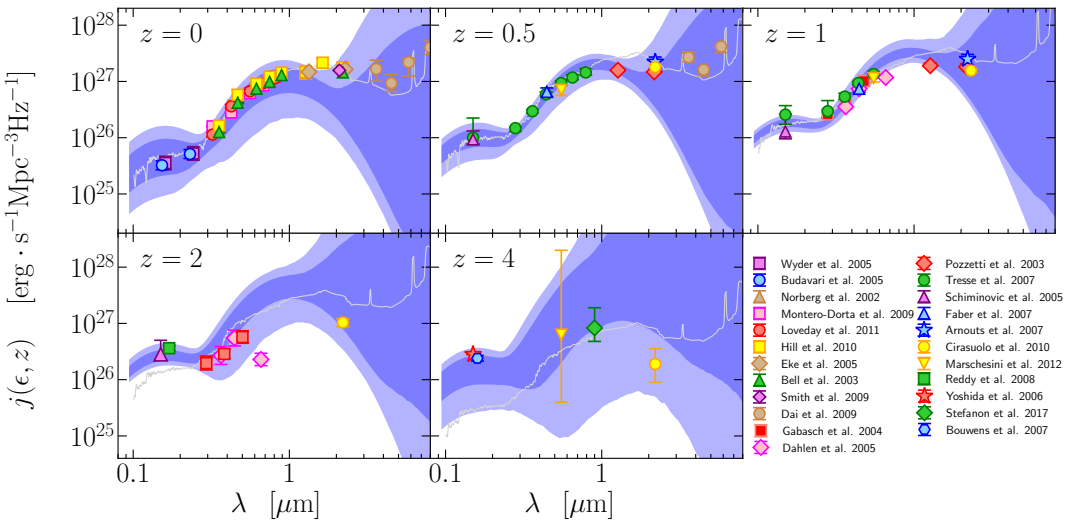

Figure 5.11 The cosmic emissivity (luminosity density) as a function of wavelength in several redshift slices. The blue shaded regions correspond to the $1\,\sigma$ and $2\,\sigma$ confidence regions resulting from the empirical EBL reconstruction method. The data points are independent measurements from integrated galaxy luminosity functions in the literature. We have not corrected the data for evolution from the redshift displayed (e.g. $z = 1$ panel shows measurements at $0.9 < z < 1.15$) which may cause some additional scatter. Our results are in general agreement with the galaxy survey data. The gray lines correspond to the EBL model of Domínguez et al. (2011) where the luminosity density is found to be dominated by a spiral-type galaxy SED template.

culating the optical depths at each energy and redshift bin. Our reconstruction recovers the fake EBL in all cases within the derived $1\,\sigma$ uncertainty region. We see no evidence for a systematic over- or underestimation of the emissivity at any particular wavelength. The largest offsets arise at $> 1\mu$m where the dataset is less constraining.

5.2.14 Comparison with empirical EBL models

The literature offers different approaches to estimate the evolving EBL . There are methodologies that are observationally motivated (Domínguez et al., 2011; Helgason & Kashlinsky, 2012b; Stecker et al., 2016; Driver et al., 2016; Franceschini & Rodighiero, 2017), physically motivated (Kneiske & Dole, 2010; Finke et al., 2010; Khaire & Srianand, 2015; Andrews et al., 2018), and based on semi-analytical models of galaxy formation such as (Gilmore et al., 2012; Inoue et al., 2013). Typically these models are constructed in such a way that the lower redshifts and, in general, the optical/near-IR peak are better constrained. Figure 5.12 shows our reconstructed EBL spectral intensities in comparison with some of the models.

The reconstructed EBL follows galaxy counts (Keenan et al., 2010; Voyer et al., 2011) leaving little room for substantial contributions not resolved by deep galaxy surveys. This is in conflict with several direct measurements of EBL (which may be contaminated by foregrounds, see e.g. (Wright & Reese, 2000; Matsumoto et al., 2005; Matsuura et al., 2017)) and in tension with some models proposed to explain the anisotropies measured in diffuse light (Zemcov et al., 2014).

Relative to EBL models, in the local Universe, we find that our estimate roughly follows the median of existing models. The models by Finke et al. (2010), Kneiske & Dole (2010), Domínguez et al. (2011), Helgason & Kashlinsky (2012b), and Franceschini & Rodighiero (2017) reproduce our results quite well. The fiducial model by Gilmore et al. (2012) tends to follow the upper region of our 1σ band. Finally, the baseline model by Inoue et al. (2013) provides too much UV and too little near-IR.

The strategy of using the observation of γ-ray photons to derive constraints on the

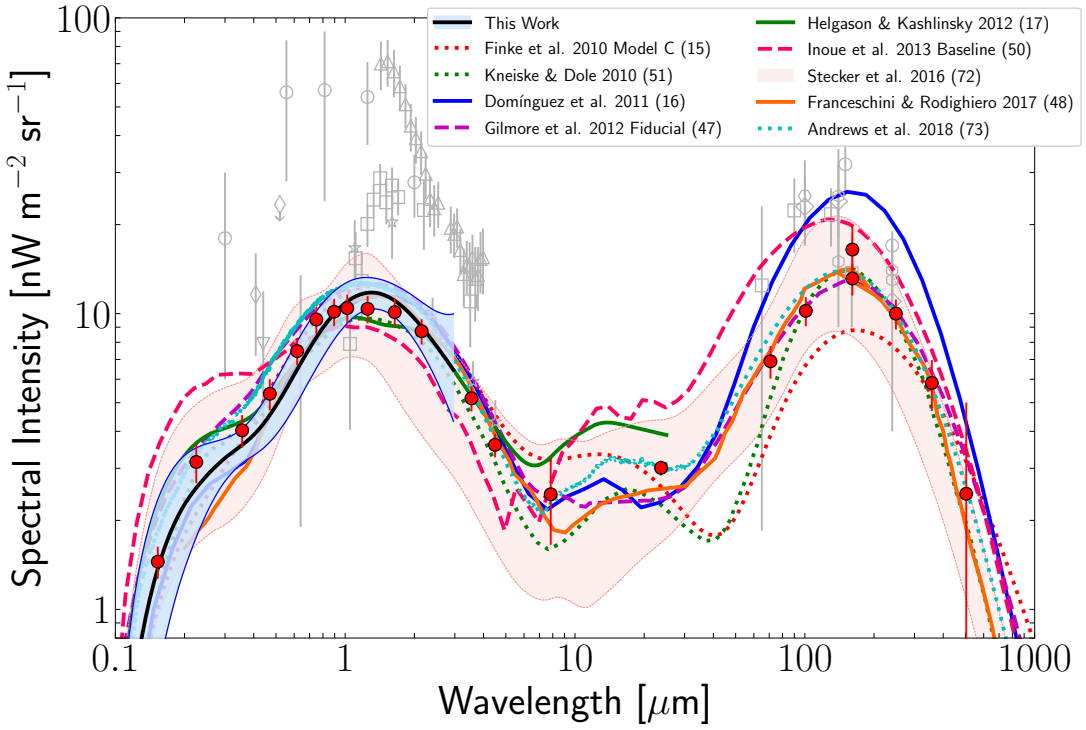

Figure 5.12 SED of the EBL at $z = 0$. Recovered EBL spectral energy distribution at $z = 0$ (solid black line) with its 1σ uncertainties (shaded blue) in comparison with the some estimates from empirical models from ultraviolet to far-IR wavelengths. We show some examples for different modeling methodologies: observationally motivated (solid lines), physically motivated (dotted lines), and theoretically motivated (dashed lines). Our uncertainties start to diverge above the near-IR as a consequence of the larger uncertainties of our optical-depth data at the larger γ-ray energies. A compilation of data from direct detection (open gray symbols) and galaxy counts (filled gray symbols) is also shown. Our spectral intensities match those results from galaxy counts leaving little room for substantial contributions from sources that have not been detected in deep surveys.

background has been used extensively in recent years. Early attempts, characterized by scarcer γ-ray data, only allowed intensity upper limits as a consequence of assumptions on the intrinsic spectra of blazars (Aharonian et al., 2006; Albert et al., 2008; Meyer et al., 2012). These results were followed by more sophisticated approaches based on more and better data that allowed the EBL detection and study, both with the LAT at somewhat lower energies and thus, larger redshifts (Ackermann et al., 2012b; Domínguez & Ajello, 2015; Armstrong et al., 2017; Desai et al., 2017), and with Imaging Atmospheric Cherenkov Telescopes (IACTs), mostly constraining the more local Universe (Abramowski et al., 2013;

Biteau & Williams, 2015; Abdalla et al., 2017). Notably, our derived EBL at $z = 0$ is even closer to the integrated counts compared to previous γ-ray derived EBL measurements.

Table 5.4 reports the EBL spectral intensities at several redshifts as displayed in Figure 6.3. Using Equation 5.6, we can calculate the optical depth curves as a function of energy and redshift from our reconstructed EBL. These can be used to correct spectra of cosmological γ-ray sources for EBL absorption in order to study physical properties of the source.

Table 5.4. Spectral intensity[a] (λI_λ) of the EBL as a function of redshift and wavelengths as reported in Figure 6.3.

λ (μm)	$z = 0$ (nW m^{-2} sr^{-1})	$z = 1$ (nW m^{-2} sr^{-1})	$z = 2$ (nW m^{-2} sr^{-1})	$z = 3$ (nW m^{-2} sr^{-1})
0.102	$0.12^{+0.12}_{-0.07}$	$0.41^{+0.08}_{-0.06}$	$0.36^{+0.11}_{-0.07}$	$0.21^{+0.07}_{-0.08}$
0.111	$0.33^{+0.31}_{-0.20}$	$0.90^{+0.18}_{-0.13}$	$0.72^{+0.20}_{-0.14}$	$0.39^{+0.14}_{-0.15}$
0.120	$0.59^{+0.51}_{-0.34}$	$1.42^{+0.29}_{-0.21}$	$1.05^{+0.28}_{-0.21}$	$0.55^{+0.21}_{-0.23}$
0.130	$0.90^{+0.68}_{-0.49}$	$1.92^{+0.38}_{-0.29}$	$1.33^{+0.36}_{-0.28}$	$0.68^{+0.28}_{-0.30}$
0.141	$1.22^{+0.83}_{-0.63}$	$2.37^{+0.44}_{-0.37}$	$1.55^{+0.40}_{-0.34}$	$0.78^{+0.34}_{-0.35}$
0.153	$1.55^{+0.92}_{-0.74}$	$2.74^{+0.50}_{-0.43}$	$1.71^{+0.45}_{-0.38}$	$0.84^{+0.39}_{-0.39}$
0.166	$1.87^{+0.98}_{-0.84}$	$2.99^{+0.56}_{-0.46}$	$1.80^{+0.47}_{-0.42}$	$0.87^{+0.43}_{-0.42}$
0.180	$2.16^{+0.99}_{-0.87}$	$3.15^{+0.59}_{-0.48}$	$1.82^{+0.48}_{-0.44}$	$0.87^{+0.45}_{-0.42}$
0.195	$2.44^{+0.93}_{-0.89}$	$3.21^{+0.58}_{-0.48}$	$1.79^{+0.47}_{-0.45}$	$0.84^{+0.46}_{-0.42}$
0.212	$2.68^{+0.87}_{-0.86}$	$3.19^{+0.55}_{-0.47}$	$1.72^{+0.46}_{-0.44}$	$0.80^{+0.45}_{-0.41}$
0.230	$2.86^{+0.79}_{-0.79}$	$3.10^{+0.50}_{-0.44}$	$1.62^{+0.45}_{-0.42}$	$0.75^{+0.45}_{-0.38}$
0.249	$3.01^{+0.70}_{-0.69}$	$2.98^{+0.45}_{-0.40}$	$1.52^{+0.43}_{-0.40}$	$0.71^{+0.42}_{-0.36}$
0.270	$3.12^{+0.60}_{-0.56}$	$2.85^{+0.41}_{-0.36}$	$1.44^{+0.40}_{-0.39}$	$0.68^{+0.39}_{-0.35}$
0.293	$3.23^{+0.50}_{-0.48}$	$2.75^{+0.38}_{-0.33}$	$1.40^{+0.38}_{-0.39}$	$0.66^{+0.41}_{-0.36}$
0.318	$3.33^{+0.44}_{-0.41}$	$2.72^{+0.34}_{-0.32}$	$1.39^{+0.42}_{-0.43}$	$0.68^{+0.46}_{-0.39}$
0.345	$3.46^{+0.41}_{-0.42}$	$2.77^{+0.38}_{-0.35}$	$1.45^{+0.52}_{-0.53}$	$0.70^{+0.56}_{-0.43}$
0.374	$3.63^{+0.46}_{-0.48}$	$2.96^{+0.44}_{-0.43}$	$1.57^{+0.71}_{-0.65}$	$0.74^{+0.75}_{-0.48}$
0.405	$3.87^{+0.59}_{-0.62}$	$3.27^{+0.57}_{-0.56}$	$1.77^{+0.96}_{-0.83}$	$0.84^{+0.98}_{-0.58}$
0.440	$4.21^{+0.75}_{-0.80}$	$3.73^{+0.72}_{-0.77}$	$2.04^{+1.28}_{-1.06}$	$0.99^{+1.26}_{-0.72}$
0.477	$4.64^{+0.92}_{-0.98}$	$4.34^{+0.94}_{-1.01}$	$2.38^{+1.69}_{-1.33}$	$1.20^{+1.63}_{-0.92}$
0.517	$5.19^{+1.12}_{-1.20}$	$5.06^{+1.20}_{-1.27}$	$2.80^{+2.12}_{-1.63}$	$1.47^{+2.09}_{-1.18}$
0.561	$5.84^{+1.32}_{-1.42}$	$5.91^{+1.48}_{-1.57}$	$3.27^{+2.58}_{-1.95}$	$1.78^{+2.66}_{-1.45}$
0.608	$6.59^{+1.50}_{-1.65}$	$6.81^{+1.77}_{-1.93}$	$3.79^{+3.07}_{-2.28}$	$2.13^{+3.32}_{-1.75}$
0.660	$7.41^{+1.67}_{-1.87}$	$7.71^{+2.14}_{-2.23}$	$4.32^{+3.55}_{-2.60}$	$2.47^{+4.35}_{-2.06}$
0.716	$8.25^{+1.82}_{-2.02}$	$8.56^{+2.50}_{-2.55}$	$4.88^{+4.01}_{-2.95}$	$2.88^{+5.38}_{-2.41}$
0.776	$9.09^{+1.90}_{-2.13}$	$9.30^{+2.87}_{-2.84}$	$5.48^{+4.56}_{-3.35}$	$3.27^{+6.58}_{-2.72}$
0.842	$9.88^{+1.95}_{-2.16}$	$9.90^{+3.23}_{-3.09}$	$5.98^{+5.15}_{-3.72}$	$3.64^{+7.78}_{-3.02}$
0.913	$10.60^{+1.96}_{-2.18}$	$10.32^{+3.56}_{-3.18}$	$6.52^{+5.88}_{-4.14}$	$3.94^{+9.86}_{-3.25}$
0.990	$11.15^{+1.88}_{-2.06}$	$10.60^{+3.84}_{-3.36}$	$6.83^{+6.60}_{-4.40}$	$4.26^{+12.24}_{-3.52}$
1.074	$11.54^{+1.79}_{-1.90}$	$10.73^{+4.04}_{-3.48}$	$6.97^{+7.81}_{-4.51}$	$4.51^{+15.08}_{-3.73}$
1.164	$11.79^{+1.65}_{-1.76}$	$10.64^{+4.23}_{-3.47}$	$7.04^{+9.00}_{-4.55}$	$4.65^{+19.68}_{-3.87}$
1.263	$11.86^{+1.50}_{-1.58}$	$10.46^{+4.47}_{-3.65}$	$6.91^{+11.27}_{-4.47}$	$4.72^{+28.24}_{-3.94}$
1.370	$11.73^{+1.40}_{-1.41}$	$10.05^{+4.94}_{-3.72}$	$6.87^{+13.94}_{-4.59}$	$4.79^{+40.34}_{-4.00}$
1.485	$11.50^{+1.28}_{-1.38}$	$9.56^{+5.80}_{-3.78}$	$6.81^{+18.49}_{-4.68}$	$4.81^{+58.87}_{-4.05}$
1.611	$11.07^{+1.35}_{-1.35}$	$9.09^{+6.77}_{-3.86}$	$6.52^{+25.41}_{-4.61}$	$4.67^{+84.71}_{-3.96}$
1.747	$10.53^{+1.46}_{-1.42}$	$8.54^{+8.48}_{-3.96}$	$6.20^{+37.72}_{-4.52}$	$4.51^{+117.34}_{-3.86}$
1.895	$9.94^{+1.63}_{-1.53}$	$7.97^{+10.94}_{-4.01}$	$5.77^{+55.07}_{-4.28}$	$4.38^{+156.29}_{-3.84}$
2.055	$9.34^{+1.87}_{-1.70}$	$7.57^{+14.47}_{-4.07}$	$5.51^{+76.16}_{-4.22}$	$4.40^{+213.73}_{-3.90}$
2.229	$8.72^{+2.14}_{-1.86}$	$7.01^{+20.41}_{-4.10}$	$5.38^{+101.00}_{-4.31}$	$4.47^{+271.37}_{-4.03}$
2.417	$8.16^{+2.55}_{-2.03}$	$6.70^{+28.53}_{-4.28}$	$5.24^{+135.49}_{-4.33}$	$4.51^{+341.38}_{-4.11}$
2.621	$7.57^{+3.20}_{-2.16}$	$6.31^{+39.23}_{-4.30}$	$5.28^{+174.14}_{-4.50}$	$4.72^{+415.24}_{-4.37}$
2.843	$7.05^{+4.08}_{-2.33}$	$5.95^{+52.73}_{-4.31}$	$5.38^{+223.92}_{-4.71}$	$4.86^{+494.98}_{-4.55}$
3.083	$6.54^{+5.51}_{-2.48}$	...	...	...
3.344	$6.15^{+7.44}_{-2.69}$	...	...	...
3.626	$5.85^{+9.76}_{-2.91}$	...	...	...
3.933	$5.46^{+13.33}_{-3.03}$	...	...	...
4.265	$5.23^{+17.70}_{-3.21}$	...	...	...
4.626	$5.11^{+23.25}_{-3.44}$	...	...	...
5.017	$5.07^{+30.88}_{-3.70}$	...	...	...

[a]The intensities reported in the this table are in comoving coordinates. To reproduce the results of Figure 6.3 (shown in physical coordinates) they need to be multiplied by a $(1 + z)^3$ factor.

5.2.15 Implications for the high-z Universe

In principle, there is always some constraining power beyond the maximum redshift of the sample of γ-ray sources. This is because the γ rays coming from $z_{\rm max}$ start interacting with EBL photons which were built up at still earlier times and the rate of the interactions is related to $n_{\rm EBL} \propto (1+z)^3$. Focusing on the UV, which is important for cosmic re-ionization, Figure 5.13 suggests rather minimal UV emissivity at $z > 4$ with respect to measurements from Lyman-break galaxy surveys. However, it is possible that the confidence regions at these redshifts may be artificially narrow due to the lack of flexibility in the parameterized shape of the evolution. In order to test the robustness of the constraints at high-z we have re-run the MCMC and included an additional term in Equation 6.3:

$$j_{\rm high-z}(\lambda, z) = a_{\rm high-z} \exp\left[-\frac{(z-z_0)^2}{2\sigma^2}\right] \left(\frac{\lambda}{0.17\mu{\rm m}}\right)^{-0.5} \tag{5.13}$$

centered at $z_0 = 6$ with $\sigma = 0.08$. We find that, while this reveals a relatively unconstrained lower limit for the UV emissivity, the upper limit remains robust at $\sim 3.2(5.3) \times 10^{26}$ erg s^{-1} Mpc^{-3} Hz^{-1}, $1\sigma(2\sigma)$, at $z = 5-6$. In Figure 5.4, we compare this value with the integrated UV luminosity functions from the Hubble Frontier Fields (HFF) program, which targets extremely faint galaxies behind strong gravitational lenses, reaching $M_{\rm AB} \sim -13$. Some HFF analyses have found evidence for a turnover in the steep faint-end of the luminosity function (LF) (Bouwens et al., 2017; Atek et al., 2018), whereas others do not see such a feature (Livermore et al., 2017; Ishigaki et al., 2018). The conflicting results at $M_{\rm AB} \gtrsim -15$ could be due to uncertainties in the magnification factor determined by lens models.

Our constraints limit how far a steep faint-end slope can be extrapolated. In fact, Figure 5.4 shows that the emissivities from the integrated UV luminosity functions are already close to our derived upper limits, but are all compatible within $2\,\sigma$. They favor a turnover of the LF at $M_{\rm AB} \sim -14$ in agreement with Bouwens et al. (2017) and Atek et al. (2018). The UV emissivity implied by Ishigaki et al. (2018) for example (with no turnover), would reach the 2σ upper limit if extrapolated to $M_{\rm AB} \sim -10$.

In Figure 5.4, we also show the UV emissivity necessary to sustain a reionized Universe at $z = 6$. The required emissivity (at $0.15\,\mu$m) can be shown to be (Madau, 1999):

$$j_{\rm UV} = 2.5 \times 10^{26}\ \epsilon_{53}^{-1} \left(\frac{1+z}{6}\right)^3 \left(\frac{\Omega_b h_{70}^2}{0.0461}\right)^2 \left(\frac{C/f_{\rm esc}}{30}\right)^2 \quad {\rm erg\ s^{-1}Mpc^{-3}Hz^{-1}}. \quad (5.14)$$

Here, Ω_b is the cosmic baryon density, h_{70} is Hubble parameter in units of $70\,{\rm km\ s^{-1}Mpc^{-1}}$, C is the clumping factor of ionized hydrogen and $f_{\rm esc}$ is the mean escape fraction of ionizing photons. The parameter ϵ_{53} is the number of Lyman continuum photons per unit of forming stellar mass in units of 10^{53} photons $\cdot {\rm s^{-1}(M_\odot \cdot yr^{-1})^{-1}}$. For this we follow Finkelstein et al. (2012) exploring values of ϵ_{53} based on stellar population synthesis models assuming a Salpeter IMF and a constant star formation rate. The width of the grey regions in Figure 5.4 correspond to the range $0.9 < \epsilon_{53} < 1.4$ when the metallicity is varied from $0.02Z_\odot$ to $1.0Z_\odot$ (where $Z_\odot$ is the solar metallicity). We display the emissivity for a reasonable assumption of $C/f_{\rm esc} = 30$, showing that our constraints accommodate a scenario in which the Universe is reionized at $z = 6$.

Our constraints at $z > 4$ come almost entirely from GRB 080916C which provides a strong upper limit to the optical depth at $z = 4.35$ whereas the blazar sample alone ($z < 3.1$) has lower constraining power. This is a benefit of detecting more high-z γ-ray sources as probes of the epoch of re-ionization (Kashlinsky et al., 2005).

5.2.16 The Star-Formation History

We derive the SFH from our constraints on the far-UV emissivity in a similar manner to galaxy surveys that measure the rest-frame UV emission (Schiminovich et al., 2005; Bouwens et al., 2014; McLure et al., 2013; Ellis et al., 2013; Finkelstein et al., 2015b). The conversion into star-formation rate (SFR) requires two assumptions: i) the amount of UV emission expected per unit SFR, $\mathscr{K}_{\rm UV}$, which is dictated by the initial mass function (IMF) of choice, and ii) the mean dust extinction within the host galaxies, A_V, since photons

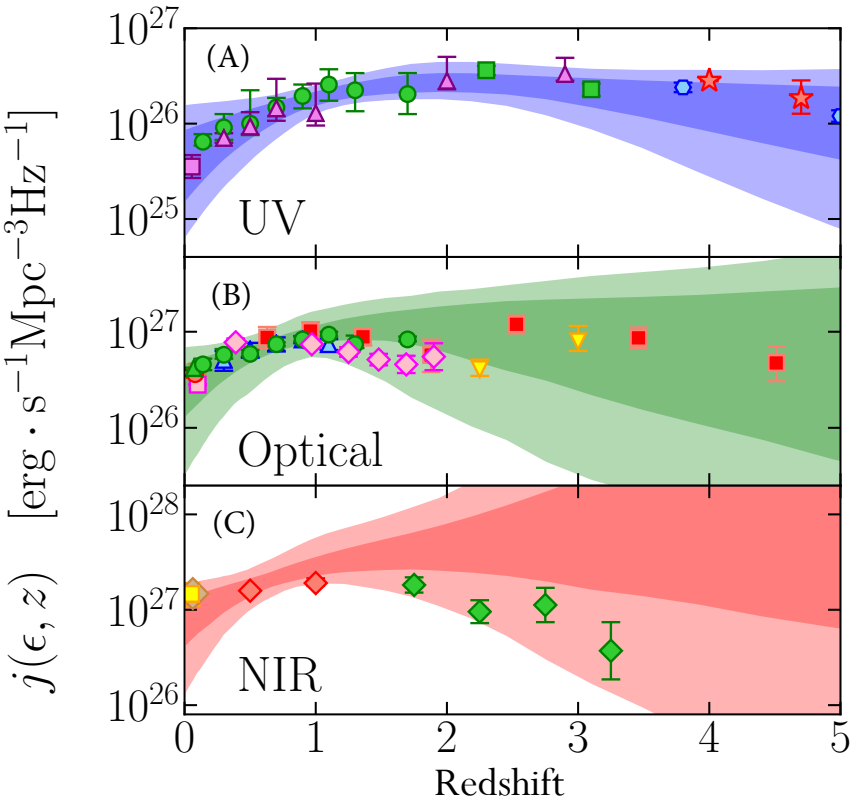

Figure 5.13 Evolution of the cosmic emissivity. The evolution of the cosmic emissivity at UV (0.16 m), optical (0.45 m) and NIR (1.6 m), panels A, B and C respectively. The shaded regions show the 1σ and 2σ confidence regions resulting from the empirical EBL reconstruction model. The data points shown have rest-frame wavelengths in the range 0.15-0.17m, 0.42-0.48m and 1.25-1.27m in the UV, optical, and NIR panels respectively. Colors and symbols follow the same scheme as in Figure 5.11.

become a part of the EBL only if they escape their progenitor galaxies. For the former quantity, we assume $\mathscr{K}_{\rm UV} = 7.25 \times 10^{-29} {\rm M}_{\odot}$ yr^{-1} erg^{-1} s Hz which is consistent with a Chabrier IMF (Chabrier, 2003). Our results on the SFH can be re-scaled by constant factor of 1.6 to represent a Salpeter IMF (Salpeter, 1955).

For the dust extinction correction, we rely on measured values of the mean A_V from the literature and fit its evolution with redshift using the following parametrization: $A_V \propto \frac{(1+z)^f}{1+\left(\frac{1+z}{c}\right)^d}$. The result is shown in Figure 5.14. The measured values of A_V are based on different methods. For instance, these come from: measured UV continuum slopes (Bouwens et al., 2014, 2016), stellar population synthesis SED fitting (Cucciati et al., 2012a; Andrews et al., 2017) and comparison of the integrated UV and IR luminosity functions (Takeuchi et al., 2005; Burgarella et al., 2013). We choose to use only those data that are measured from a large sample where robust uncertainty estimation is provided. Studies that assume or estimate values of A_V do not contribute to the fit but are shown in Figure 5.14 for reference. We obtain the evolving extinction:

$$A_V(z) = (1.49 \pm 0.07) \frac{(1+z)^{(0.64 \pm 0.19)}}{1 + [(1+z)/(3.40 \pm 0.44)]^{(3.54 \pm 0.47)}}. \tag{5.15}$$

The SFH is then calculated as:

$$\rho_{\star}(z) = j_{\rm UV}(z) \cdot \mathscr{K}_{UV} \cdot 10^{0.4 A_V} \tag{5.16}$$

where $j_{\rm UV}(z)$ is our reconstructed emissivity at 1600Å.

The confidence regions for the cosmic SFH are shown in Figure 5.3 in the main paper along with data points from UV-derived measurements (Madau & Dickinson, 2014). We also display the same result in Figure 5.15 showing data from various studies using different tracers of SFR, including limits from γ-ray constraints of the EBL (Raue & Meyer, 2012). At low and intermediate redshifts, our results are in good agreement with (albeit a little bit above) independent measurements from galaxy surveys. At $z > 3$, our results are in agreement, within the uncertainties, but favor a rather low SFH. As discussed in the

previous subsection, this is primarily driven by GRB 080916C. More importantly, because the SFH derived from γ-ray absorption complements traditional methods that probe the SFH from sources resolved in surveys, our results imply that the bulk of star formation across cosmic time is already accounted for by surveys.

5.2.17 Stellar Population Model Method

The cosmic SFH, $\dot{\rho}(z)$, is the starting point in the EBL model of Razzaque et al. (2009); Finke et al. (2010) making it a useful model for further exploration of the parameter space that is made possible by the γ-ray optical depth data. The model assumes that stars emit as blackbodies, with their temperatures, luminosities, and time evolution determined from formulae given by Eggleton et al. (1989). The radiation emitted by stars is convolved with an IMF and star-formation rate density parameterization to get the luminosity density $j(\epsilon; z)$. The fraction of light that escapes dust extinction ($f_{\rm esc,dust}$) is based on the extinction curve from Driver et al. (2008), which was derived from a fit to the luminosity density data in the local Universe. We let the dust extinction evolve according to Equation 5.15. The infrared portion of the EBL is computed assuming that all the energy absorbed by dust is re-radiated in the infrared. The SFH and IMF model parameters were chosen to reproduce the luminosity density data available at the time. Once $j(\epsilon; z)$ is calculated, the EBL number density and γ-ray absorption optical depth are computed from Equations 5.6–5.8 above.

Using the methodology of Finke et al. (2010), we have performed an MCMC fit to the γ-ray optical depth data. We parameterize the SFH and let the parameters vary, calculating the resulting EBL and optical depths in each step. A similar MCMC model fit, but limited to $z \geq 2$, was done by Gong & Cooray (2013) to the earlier EBL absorption data from Ackermann et al. (2012b). We use the standard parameterization for the SFH (Equation 6.3), but also consider evolution according to Equation 5.11. The SFH result from our MCMC fits, reported in Figure 5.3 (as the green confidence region), are consistent with the SFH used for the "model C" of Finke et al. (2010), which relied on the Cole et al. (2001) parametrization with free parameters given by Hopkins & Beacom (2006), at all values of

Table 5.5. The Cosmic star-formation history as reported in Figure 5.3.

z	Physical EBL model ($10^{-2}\mathrm{M}_\odot\,\mathrm{yr}^{-1}\,\mathrm{Mpc}^{-3}$)	EBL Reconstruction ($10^{-2}\mathrm{M}_\odot\,\mathrm{yr}^{-1}\,\mathrm{Mpc}^{-3}$)
0.0	$0.8^{+0.7}_{-0.3}$	$1.2^{+1.3}_{-0.7}$
0.1	$1.1^{+0.8}_{-0.4}$	$1.6^{+1.4}_{-0.9}$
0.2	$1.6^{+0.9}_{-0.5}$	$2.1^{+1.4}_{-1.1}$
0.3	$2.0^{+0.9}_{-0.5}$	$2.7^{+1.4}_{-1.2}$
0.4	$2.6^{+0.8}_{-0.6}$	$3.4^{+1.4}_{-1.4}$
0.5	$3.3^{+0.8}_{-0.6}$	$4.2^{+1.4}_{-1.5}$
0.6	$4.1^{+0.8}_{-0.7}$	$5.0^{+1.4}_{-1.5}$
0.8	$6.0^{+1.0}_{-0.9}$	$6.8^{+1.5}_{-1.4}$
1.0	$8.2^{+1.6}_{-1.4}$	$8.5^{+1.6}_{-1.3}$
1.2	$10.7^{+2.0}_{-2.2}$	$10.0^{+2.1}_{-1.5}$
1.4	$12.9^{+2.5}_{-2.8}$	$11.0^{+2.3}_{-1.8}$
1.6	$14.5^{+2.3}_{-2.9}$	$11.3^{+2.9}_{-2.0}$
1.8	$15.0^{+2.3}_{-2.5}$	$11.0^{+3.1}_{-2.0}$
2.0	$14.7^{+2.4}_{-2.4}$	$10.4^{+3.0}_{-1.9}$
2.5	$11.6^{+3.2}_{-2.9}$	$7.9^{+2.2}_{-1.7}$
3.0	$7.6^{+3.3}_{-2.4}$	$5.6^{+1.8}_{-1.8}$
3.5	$4.8^{+2.6}_{-1.8}$	$4.0^{+1.5}_{-1.7}$
4.0	$3.1^{+2.0}_{-1.3}$	$2.8^{+1.5}_{-1.5}$
4.5	$2.0^{+1.6}_{-0.9}$	$2.1^{+1.4}_{-1.3}$
5.0	$1.3^{+1.3}_{-0.7}$	$1.6^{+1.4}_{-1.1}$
5.5	$0.9^{+1.1}_{-0.5}$	$1.2^{+1.3}_{-0.9}$
6.0	$0.6^{+1.0}_{-0.3}$	$1.0^{+1.3}_{-0.8}$

z, but the confidence interval is particularly narrow up to $z \leq 2.5$. Table 5.5 reports the values of the SFH obtained from both methods as displayed in Figure 5.3.

5.2.18 The contribution of Active Galactic Nuclei

The methods employed here to derive the SFH of the Universe rest on the assumption that most of the EBL is the product of stellar emission. While this is almost certainly true in the IR and optical bands, there could be a non-negligible contribution of active galactic nuclei (AGN) to the global UV background (Domínguez et al., 2011). We estimate this contribution by considering measurements of the integrated quasar luminosity function. A

fitting formula for the resulting emissivity as a function of redshift was provided by Madau & Haardt (2015) at a rest-frame wavelength of 912Å. We convert this to $0.16\,\mu$m (the wavelength used to estimate our SFH) adopting the same power law spectrum $\propto \lambda^{-0.61}$ (Lusso et al., 2015) and show the ratio of the AGN to total (as estimated in this work) emissivities at $0.16\,\mu$m in Figure 5.16. This shows that the contribution from known AGN is no more than a few percent. This is in agreement with the recent estimate of the AGN contribution to the EBL (Andrews et al., 2018).

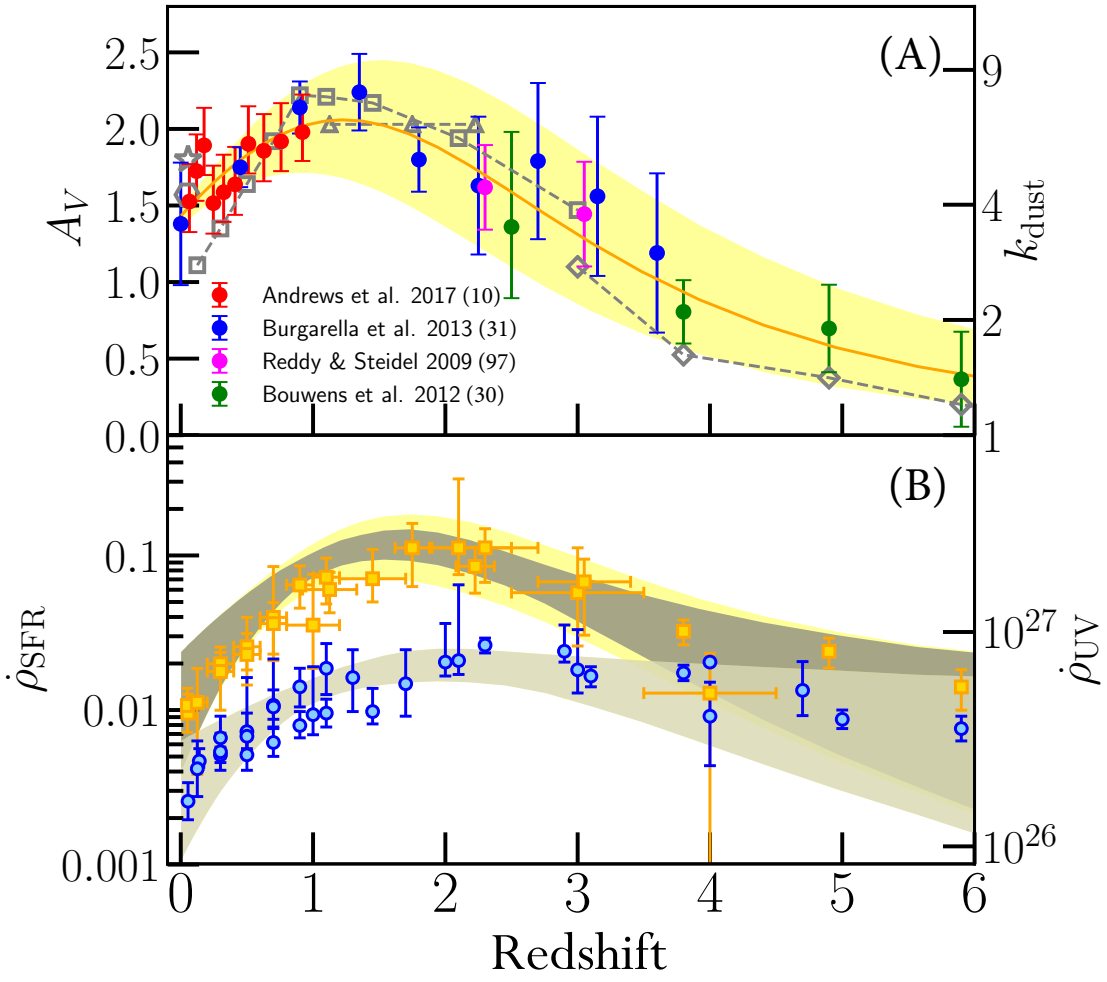

Figure 5.14 The effects of dust extinction on the derived SFH. *Panel A:* The mean dust extinction as a function of redshift. The solid line is our best fit (see Equation 5.15) with uncertainty shown as yellow region. Data points used for the fit (filled circles) are from Andrews et al. (2017); Burgarella et al. (2013); Reddy & Steidel (2009); Bouwens et al. (2012). Also shown as gray connected points are estimates from other references without published uncertainties: Wyder et al. (2005) (star), Robotham & Driver (2011) (hexagon), Dahlen et al. (2007) (triangles), Cucciati et al. (2012b) (squares), Bouwens et al. (2016) (diamonds). Right vertical axis shows the multiplicative factor $k_{\rm dust} = 10^{0.4A_V}$. *Panel B:* The SFH corrected (dark gray) and uncorrected (light gray) for dust extinction (in $M_\odot$ yr^{-1}Mpc^{-3}). Yellow region includes the systematic uncertainty from the dust correction **which has been added in quadrature to the statistical uncertainties**. The data points show the corrected (orange) and uncorrected (blue) SFH from the compilation of Madau & Dickinson (2014) with the addition of Yoshida et al. (2006) and Tresse et al. (2007). Right vertical axis shows the UV emissivity in units of erg s^{-1}Mpc^{-3}Hz^{-1}.

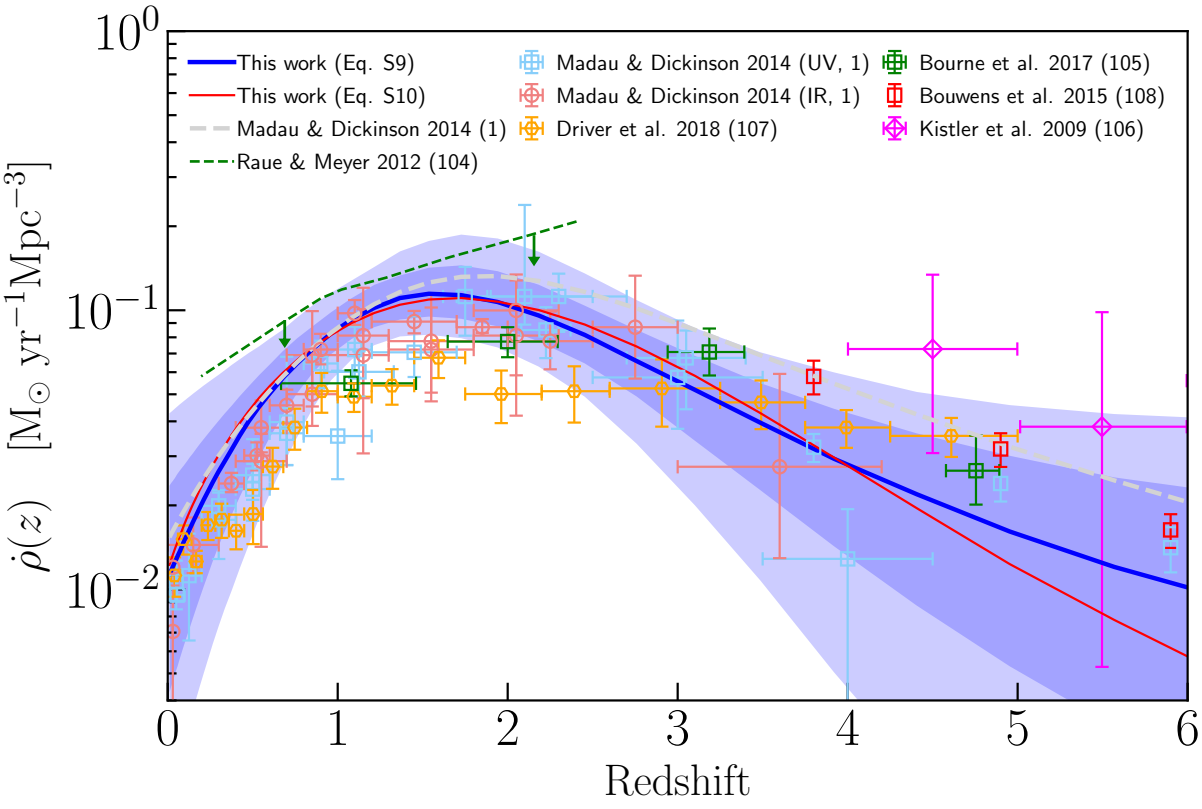

Figure 5.15 The star-formation history of the Universe. Results for the SFH compared with data from the literature. The blue and red lines compare the median SFH resulting from our EBL reconstruction using the evolution parameterization in Eq. 6.3 from Madau & Dickinson (2014) versus the parametrization in Eq. 5.11 from Cole et al. (2001). The blue regions show the 1σ and 2σ confidence intervals (pMD). The dashed gray line shows the fit from Madau & Dickinson (2014) and dashed green line are upper limits from γ-ray data derived by Raue & Meyer (2012) where they assume a Chabrier IMF and $\beta = 0.3$. Data points are from the compilation of Madau & Dickinson (2014) with the addition of data from Bourne et al. (2017); Kistler et al. (2009); Driver et al. (2018); Bouwens et al. (2015b). The data have been corrected for variations in the adopted IMF to $\mathscr{K}_{\rm UV} = 7.25 \times 10^{-29}$ consistent with a Chabrier IMF (see text).

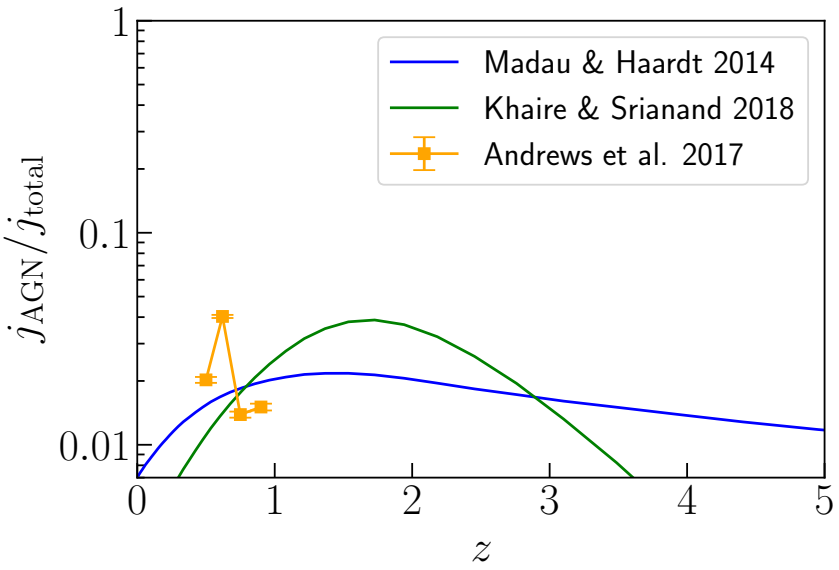

Figure 5.16 Ratio of emissivities of AGN vs total at 0.16 μm. The $j(\epsilon, z)_{\rm total}$ comes from the median UV emissivity derived from the optical depth data. The AGN emissivity is taken from the empirical fit of integrated quasar luminosity functions (converted to 0.16μm) provided by Madau & Haardt (2015) and Khaire & Srianand (2018), plotted in blue and green respectively.

Chapter 6

EBL measurements using AGN observed using Cherenkov Telescopes

The The Fermi-LAT Collaboration (2018) work made use of blazar data observed only using the *Fermi*-LAT in the 1 GeV−1 TeV regime allowing us to strongly constraining the EBL intensity at UV and optical wavelengths. To improve upon this measurement even further and also obtain a stronger constrain on IR portion of the EBL, we made use of blazar observations from Cherenkov Telescopes in the 100 GeV−21 TeV regime (Desai et al., 2019a) and combined it with the The Fermi-LAT Collaboration (2018) results. This allowed us to obtain the best possible determination of the EBL intensity till date (in the ∼0.1-100μm wavelength range) which can be improved upon only after using future observations made using the upcoming Cherenkov Telescope Array (CTA). The following sections are taken from Desai et al. (2019a) [1].

6.1 Introduction

The Extragalactic Background Light (EBL) is the diffuse background radiation accumulated over the cosmic history at ultraviolet (UV), optical and infrared (IR) wavelengths

[1] https://doi.org/10.3847/2041-8213/ab0c10

(e.g. Dwek & Krennrich, 2013). The local EBL energy spectrum comprises two peaks, with the first peak (≈ 1 μm) due to direct emission from stars and the second peak (≈ 100 μm) due to reprocessed star-light emission by dust within galaxies(Brun, 2013). Measurements of both the EBL spectral intensity and its evolution are important to study both star formation and galaxy evolution processes (e.g. Raue & Meyer, 2012; Cowley et al., 2018; Khaire & Srianand, 2018).

Measuring the EBL brightness has proven challenging mainly due to bright foreground contaminants such as the Zodiacal Light and the Diffuse Galactic Light (Hauser et al., 1998). Studying the signatures left by the EBL in the spectra of distant γ ray sources, via the photon-photon interaction, is emerging as the most powerful technique to probe the EBL. Various attempts have been made to constrain the EBL intensity using the absorption found in the spectrum of Blazars at 0.1-100 GeV high energy (HE) and 0.1-30 TeV very high energy (VHE). The constraints came first in the form of upper limits on the intensity (e.g. Aharonian et al., 2006; Mazin & Raue, 2007; Meyer et al., 2012) and later as measurements of the actual levels (e.g. Ackermann et al., 2012b; Abramowski et al., 2013a; Biteau & Williams, 2015; Ahnen et al., 2016). However, the majority of these measurements rely on scaling existing EBL models (e.g. Kneiske & Dole, 2010; Finke et al., 2010; Domínguez et al., 2011; Gilmore et al., 2012; Stecker et al., 2016) in amplitude. To improve this, we have developed a method to reconstruct the EBL spectrum and evolution based on measured γ ray optical depths (see The Fermi-LAT Collaboration, 2018).

In this Letter, we apply this newly developed tool to measure the EBL using both GeV and TeV data. While the GeV optical depths are taken from The Fermi-LAT Collaboration (2018), the TeV optical depths are derived using the multiple spectra of 38 TeV blazars reported in Biteau & Williams (2015). The combined data-set enables us to consistently constrain the EBL spectral intensity in the wavelength regime 0.1 μm to 100 μm. The paper is organized as follows: in Section 6.2 we describe the procedure used to derive the TeV optical depths, in Section 6.3 we describe the methodology used to reconstruct the EBL and in Section 6.4 we discuss the implications of our measurements.

6.2 Analysis

6.2.1 The intrinsic blazars' spectra

Our analysis relies on the 106 VHE gamma-ray spectral energy distributions (SEDs) of 38 blazars reported in Biteau & Williams (2015). The source photons in this sample originate from $z = 0.019$ to $z = 0.604$ and are detected in the 0.1 TeV to 21 TeV range. The SEDs are modeled in this energy range using:

$$\frac{dN}{dE}_{\text{obs}} = \frac{dN}{dE}_{\text{int}} \cdot e^{-b \cdot \tau_{\text{model}}} \tag{6.1}$$

where, dN/dE_{int} and dN/dE_{obs} are the intrinsic and observed blazar spectrum respectively, $\tau_{model}(E)$ is the optical depth estimated by EBL models at the source redshift (e.g. Kneiske & Dole, 2010; Finke et al., 2010; Domínguez et al., 2011; Gilmore et al., 2012) and b is a renormalization constant to scale the optical depth.

To model the intrinsic spectrum we follow the methodology similar to previous analyses of VHE data where four different intrinsic spectral functions are used (see also Biteau & Williams, 2015; Acciari et al., 2019). These models are power law, log-parabola, power law with exponential cutoff and log-parabola with exponential cutoff. For a given EBL model (see e.g. Tab. 1), the intrinsic spectrum of a source is then chosen by adopting the function that produces the highest χ^2 probability when $b = 1$.

For a given EBL model and for each source, a likelihood profile of the re-normalization constant b is produced. This is transformed into a test statistic (TS) profile, by subtracting the value of the log-Likelihood at b=0 and multiplying by two. For a given EBL model, the TS profiles of all sources are summed generating a "stacked" TS, which allows us to identify the best-fit value of b for all spectra. This stacked TS value also displays the significance of the result as $\sqrt{TS}$ (see also Ackermann et al., 2012b; Abramowski et al., 2013a; Desai et al., 2017). The stacked TS vs b profile for one EBL model is shown in Fig 6.1. There is a maximum TS of 117.83, which implies a detection at approximately $10.85\,\sigma$. Table 6.1 shows the results obtained using five different EBL models.

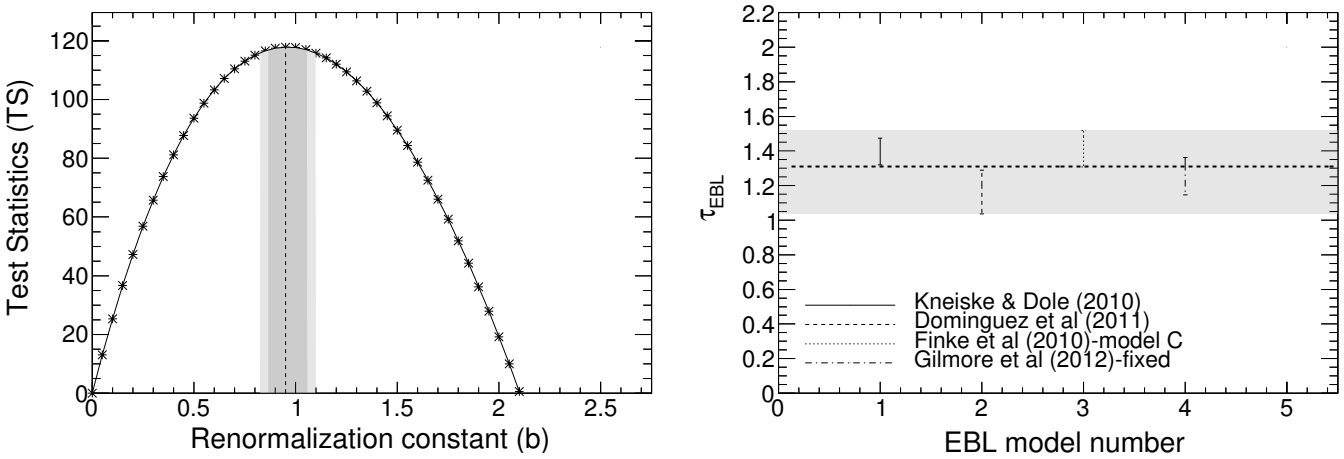

Figure 6.1 Left: Stacked TS profile obtained for a range of b values using the EBL optical depths given by Biteau & Williams (2015). The dotted line shows the best-fit value of b for the given EBL model. The shaded dark gray region highlights the $1\,\sigma$ contour while light gray region shows the $2\,\sigma$ contour. Right: Example of how the optical depth is derived for a given energy and redshift bin using the values of τ derived using four different EBL model. The horizontal dashed line shows the best-fit value of the optical depth, while its uncertainty (the gray band) is chosen to encompass the uncertainty of all models.

6.2.2 Deriving the EBL optical depths

In order to measure the optical depth, we perform a stacking analysis where the source sample is divided into two redshift bins and the analysis is performed across four energy bins. While the two redshift bins ($0.01 < z < 0.04$ and $0.04 < z < 0.604$) are chosen such that they contain the same signal strength (TS contribution to the analysis described in Section 6.2.1), the energy bins are chosen to have equal logarithmic widths. For each energy and redshift bin, a stacked TS vs b profile is derived using the method described in Section 6.2.1 where the source sample and energy range is modified according to the bin being considered. The corresponding b value, in each redshift and energy bin, is then used alongside the EBL model being tested to obtain the optical depth (as obtained using that model).

We perform the above binned analysis for four[2] different EBL models (Finke et al.,

[2]The optical depths reported in Biteau & Williams (2015) were optimized relying on the data used in this work and as such are not used here.

Table 6.1. Results of EBL models tested using VHE data

Model	$b_{best-fit}$ [a]	Test Statistic [b]
Finke et al. (2010) – model C	$1.05^{-0.15}_{+0.12}$	71.60
Kneiske & Dole (2010)	$1.4^{-0.16}_{+0.14}$	99.47
Domínguez et al. (2011)	$0.85^{-0.10}_{+0.08}$	105.98
Gilmore et al. (2012) – fixed	$1.00^{-0.16}_{+0.12}$	106.13
Biteau & Williams (2015)	$0.95^{-0.08}_{+0.11}$	117.83

[a]Best-fit renormalization constant derived from the stacking analysis

[b]TS obtained by comparing the log likelihood obtained for the null case of $b = 0$ with the value obtained for $b = b_{best-fit}$.

2010; Kneiske & Dole, 2010; Domínguez et al., 2011; Gilmore et al., 2012). In a given energy and redshift bin, the optical depth is derived as the mean of the four individual optical depth measurements (derived using four different EBL models), while the uncertainty is chosen as the one that encompasses the uncertainties of all the optical depth measurements, as shown in Figure 6.1. Along with the statistical uncertainties, the uncertainty on the optical depth includes a systematic contribution due to the difference in shape of the optical depth curve estimated from EBL models, the intrinsic model used in Equation 6.1 and the systematic energy bias of $\approx 10\%$ found in TeV data measured using Cherenkov telescopes(Meyer et al., 2010). As in Biteau & Williams (2015), the impact of these systematic uncertainties on the EBL optical depth is estimated to be $\approx 2 - 5\%$. We include these uncertainties in our measurement of the derived optical depth values and show it in Fig. 6.2. These optical depth measurements are also made available on an online database.[3]

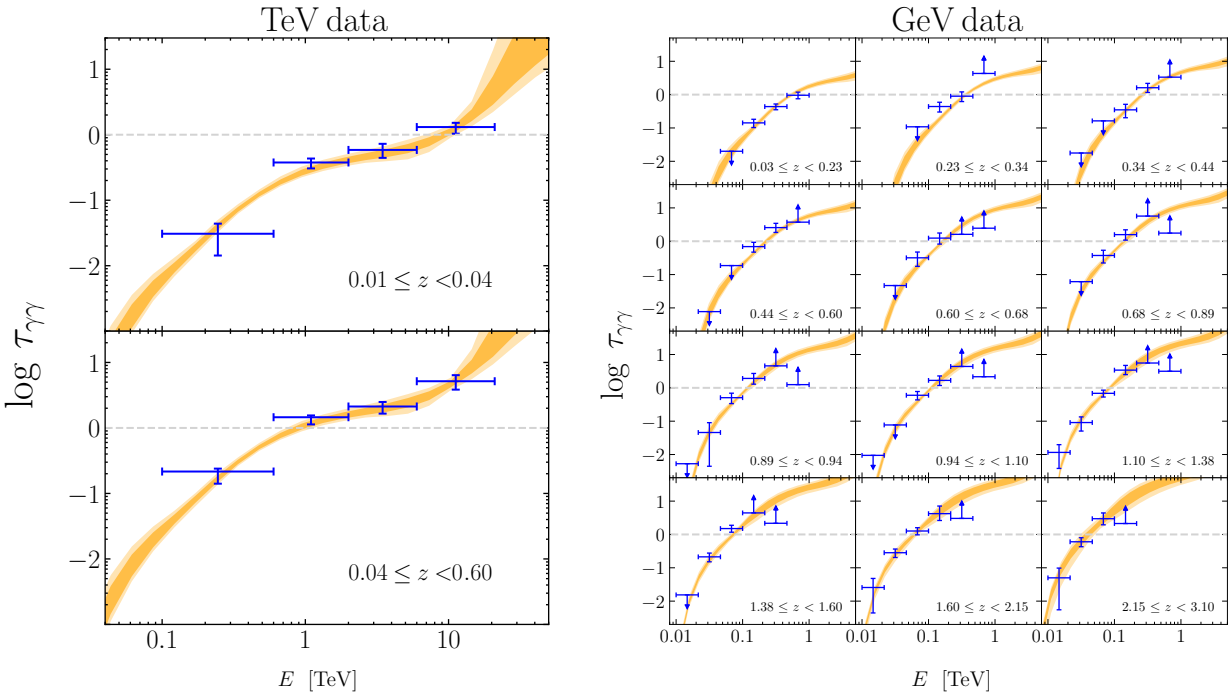

Figure 6.2 Redshift binned optical depth measurements derived from the stacking analysis using VHE data (left) and *Fermi*-LAT data (right) are shown compared to the optical depth templates reported by this work. The shaded regions signify the 1σ and 2σ confidence regions of our best-fitting EBL reconstruction.

6.3 Reconstructing the EBL

We use the derived optical depths to reconstruct the absorbing EBL in a model independent way. In what follows, we include optical depth measurements at $\lesssim 1$ TeV by The Fermi-LAT Collaboration (2018) based on a sample of 739 blazars observed by *Fermi*-Large Area Telescope (LAT). These measurements provide $\tau(E, z)$ in twelve redshift bins in the $z = 0.03 - 3.1$ range and are thus highly complementary to our VHE data-set. Whereas the optical depths at VHE constrain the local EBL from optical to far-IR wavelengths, the *Fermi*-LAT data-set probes the UV to optical out to high redshifts. In terms of wavelength and redshift coverage, the combined data-set results in the most extensive constraints of the EBL to date.

[3] `https://figshare.com/s/9cd4f26925945470582a`.

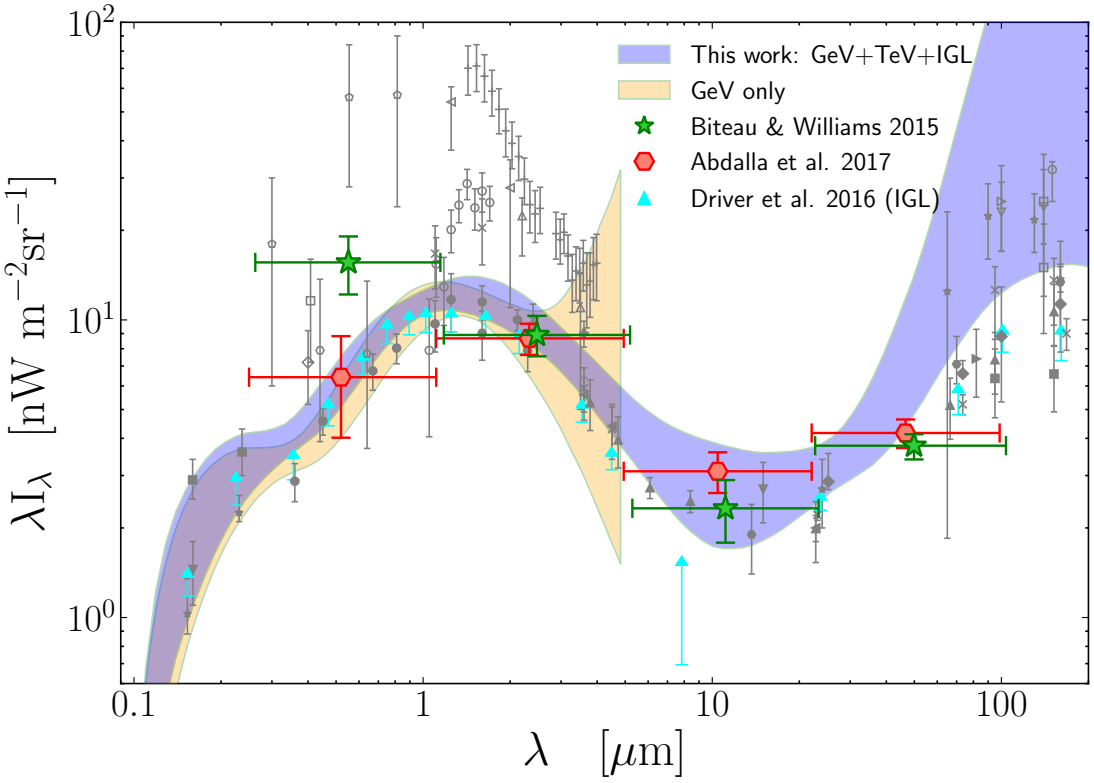

Figure 6.3 The spectral intensity of the EBL from UV to far-IR. The constraints from this work are shown as a 68% confidence region and median (blue). A corresponding region from (The Fermi-LAT Collaboration, 2018) that relies on GeV data only is shown in orange. Various measurements in the literature are shown in gray: direct measurements (open symbols), integrated galaxy counts (filled symbols). The numerical data of the blue and orange curves are available at `https://figshare.com/s/9cd4f26925945470582a`.

We follow the novel methodology presented by The Fermi-LAT Collaboration (2018), where the cosmic emissivity (luminosity density) is modeled as the sum of several log-normal templates with a fixed peak position

$$j(\lambda) = \sum_i a_i \cdot \exp\left[-\frac{(\log\lambda - \log\lambda_i)^2}{2\sigma^2}\right] \tag{6.2}$$

in $\mathrm{erg}\cdot\mathrm{s}^{-1}\mathrm{cm}^{-3-1}$ where the pivots are logarithmically spaced with $\Delta_{\mathrm{lg}\lambda} = 0.5$, resulting in seven templates centered at $\lambda_i = [0.16, 0.50, 1.6, 5.0, 16, 50, 160]\mu$m. We fix $\sigma = 0.2$, and leave the amplitudes a_i free to vary. We tried varying the number of templates and their placement under the condition that $\sigma = \Delta_{\mathrm{lg}\lambda}/2.5$ and find that the local EBL is always consistent within the one sigma confidence region of the final result shown in Figure 6.3. Each template is allowed to evolve independently with redshift according to

$$j(\lambda_i, z) = j_0(\lambda_i) \cdot \begin{cases} \frac{(1+z)^{b_i}}{1+\left(\frac{1+z}{c_i}\right)^{d_i}}, & i \leq 3 \\ (1+z)^{b_i}, & i > 3, \end{cases} \tag{6.3}$$

where $j_0(\lambda_i) \equiv j(\lambda_i, z = 0)$ is the emissivity at the present time centered at λ_i. We reduce the number of parameters by splitting the evolution form at $\lambda \simeq 5\mu$m as the TeV sources are only sensitive to EBL photons at low-z towards infrared wavelengths. This results in 18 free parameters.

The local EBL is obtained from the evolving emissivity $j(\lambda, z)$:

$$\lambda I_\lambda = \frac{c}{4\pi}\int \lambda' j(\lambda', z)\frac{dt}{dz}\frac{dz}{(1+z)} \tag{6.4}$$

where $\lambda' = \lambda/(1+z)$ is the rest-frame wavelength.

The MCMC code `emcee` (Foreman-Mackey et al., 2013), a Python implementation of an affine invariant MCMC ensemble sampler (Goodman & Weare, 2010), is used to constrain the parameters controlling the emissivity. With the emissivity specified as a function of wavelength and redshift, we calculate the resulting EBL and optical depth at 14 redshifts

corresponding to each of the bins in Figure 6.2. In addition to the optical depth data, we have included the integrated galaxy counts from Driver et al. (2016) as lower limits on the EBL at $z = 0$. These are taken to be the lower uncertainty for the galaxy light data obtained by integrating over the observed magnitude range only i.e. not extrapolated[4]. The likelihood function is estimated as $\mathscr{L} \propto \exp(-\chi^2)$ where the total number of optical depth data points and EBL lower limits used to calculate χ^2 is 97. Our final results are based on MCMC chains from 120 walkers exploring the parameter space in 10,000 steps each. This results in 1,140,000 steps after a burn-in of 500 steps for each walker. We refer to The Fermi-LAT Collaboration (2018) for details.

6.4 Discussion

The measured constraints on the local EBL with a 68% confidence region are displayed in Figure 6.3. For a comparison, we also show previous measurements reported in the literature. While the results are in good agreement with the *Fermi*-LAT measurement (orange) relying on GeV data only (The Fermi-LAT Collaboration, 2018), a minor difference is seen in the higher end of the uncertainty at $\approx 2\,\mu m$ which is mainly driven by the Cherenkov measurements of the repeatedly observed Mkn 421 and Mkn 501.

The slightly larger-intensity of the GeV+TeV+IGL result, as compared to GeV only, is not entirely due to the inclusion of the IGL lower limits. In fact, examining the reduced $\chi^2 = \chi^2_{\rm GeV+TeV} + \chi^2_{\rm IGL}$ shows that the GeV+TeV dataset prefers this intensity independently of the IGL lower limits. In other words, lowering the EBL intensity does not improve $\chi^2_{\rm GeV+TeV}$. This is also reflected in the reconstructed optical depths shown in Figure 6.2 which do not show systematically higher optical depths with respect to the data. However, we find that the IGL lower limits help constrain the spectral shape of the EBL, making the result less dependent on the placement of the spectral templates (λ_i). This is not surprising since the optical depth at a given energy is an integral over the EBL wavelengths encompassed by the photon-photon interaction cross-section.

[4]We take the lower of the two PACS160 values given in Table 2 of Driver et al. (2016)

An overall agreement is found with independent EBL measurements, both integrated galaxy counts and other γ-ray absorption studies. The combined GeV+TeV data-set is also sensitive to EBL photons in the mid-IR ($\lesssim 100\mu$m) where we find good agreement with previous studies (Biteau & Williams, 2015; Driver et al., 2016; H.˜E.˜S.˜S. Collaboration et al., 2017). However, the γ ray dataset has no constraining power at $\gtrsim 100\mu$m and the lower limits therefore push the EBL to higher far-IR values.

Our measurements are particularly valuable in the UV/optical, where previous γ-ray absorption studies had limited sensitivity , integrated counts show conflicting results (Gardner et al., 2000; Xu et al., 2005; Voyer et al., 2011) and direct measurements remain somewhat above the counts data (Bernstein, 2007; Matsuoka et al., 2011; Mattila et al., 2017).

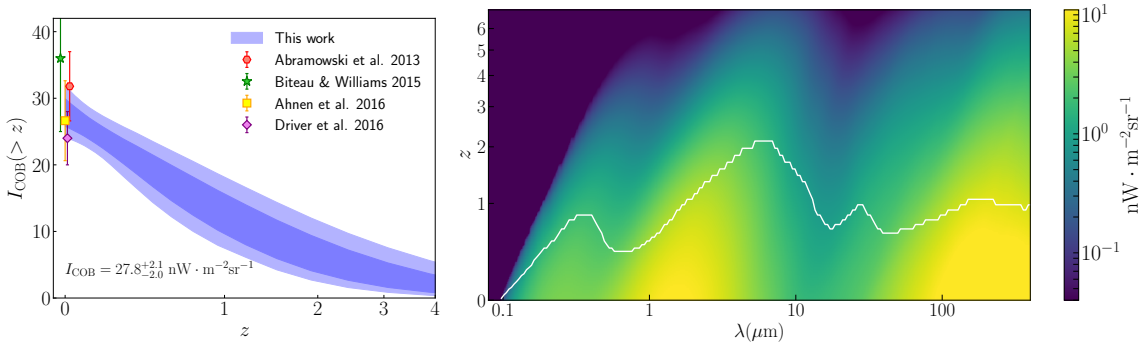

Figure 6.4 The build-up of the local EBL. The EBL at $z > 0$ is shown in comoving coordinates as a function of the observed wavelength. *Left panel:* The median and 68% confidence region of the build-up of the total background, integrated in the 0.1–8μm range. Also displayed are γ-ray derived measurements of the COB at $z = 0$ from Abramowski et al. (2013a); Biteau & Williams (2015); Ahnen et al. (2016) and integrated counts from Driver et al. (2016). *Right panel:* The color map shows the median spectral intensity depicting the origin of the $z = 0$ EBL at a given wavelength. The white continuous line marks the redshift at which 50% of the local EBL has been accumulated. As the image shows the median EBL without uncertainties, we caution that the IR part is very poorly constrained i.e. towards the upper right corner of the image.

A key result of this work is a minimal EBL measurement throughout the wavelength range with respect to integrated galaxy light, allowing very little additional unresolved emission from faint or truly diffuse populations. We estimate the integrated cosmic background

in the [0.09-8] μm range, often referred to as the cosmic optical background (COB), to be $27.8^{+2.1}_{-2.0}$ nW $\cdot$ m^{-2}sr^{-1}. We note that this is among the lowest estimates of the COB to date that is inferred from γ-ray data alone (see also Ahnen et al., 2016). At the reference wavelength of 1.4μm we find $\lambda I_\lambda = 11.8^{+2.2(5.2)}_{-1.23(2.2)}$ nW $\cdot$ m^{-2}sr^{-1} ($1\sigma(2\sigma)$), limiting any undetected contribution to the cosmic near-IR background to $\lesssim 4$ nW $\cdot$ m^{-2}sr^{-1} (1σ) with respect to integrated counts of Driver et al. (2016), and even less with respect to Keenan et al. (2010). This suggests that larger values of the EBL inferred by direct measurements that rely on absolute flux calibration are not extragalactic and likely attributable to Zodiacal light or other foreground emissions (Matsuura et al., 2017).

An important aspect of this work is the ability to constrain the build-up of the EBL with cosmic time. This is illustrated in Figure 6.4 where we measure that 50% of the COB has been accumulated by $z = 0.9$. The build-up of the EBL across the entire wavelength range is qualitatively consistent with that of state-of-the-art EBL models (Cowley et al., 2018).

The fact that the reconstructed EBL is remarkably similar to integrated counts data, and a host of existing models, suggest that significant systematic biases in our analysis are unlikely. Known systematic uncertainties are already included in the optical depth uncertainties. With nearly ~ 800 blazars, any inaccuracies would need to affect the entire sample systematically in the same manner. Absorption intrinsic to the source (largely ruled out now by Costamante et al., 2018) for instance, from the black hole close environment or host galaxy, would result in the derived EBL being artificially larger, not lower. The fact that our EBL is already close to the minimum allowed by galaxy counts suggests that this effect, if present, is insignificant.

Finally, our work makes use of latest blazar data from *Fermi*-LAT and present Cherenkov telescopes with a maximum energy of 21 TeV and allows us to constrain the EBL up to 70 μm. Long HAWC observations of bright blazars and observations by the upcoming CTA should be able to push this measurement even further, providing better IR constraints. At the same time, CTA should also be able to study the evolution of the EBL

up-to a redshift of 0.5 with 10% uncertainty (Gaté et al., 2017), effectively complementing our results.

Chapter 7

Redshift measurements of AGN

This chapter is taken from Desai et al. (2019b)[1] to report the work done to identify and measure the redshift of unclassified blazar sources in the 3FHL catalog.

7.1 Introduction

Blazars are a peculiar class of active galactic nuclei (AGNs) which dominate the observable γ-ray Universe because of their extreme properties and abundant population. The blazar properties are a result of non-thermal emitting plasma traveling towards the observer causing relativistic amplification of flux. This leads to an amplification of low energy photons in the medium to intense levels via inverse Compton process, making blazars valuable sources to understand the physics of an AGN. The Third *Fermi* –LAT Catalog of High-Energy Sources (3FHL Ajello et al., 2017), which encompasses seven years of observations made by the Large area telescope (LAT) aboard the *Fermi Gamma-ray Space Telescope* (Atwood et al., 2009), contains more than 1500 sources detected at $> 10\,\mathrm{GeV}$, the vast majority of which (≈ 1160) are blazars (Ajello et al., 2017).

Innovative scientific results can be obtained using the blazar data collected by the *Fermi* LAT in the γ-ray regime, provided the redshift (z) of the observed blazar source is

[1] https://doi.org/10.3847/1538-4365/ab01fc

known. These are not only limited to blazar physics such as, understanding their basic emission processes (e.g. Ghisellini et al., 2017) or their evolution with redshift (Ajello et al., 2014), but also to other areas of study, like understanding the extragalactic background light (EBL), which encompasses all the radiation emitted by stars and galaxies and reprocessed radiation from interstellar dust, and its evolution with z (Ackermann et al., 2012a; Domínguez & Prada, 2013b). Out of the confirmed blazar sources reported in the 3FHL catalog a redshift measurement of only $\approx$50 % sources is present (Ajello et al., 2017). To overcome this limitation, extensive optical spectroscopic campaigns, targeting those 3FHL objects still lacking redshift and classification, must be performed.

Besides being used for redshift determination, optical spectroscopy campaigns of blazars are also essential to distinguish between blazar sub-classes, namely BL Lacs (BLL) and flat spectrum radio quasars (FSRQs). FSRQs are generally high redshift objects with average luminosity larger than that of the BLL (Padovani, 1992; Paiano et al., 2017). As a result, the emission lines in the BLL spectra are weak or absent and the lines in FSRQs are extremely prominent. This is seen by the difference in the equivalent width (EW) of the lines where generally, FSRQ have lines with EW$>$ 5Å and BLL have lines with EW$<$ 5 Å(Urry & Padovani, 1995; Ghisellini et al., 2017). The blazar sources not classified as FSRQ or BLL are listed as blazar candidates of uncertain type (BCU) in the 3FHL catalog, and constitute $\approx$ 25 % of the reported blazar sample (Ajello et al., 2017). Obtaining a spectroscopically complete classification of the blazars observed by *Fermi* LAT in the γ-ray regime is essential to validate claims of different cosmological evolution of the two classes (Ajello et al., 2012a, 2014).

The ground based telescopes used in the spectroscopy campaigns are generally of the 4–m,8–m and 10–m class type. While the 10–m and 8–m class telescopes are shown to be significantly more effective in obtaining redshift measurements for blazars (60–80% versus 25–40% success rate, see, e.g. Paiano et al., 2017; Marchesi et al., 2018), even 4–m class telescopes have proven to be useful for effectively distinguishing between the two different blazar subclasses (see Shaw et al., 2013; Massaro et al., 2014; Paggi et al., 2014; Landoni

et al., 2015; Ricci et al., 2015; Marchesini et al., 2016; Álvarez Crespo et al., 2016a,b).

This work is part of a larger spectroscopic follow-up campaign to classify the BCUs in the 3FHL catalog and measure their redshift. The first part of the campaign took place in the second half of 2017, when we observed 28 sources in seven nights of observations at the 4–m telescope at Kitt Peak National Observatory (KPNO). The results of this work are reported in Marchesi et al. (2018): we classified 27 out of 28 sources as BL Lacs, while the remaining object was found to be a FSRQ. Furthermore, we measured a redshift for 3 sources and set a lower limit on z for other four objects; the farthest object in our KPNO sample has $z > 0.836$. The spectroscopic campaign will then continue with seven nights of observations at the 4–m telescope at Cerro Tololo Interamerican Observatory (CTIO) in Chile and five nights of observations at the 8–m Gemini-N and Gemini-S telescopes (to be performed in 2019). In this work, we report the results of the observations made during the first four nights at CTIO. Our source sample contains 23 BCUs in the 3FHL catalog without a redshift measurement. The paper is organized as follows: Section 7.2 reports the criteria used in sample selection, Section 7.3 describes the methodology used for the source observation and spectral extraction procedures, Section 7.4 lists the results of this work, both, for each individual source and also in general terms, while Section 7.5 reports the conclusions inferred from this spectroscopic campaign.

7.2 Sample Selection

We selected the 23 objects in our sample among the BCUs in the 3FHL catalog, using the following three criteria.

- **The object should have an measured optical magnitude measurement**, and it should be V$\leq$19.5. Based on previous works, sources with magnitude V$>$19.5 require more than two hours of observations to obtain an acceptable signal-to-noise ratio (S/N), therefore significantly reducing the number of sources that one can observe in a night.

- The 3FHL source should be bright in the hard γ-ray spectral regime ($f_{50-150\mathrm{GeV}} > 10^{-12}$ erg s^{-1} cm^{-2}). Selecting 3FHL objects bright in the 50–150 GeV band ensures that the completeness of the 3FHL catalog evolves to lower fluxes as more optical observations are performed.

- The target should be observable from Cerro Tololo with an altitude above the horizon $\delta > 40\,^{\circ}$(i.e., with airmass <1.5): this corresponds to a declination range -80°<Dec<20°. The target should also be observable in October, when the observations take place (i.e., it should have R.A.≥09h0m00s and R.A.≤0h30m00s).

A total of 77 3FHL sources satisfy all these criteria. Our 23 sources were selected among these 77 objects with the goal of covering a wide range of optical magnitudes (V=[16–19.5]) and, consequently, of potential redshifts and luminosities. In Figure 7.1 we show the normalized V-band magnitude distribution of our sources, compared with the one of the overall population of 173 3FHL BCUs still lacking a redshift measurement and having available magnitude information. We also plot the magnitude distribution of the 28 sources studied in Marchesi et al. (2018), where we sampled a larger number of bright sources (V<16) which all turned out to be featureless BL Lacs. The sources used in our sample and their properties are listed in Table 7.1.

7.3 Observations and Data Analysis

All the sources in our sample were observed using the $4\,m$ Blanco telescope located at the Cerro Tololo Inter-American Observatory (CTIO) in Chile. The spectra were obtained using the COSMOS spectrograph with the Red grism and the $0.9''$ slit. This experimental setup corresponds to a dispersion of $\sim 4\,$Å pixel^{-1}, over a wavelength range λ=[5000–8000] Å, and a spectral resolution R∼2100. The data were taken with the slit aligned along the parallactic angle. The seeing was $1.3''$ during the first and third night, $1''$ during the second night and $2.2''$ in the last night, respectively; all four nights were photometric.

All spectra reported here are obtained by combining at least three individual observa-

tions of the source with varying exposure times. This allows us to reduce both instrumental effects and cosmic ray contribution. The data reduction is done following a standard procedure: the final spectra are all bias-subtracted, flat-normalized and corrected for bad pixels. We normalize the flat-field to remove any wavelength dependent variations that could be present in the flat-field source but not in the observed spectrum. This is done by fitting a cubic spline function on the calibration spectrum and taking a ratio of the flat-field to the derived fit (see response function in Massey, 1997). We choose an order >5 for the cubic spline function fit with a χ^2 value less than 1 to account for all variable features in the flat-field An additional visual inspection is also done on the combined spectra to remove any artificial features that may still be present. This data reduction and spectral extraction is done using the IRAF pipeline (Tody, 1986).

The wavelength calibration for each source is done using the Hg-Ne lamp: we took a lamp spectrum after each observation of a source, to avoid potential shifts in the pixel-λ calibration due to changes in the telescope position during the night. Finally, all spectra were flux-calibrated using a spectroscopic standard, which were observed using the same $0.9''$ slit used in the rest of the analysis, and then corrected for the Galactic reddening using the extinction law by Cardelli et al. (1989) and the $E(B-V)$ value based on the Schlafly & Finkbeiner (2011) measurements, as reported in the NASA/IPAC Infrared Science Archive.[2]

7.4 Spectral Analysis

To visually enhance the spectral features of our sources, in Figure 7.2 we report the normalized spectra of the objects in our sample. These normalized spectra are obtained by dividing the flux-calibrated spectra using a continuum fit (an approach similar to the one reported in Landoni et al., 2018). The continuum is taken to be a power-law unless the optical shape is more complex, in which case the preferred fit is described in 7.4.1. The S/N of the normalized spectrum is then measured in a minimum of five individual featureless regions in the spectrum with a width of $\Delta\lambda \approx 40$ Å. The spectral analysis results for each

[2] `http://irsa.ipac.caltech.edu/applications/DUST/`

source, including the computed S/N, are reported in Table 7.2.

To find a redshift measurement, each spectrum was visually inspected for any absorption or emission feature. Any potential feature that matched known atmospheric lines[3] was not taken into consideration. To test the reliability of any potential feature, its existence was verified in each of the individual spectral files used to obtain the final combined spectrum shown in Fig 7.2. For example, the broad emission feature seen in the spectrum of 3FHL J0935.2-1735 around 5633 Å is not found in the individual files and is thus considered to be an artifact. The verified features are then matched with common blazar lines, such as the Mg II doublet lines (2797 Å and 2803 Å) or O III line (5007 Å), to compute the redshift.

All the sources in our sample were classified as BLL based on their spectral properties. Out of the 23 sources, we were able to determine a redshift measurement for 3 sources, a lower limit on the redshift for 2 of them and a tentative redshift measurement for 3 of them. The remaining 15 sources in our sample were found to be featureless. Details for some of the sources for which a spectral feature or redshift is found are given in Sec 7.4.1. These features are also listed in Table 7.2 with the derived redshift measurement.

7.4.1 Comments on Individual sources

3FHL J0936.4-2109: This BCU is associated with the X-ray source 1RXS J093622.9-211031. The optical spectrum of this source shows the presence of two absorption features at 6176 Å and 6160 Å. If they are associated with the Mg II doublet, a redshift measurement of 1.1974 and 1.1976 is obtained respectively. Corresponding to this z value, other typical features observed in blazars, either in emission or in absorption (e.g., the Ca II doublet, the G-band, O II or O III features) will fall out of our observed wavelength range of 5000Å−8200Å. We report a tentative lower limit of the redshift as $z > 1.197$ for this BLL.

3FHL J1030.6-2029: This source is associated with the radio source NVSS J103040-203032. Its optical spectrum shows the presence of the Mg II doublet at 5579 Å and 5591 Å respectively. This gives a redshift lower limit of $z > 0.995$.

[3] `https://www2.keck.hawaii.edu/inst/common/makeewww/Atmosphere/atmabs.txt`

3FHL J1042.8+0055: This source is associated with the X-ray source RBS 0895. A redshift value of 0.73 exists in the literature, (Boyle et al., 1990), however the authors flagged it as an uncertain measurement. We were not able to detect any absorption or emission lines in our optical spectrum, so we classify this source as a BLL.

3FHL J1155.5-3418: This source is associated with the radio source NVSS J115520-341718. The Mg II doublet is identified in the optical spectrum of the source at 5174 Å and 5185 Å allowing us to measure the lower limit of the redshift as $z > 0.849$.

3FHL J1212.1-2328: This source is associated with the radio source PMN J1212-2327. We obtain an optical spectrum with S/N of 102.8 and detect an emission feature at 8345 Å with an equivalent width of 0.8 Å. If associated to the O III line, we derive a redshift z=0.666.

3FHL J1223.5-3033: This source is associated with the radio source NVSS J122337-303246. We see possible absorption features at 5245 Å, 5256 Å, 5577 Å and 6341 Å. If 5245 Å and 5256 Å absorption features are associated with the Mg II line, a redshift of 0.875 is measured. However we were not able to detect the presence of any other features and also identify the features at 5577 Å and 6341 Å to confirm the redshift measurement with certainty. This source is thus classified as a BLL and a tentative lower limit of z>0.875 is reported.

3FHL J1433.5-7304: This source is associated with the X-ray source 1RXS J143343.2-730433. One emission feature (H_α) and four absorption features (G-band, Mg I,Na and Ca+Fe) are detected in the spectrum. This gives us a redshift measurement of $z = 0.200$.

3FHL J1439.4-2524: This source is associated with the radio source NVSS J143934-252458. We detect two strong absorption lines at 6008 Å and 6115 Å and an absorption line at 6835 Å close to an atmospheric feature (6845 Å) in its optical spectrum. If these lines are associated with the Mg I, Ca+Fe and NaD absorption features respectively, a redshift of $z = 0.16$ is derived.

3FHL J1605.0-1140: The IR counterpart of this source is WISE J160517.53-113926.8. The optical spectrum shows the presence of an emission feature at 6801 Å with

equivalent width of 7.044 Å. This feature can be associated with the O II or O III line giving a redshift of 0.824 or 0.358 respectively, however due to no significant detection of any other emission or absorption features and a low S/N measurement, the redshift of this source cannot be measured with certainty.

7.5 Conclusion

In this work, we present the results the optical spectroscopic campaign directed towards rendering the 3FHL a spectroscopically complete sample using the COSMOS spectrograph mounted on the $4\,m$ Blanco telescope at CTIO in Chile. We observed 23 extragalactic sources classified as BCU (blazars of uncertain classification) in the 3FHL catalog.

All the objects in our source sample are classified as BLL based on their observed optical spectrum. In the 3FHL catalog, out of the already classified 901 blazars $\approx 84.1\%$ sources are classified as BLL. Moreover out of the 28 sources observed by Marchesi et al. (2018), 27 are identified as BLL denoting that our results are not surprising.

Out of the 23 BLL in our sample we find a reliable redshift measurement for 3 sources, a reliable redshift constraint for 2 sources, a tentative redshift constraint for 3 sources and a featureless spectrum with no redshift measurement for the remaining 15 sources. Combining our results with the results of Marchesi et al. (2018), our optical spectroscopic campaign reports a redshift measurement for $\approx 23.5\%$ of the observed BLL sources using $4\,m$ telescopes. This measurement is in line with the expected consistency of $10-35\%$, obtained for redshift determination of pure BLL using using $4\,m$ telescopes (Landoni et al., 2015; Ricci et al., 2015; Álvarez Crespo et al., 2016a; Peña-Herazo et al., 2017). Moreover, our work combined with Marchesi et al. (2018) also classifies, as either BLL or FSRQs, 51 blazars of previously uncertain classification.

The third and fourth part of our spectroscopic campaign will include observations from the $4\,m$ CTIO telescope and $8\,m$ Gemini-N and Gemini-S telescope respectively[4]. Ad-

[4] *Fermi* Guest Investigator Program Cycle 11, ID:111128, PI: S. Marchesi.

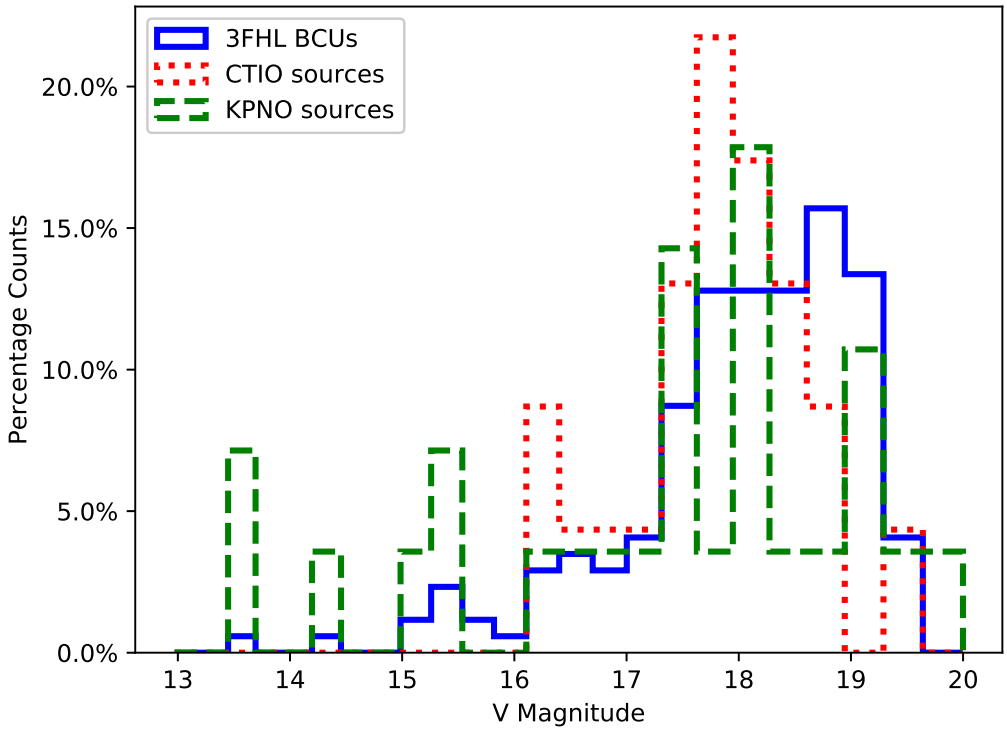

Figure 7.1 Normalized V-band magnitude distribution of the sources analyzed in this work (red dashed line), compared with the distribution of the 173 3FHL BCUs lacking of redshift and having magnitude information (blue solid line). The magnitude distribution of the objects analyzed in Marchesi et al. (2018) using KPNO is also shown for comparison.

ditionally we also aim to extend the campaign by inducing follow up observations[5], similar to Kaur et al. (2019), using the Swift X-ray telescope. These follow up observations in the X-ray regime will help us confirm the classification of the blazar sources contributing to the spectral completion of the 3FHL catalog.

[5] *Swift* Cycle 14, prop ID 1417063 PI: M. Ajello

3FHL Name	Counterpart	R.A.	Dec	E(B-V)	mag	Obs Date	Exposure	continuum slope
(1)	(2)	(3)	(4)	(5)	(6)	(7)	(8)	(9)
3FHL J0002.1−6728	SUMSS J000215−672653	00:02:15.21	−67:26:52.91	0.0253	18.6	June 1 2018	5400	−1.44
3FHL J0935.2−1735	NVSS J093514−173658	09:35:14.77	−17:36:58.30	0.0643	17.8	June 1 2018	3900	−0.12
3FHL J0936.4−2109	1RXS J093622.9−211031	09:36:23.08	−21:10:39.00	0.0574	18.5	June 2,3 2018	5100	−0.28
3FHL J1030.6−2029	NVSS J103040−203032	10:30:40.46	−20:30:32.70	0.0469	18.4	June 3 2018	3300	−1.91
3FHL J1042.8+0055	RBS 895	10:43:03.84	+00:54:20.43	0.0419	19.3	June 4 2018	5600	-1.03
3FHL J1130.5−7801	SUMSS J113032−780105	11:30:32.92	−78:01:05.20	0.1921	17.6	June 2 2018	3400	−1.07
3FHL J1155.5−3418	NVSS J115520−341718	11:55:20.43	−34:17:18.30	0.0702	16.8	June 1 2018	2400	−1.10
3FHL J1212.1−2328	PMN J1212−2327	12:12:04.54	−23:27:42.00	0.0656	18.2	June 1 2018	4500	−0.77
3FHL J1223.5−3033	NVSS J122337−303246	12:23:37.32	−30:32:46.10	0.0593	17.2	June 2 2018	3400	−2.15
3FHL J1229.7−5304	AT20G J122939−530332	12:29:39.93	−53:03:32.20	0.1293	17.8	June 3 2018	2300	−0.44
3FHL J1315.9−0732	WISE J131552.98−073301.9	13:15:53.00	−07:33:02.07	0.0352	18.2	June 4 2018	4500	−0.87
3FHL J1433.5−7304	GALEX J143343.0−730437	14:33:42.81	−73:04:36.84	0.1592	17.9	June 1 2018	4000	−0.81
3FHL J1439.4−2524	NVSS J143934−252458	14:39:34.66	−25:24:59.10	0.0862	16.2	June 3 2018	2800	−0.01
3FHL J1605.0−1140	WISE J160517.53−113926.8	16:05:17.53	−11:39:26.83	0.2584	18.7	June 4 2018	5400	−0.35
3FHL J1612.3−3100	NVSS J161219−305937	16:12:19.95	−30:59:37.80	0.2003	18.1	June 2 2018	3600	−1.11
3FHL J1640.1+0629	NVSS J164011+062827	16:40:11.06	+06:28:27.70	0.0695	18.6	June 2 2018	3800	−1.71
3FHL J1842.4−5841	1RXSJ184230.6−584202	18:42:29.67	−58:41:57.19	0.0848	17.5	June 1 2018	3600	−1.67
3FHL J1924.2−1548	NVSS J192411−154902	19:24:11.82	−15:49:02.10	0.1491	17.7	June 3 2018	3600	−1.35
3FHL J2034.9−4200	SUMSS J203451−420024	20:34:51.06	−42:00:37.60	0.0360	17.2	June 2,4 2018	3900	−0.62
3FHL J2041.7−7319	SUMSS J204201−731911	20:42:01.85	−73:19:13.01	0.0544	18.2	June 4 2018	3400	−4.47
3FHL J2240.3−5240	SUMSS J224017−524111	22:40:17.64	−52:41:13.07	0.0118	16.7	June 4 2018	1950	−5.84
3FHL J2321.8−6437	PMN J2321−6438	23:21:42.17	−64:38:06.90	0.02	17.4	June 4 2018	2800	−0.06
3FHL J2339.2−7404	1RXS J233919.8−740439	23:39:20.88	−74:04:36.12	0.0262	16.1	June 4 2018	1500	−0.65

Table 7.1 List of sources and their properties sorted in the order of increasing R.A. (Right ascension) values. (1): 3FHL catalog (Ajello et al., 2017) name for the source. (2): optical, IR, X-ray or radio counterpart of the source. (3) Right ascension. (4) Declination. (5) $E(B-V)$ value obtained using the measurements of Schlafly & Finkbeiner (2011) and the NASA/IPAC Infrared Science Archive online tool. (6) V band magnitude. (7) Date of observation. (8) Exposure time (in seconds).(9)Slope of continuum fit obtained from the observed fits file

Source	S/N	Spectral line	Observed λ (Å)	line type	redshift
		Rest frame λ (Å)			
3FHL J0002.1−6728	41.4				
3FHL J0935.2−1735	51.5				
3FHL J0936.4−2109	27.2	Mg II(2797)	6176	absorption	$> 1.197^*$
		Mg II(2803)	6160	absorption	
3FHL J1030.6−2029	29.3	Mg II(2797)	5579	absorption	> 0.995
		Mg II(2803)	5591	absorption	
3FHL J1042.8+0055	46.6				
3FHL J1130.5−7801	72.2				
3FHL J1155.5−3418	42.7	Mg II(2797)	5174	absorption	> 0.849
		Mg II(2803)	5185	absorption	
3FHL J1212.1−2328	102.8	O III(5007)	8345	emission	0.666
3FHL J1223.5−3033	46.5	Mg II(2797)	5245	absorption	$> 0.875^*$
		Mg II(2803)	5256	absorption	
3FHL J1229.7−5304	78.6				
3FHL J1315.9−0732	60.8				
3FHL J1433.5−7304	64.9	G-band(4304)	5165	absorption	0.200
		Mg I(5175)	6209	absorption	
		Ca+Fe(5269)	6340	absorption	
		Na (5895)	7074	absorption	
		H_α(6562)	7876	absorption	
3FHL J1439.4−2524	82.7	Mg I(5175)	6008	absorption	0.16
		Ca+Fe(5269)	6115	absorption	
		NaD(5892)	6835	absorption	
3FHL J1605.0−1140	17.2	O II(3727)	6801	emission	0.358^*
		(or) O III(5007)	6801	emission	0.824^*
3FHL J1612.3−3100	75.4				
3FHL J1640.1+0629	83.1				
3FHL J1842.4−5841	32.7				
3FHL J1924.2−1548	64.4				
3FHL J2034.9−4200	33.4				
3FHL J2041.7−7319	70.1				
3FHL J2240.3−5240	71.2				
3FHL J2321.8−6437	33.7				
3FHL J2339.2−7404	45.5				

Table 7.2 Results obtained from spectral analysis discussed in Section 7.4. The redshift measurement values marked with a * are tentative z measurements.

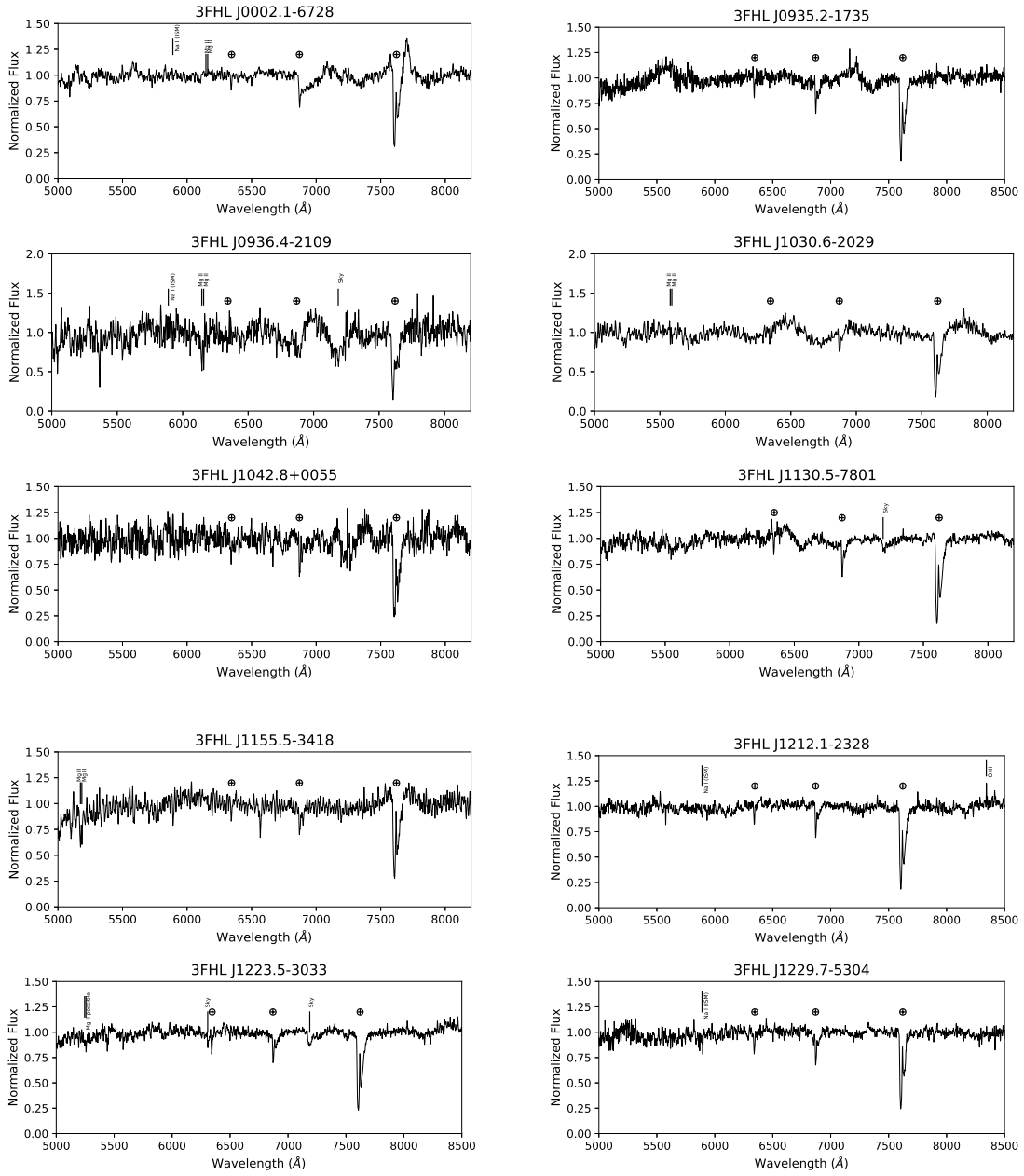

Figure 7.2 Optical spectra of the observed candidates after performing flux calibration and dereddening. The bottom panel displays the normalized spectra where the atmospheric features are denoted by ⊗ while the absorption or emission features are labeled as per the lines they signify.

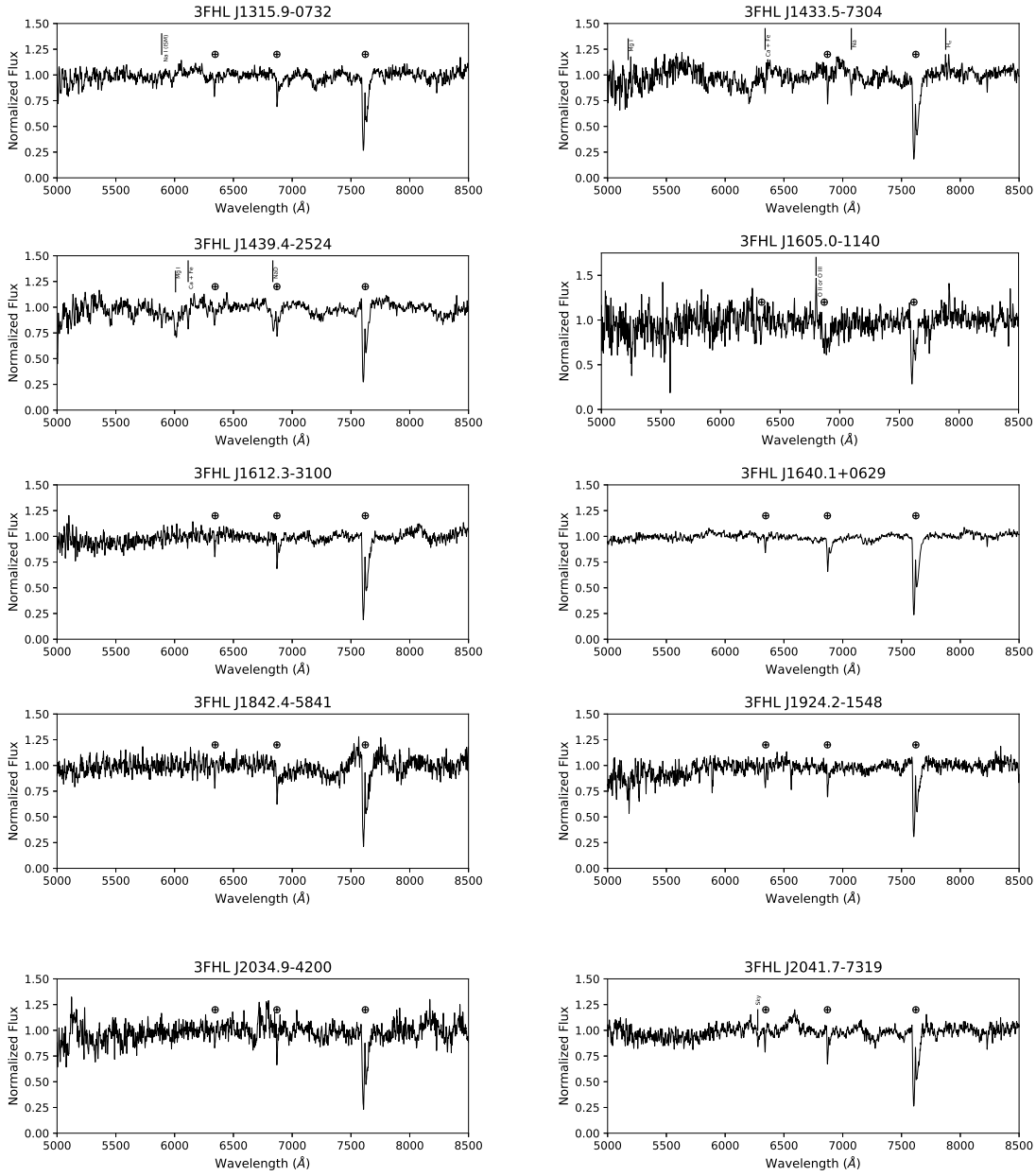

Figure 7.2 Continued from Fig 7.2

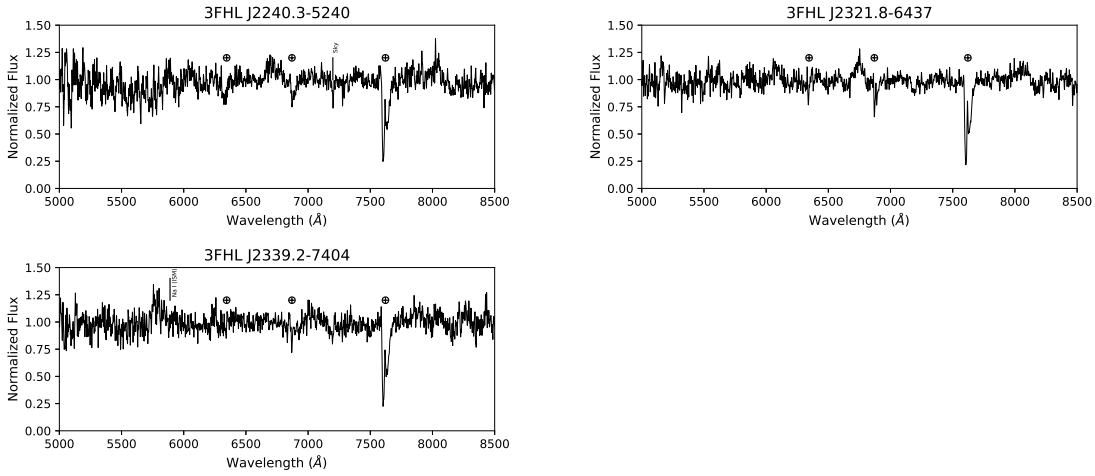

Figure 7.2 Continued from Fig 7.2

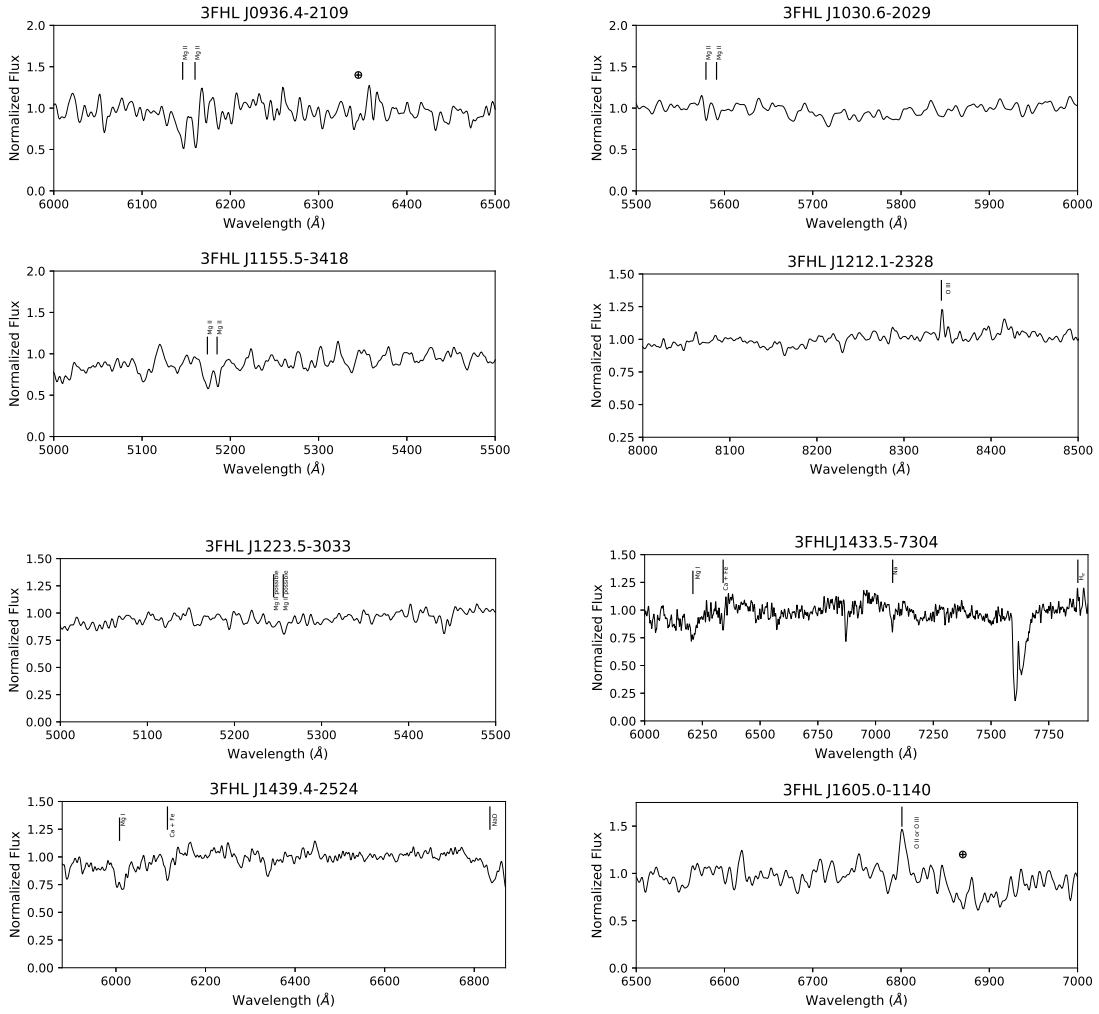

Figure 7.3 The zoomed spectra of selected sources from Fig 7.2 are shown above to highlight absorption and emission features

Chapter 8

Conclusions and Discussion

As the EBL is the collections of all the light radiated over the history of the Universe, a thorough understanding about its energy density and how it evolved with time has the potential to unlock many mysteries of the Universe. Like we saw in Chapter 2, many efforts have been made to constrain the EBL intensity using galaxy counts, direct methods and indirect methods. We also saw that the most effective method to probe the EBL is by studying the attenuation it leaves in the spectra of distant high energy sources, also known as the indirect method. Multiple studies have been undertaken in the past to study this EBL attenuation (e.g. Ackermann et al., 2012b; Mazin et al., 2017; Abramowski et al., 2013a; Biteau & Williams, 2015) making use of the observed spectrum of GRBs and Blazars in the GeV and TeV regime. However most of the indirect measurement methods aim to scale the estimated EBL optical depth calculated by existing EBL models at a particular redshift and energy using a normalization constant. To tackle this problem and to understand the evolution of the EBL in a much more effective way, our group devised a novel approach to bin the existing observed data in multiple energy and redshift bins (similar to Ackermann et al., 2012b) and measure the EBL optical depth in each of these bins. As we saw in Chapters 4 and 5, this approach allows us to obtain a model independent measurement of the EBL optical depth and the shape of the the optical depth curve as it evolves with redshift.

As we saw in Chapter 4, we used the spectra of 22 GRBs observed using the *Fermi*-LAT in the 100 MeV to 500 GeV energy range and combined it with the results derived by Ackermann et al. (2012b) and our approach to constrain the EBL optical depth up-to a redshift of 4.35. Moreover, we also showed that GRBs can serve to be a valuable diagnostic tool to determine the shape of the EBL optical depth curve as reported by different EBL models. However, due to the limited sample size of GRBs that could be used in the analysis, although effective, there is a scope of improvement by using a larger burst sample with known redshift measurements. This can be achieved using quicker burst alert for ground based telescopes to perform a spectroscopic measurement or making use of effective photometric measurements.

Following the GRB measurement, we saw in Chapters 5 and 6, how our group exceedingly improved upon the measurement of the EBL by making use of not only 759 Blazars observed by the *Fermi*-LAT but also 106 blazar spectra, observed in the TeV regime using Cherenkov Telescopes. Using these measurements and combining it with existing EBL spectral intensity lower-limits reported by IGL data by Driver et al. (2016) allowed us to derive a minimal EBL measurement throughout the UV/optical range with respect to the IGL data. Moreover due to the inclusion of TeV data, we were also able to report the EBL intensity in the IR regime with increased sensitivity as compared to past results.

From all the measurements of the EBL using observed data, the importance of an effective redshift measurement of a blazar or GRB source for EBL attenuation is evident. We saw that one of the primary and most effective ways to determine the redshift of a source is to observe it in the optical electromagnetic regime using ground based telescopes and perform spectroscopy on it (Chapter 7). To contribute to the number of known sources with redshift measurements, we used the 3FGL (Ajello et al., 2017) catalog to check for sources with no known redshift measurement and observed 23 sources using the 4 m class CTIO telescope in Chile. While we were only able to find redshifts of 3 sources, a lower limit for 2 sources and a tentative redshift measurement for 3 more sources which was expected based on the sensitivity of the telescope, similar campaigns in the future will prove to be

extremely useful for EBL measurement.

In Chapter 5, we also briefly mentioned the results derived from the The Fermi-LAT Collaboration (2018) project. The key highlight of this project was the measurement of the star formation rate density over 90% of cosmic time. This measurement was in agreement with the existing UV and Layman Break Galaxy (LBG) surveys peaking at a redshift of $z = 2$. Moreover, using the measurements of GRB080916C from Desai et al. (2017) and extrapolation techniques we were able to present a star formation history measurement upto a redshift of 6 (see Figure 5.3).

The EBL intensity once properly constrained can be also used in the field of cosmology to determine key scientific results like measurement of the Hubble constant and matter density (Domínguez & Prada, 2013b; Biteau & Williams, 2015). Using the updated EBL intensity measurements in this work, Domínguez et al. (2019) reported a new measurement of the Hubble constant $H_0 = 67.5^{+1.4}_{1.5}$ km Mpc^1 s^1 and matter density parameter $\Omega_m = 0.30 \pm 0.02$. Domínguez et al. (2019) make use of two methods to measure the cosmological parameters: 1. Using only γ ray attenuation data(found using th optical depth bins shown in Chapters 5 and 6 and 2. Using a combination of BAO(baryon acoustic oscillations) + BBN (Big Bang nucleosynthesis) + SN (supernova) + γ ray data. These measurements compared with measurements from other methods is shown in Figure 8.1. This reported measurement, as can be seen from the figure, has contours roughly orthogonal to the contours displayed from other methods making it complementary to the other results. A measurement of the EBL optical depth at higher energies made this measurement possible, which signifies, the importance of the work shown in Chapter 6 and the importance of TeV observations from the upcoming CTA.

The combination of all the EBL measurements reported in work along with the valuable measurements of the comic star formation history, Hubble constant and matter density, we have been able to unveil the cosmic history of light from the viewpoint of high energy astrophysics. In the future, upcoming telescopes like JWST and CTA will be able to provide with an updated EBL measurement using direct and indirect methods respectively.

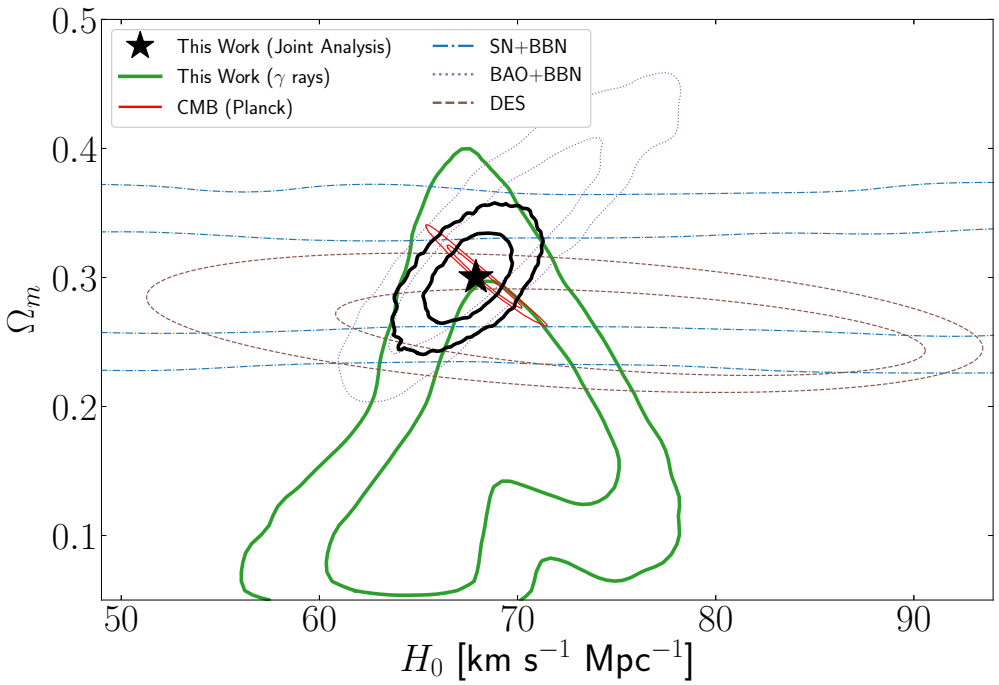

Figure 8.1 Measurement of the Hubble constant and matter density using EBL attenuation measurements with 1σ and 2σ contours (green). The maximum likelihood value for this work (black star). Different methods used to measure the $H_0 and \Omega_m$ are: supernovae plus Big Bang Nucleosynthesis (SN+BBN, blue), baryonic acoustic oscillations plus Big Bang nucleosynthesis (BAO+BBN, purple), clustering and weak lensing data (DES, brown), the cosmic mi- crowave background (Planck, red) and a joint likelihood of BAO+BBN+SN+ (black). Figure and caption taken from Domínguez et al. (2019).

However, as both these missions are in production stage it will take about two to three years before data collection. In the meantime, the results presented in this work can serve as an updated view of the EBL and be used to probe prime areas of astrophysics like stellar evolution and galaxy evolution.

Appendices

Appendix A Abbreviations used

- AGN: Active Galactic Nuclei
- ARCADE 2: Absolute Radiometer for Cosmology, Astrophsyics, and Diffuse Emission 2
- BAO: Baryon Acoustic Oscillations
- BAT: Burst Allen Telescope
- BBN: Big Bang nucleosynthesis
- BCU: Blazar Candidates of Uncertain type
- BLLAC: BL Lacertae (blazar subclass)
- CGB: Cosmic Gamma-ray Background
- CIBER: Cosmic Infrared Background ExpeRiment
- CMB: Cosmic Microwave Background
- COBE: Cosmic Background Explorer
- CRB: Cosmic Radio Background
- CTA: Cherenkov Telescope Array
- CTIO: Cerro Tololo Interamerican Observatory
- CXB: Cosmic X-ray Background
- DIRBE: Diffuse Infrared Background Experiment
- EBL: Extragalactic Background Light
- EGRET: Energetic Gamma Ray Experiment Telescope
- FIRAS: Far Infrared Absolute Spectrophotometer

- FSRQ: Flat Spectrum Radio Quasars (blazar subclass)
- GALEX: Galaxy Evolution Explorer
- GEB: Gamma-ray Burst Monitor
- GLAST: Gamma-Ray Large Area Space Telescope
- GRB: Gamma Ray Burst
- HEAO1: High Energy Astrophysics Observatory-1
- HEP: Highest Energy Photon
- HESS: High Energy Stereoscopic System
- HFF: Hubble Frontier Fields
- HST: Hubble Space Telescope
- IMF: Initial Mass Function
- IR: Infrared
- IRAS: Infrared Astronomical Satellite
- JWST: James Webb Space Telescope
- KPNO: Kitt Peak National Observatory
- LAT: Large Area Telescope
- LBG: Lyman Break Galaxy
- LL: Log Likelihood
- MAGIC: Major Atmospheric Gamma Imaging Cherenkov Telescopes
- MCMC: Markov Chain Monte Carlo

- MIPS: Multiband Imaging Photometer
- NASA: National Aeronautics and Space Administration
- NSST: National Space Science and Technology Center
- PACS: Photodetector array camera and spectrometer
- SAA: South Atlantic Anomaly
- SAS-2: Small Astronomy Satellite 2
- SED: Spectral Energy Distributions
- SFH: Star Formation History
- SN: Supernova
- SPIRE: Spectral and Photometric Imaging Receiver
- STIS: Space Telescope Imaging Spectrograph
- TS: Test Statistics
- UV: Ultraviolet
- UVS: Ultraviolet Imaging Spectrometer
- VERITAS: Very Energetic Radiation Imaging Telescope Array System
- WIMP: Weakly Interacting Massive Particle
- WMAP: Wilkinson Microwave Anisotropy Probe

Appendix B EBL attenuation brief overview

The following appendix section is a review of the EBL attenuation based on the results reported by Dwek & Krennrich (2013). When two photons with energies E_γ and E_b interact with each other, a electron positron pair creation will take place via pair production if the total energy of the photons in the center of momentum exceeds the rest frame energy of the two particles, in this case e^+ and e^-. The threshold energy required can then be found out by:

$$E_b^{threshold}(E_\gamma, z, \mu)) = \frac{2(m_e c^2)^2}{E_\gamma(1-\mu)}) \tag{1}$$

where $\mu = \cos\theta$ and θ is the interaction angle of the two photons.

The cross section of the pair production interaction can be found by making use of the relation between the threshold energy and the energy of the incoming gamma ray photon.

$$\sigma_{\gamma\gamma}(E_\gamma, z, \mu, \epsilon) = \frac{3\sigma_T}{16}(1-\beta^2)\left[2\beta(\beta^2-2) + (3-\beta^4)\ln\left(\frac{1+\beta}{1-\beta}\right)\right] \tag{2}$$

where

$$\beta = \sqrt{\left(1 - \frac{E_b^{threshold}}{\epsilon}\right)} \tag{3}$$

An analysis similar to Dwek & Krennrich (2013) can easily show that β peaks at a value of 0.7 (see Figure 1) allowing us to find the energy of an incoming gamma ray photon with respect to the energy of the interacting EBL photon. This is given by:

$$E_\gamma = \frac{1.07}{\epsilon_{EBL}(1-\mu)} \tag{4}$$

Photons emitted from distant gamma ray sources pass through the EBL radiation field and are annihilated depending upon their energies due to the pair production described above. The EBL optical depth can be found as a function of the photon energy and redshift

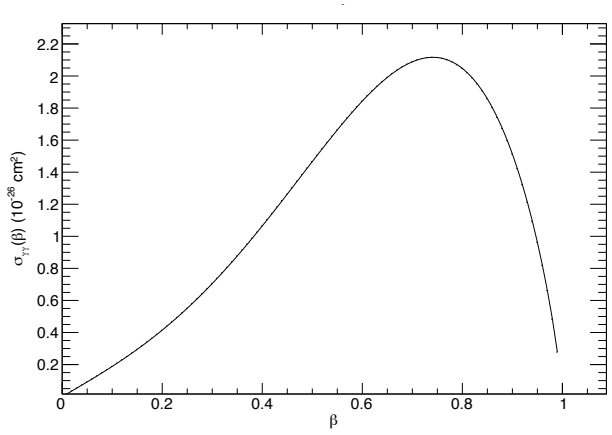

Figure 1 Above plot depicts $\sigma_{\gamma\gamma}$ as a function of increasing β.

provided we know the number density of the EBL photons and the cross section of pair production seen in equation 2 along with the cosmological parameters (see Appendix C). The EBL optical depth can thus be given by:

$$\tau_{\gamma\gamma}(E_\gamma, z) = \int_0^z dz' \frac{dl}{dz'} \int_{-1}^{1} d\mu \frac{1-\mu}{2} \int_{E_b^{threshold}}^{\infty} d\epsilon n_\epsilon(\epsilon, z')(1+z')^3 \sigma_{\gamma\gamma}(\beta', z') \qquad (5)$$

where the comoving EBL photon number density is given by $n_\epsilon(\epsilon, z')$ in units of $\mathrm{cm}^{-3}\mathrm{eV}^{-1}$ and can be found from the EBL intensity of at a given redshift. The term $(1+z')^3$ in the equation is added to convert the comoving density to the proper frame of reference. As seen from the above equation, to understand the evolution of the EBL opacity and to model the the effect it has on an incoming photon, it is required to model the EBL intensity.

For this exercise, the intensity is modeled as a diluted blackbody for simplicity(see Figure 2). Using this modeled intensity, we find the EBL photon number density shown in Figure 3.

The modeled EBL opacity is shown in Figure 4. The redshift taken for the exercise is $z = 0.5$ and a non evolving EBL is considered for simplicity.

Once we have the modeled EBL opacity, we can find the effect it has on an incoming

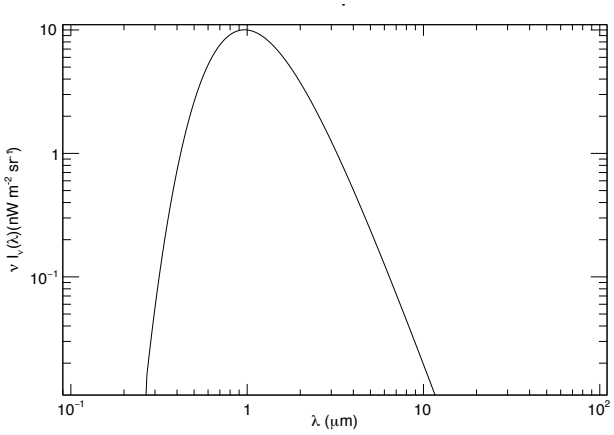

Figure 2 Intensity of the optical component of the EBL modeled using a diluted blacbody function.

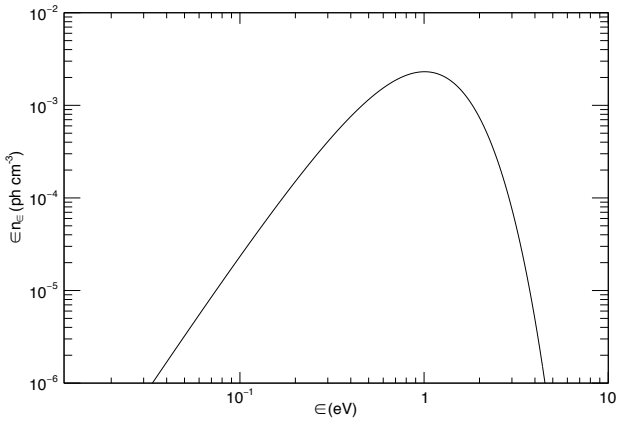

Figure 3 Photon density of the EBL in the optical regime, modeled using the EBL intensity shown in Figure 2.

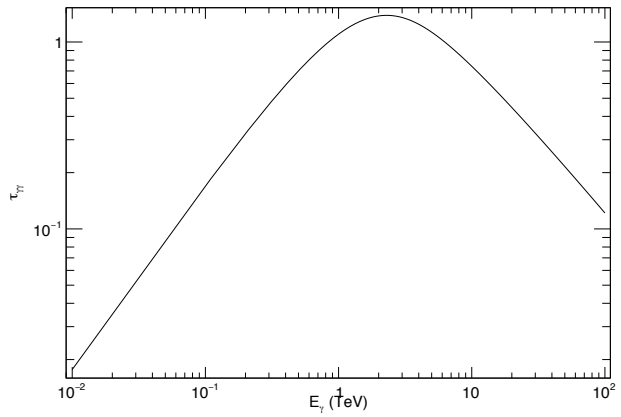

Figure 4 Optical depth of the EBL computed using the modeled intensity and number density.

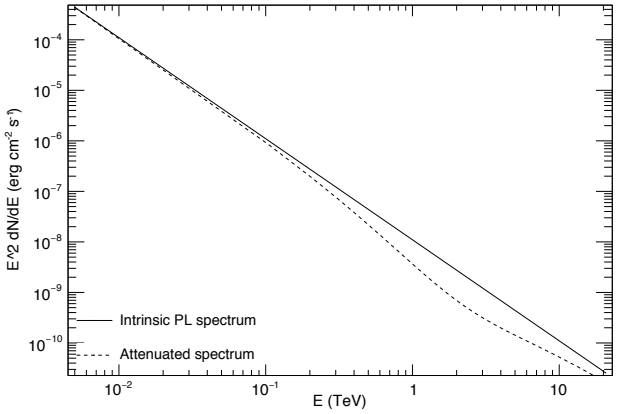

Figure 5 Comparison of an attenuated and unattenuated gamma ray spectrum. The unattenuated spectrum is modeled using a simple Power Law.

beam of gamma ray photons. This can be shown easily by taking the intrinsic source spectrum of the gamma ray photons as a simple power law with an index of -2.0. Using Equation 2.4, we can see the dip in the power law spectrum with increasing energy. The comparison between the unattenuated and attenuated spectrum is shown in Figure 5

As we only model the optical component of the EBL in this exercise, the optical EBL depth decreases at higher energies. If the double hump structure of the EBL intensity were used (after including luminosity due to dust), an increasing optical depth curve would be seen. THe shape of the optical depth curve would follow the EBL intensity where at the peak intensities the slope of the curve will be steeper as opposed to the optical depth corresponding to lower intensity values.

Appendix C Cosmology concepts used in this work

It is has been known for more than ∼90 years now that the universe is expanding. This expansion can be described simply by the Hubble's law formulated using evidence of observed redshifts of distant galaxies that are moving away from us. It also mentions that every galaxy in the universe is moving away from every other galaxy (unless the galaxies are gravitationally bound) proving that the universe as a whole is expanding. The rate of expansion is denoted in units of km/s/Mpc by the Hubble parameter H, defined as the ratio of the recessional velocity of a source to its redshift. However the rate of expansion of the universe has been found to be accelerating, which can be parameterized by a scaling factor a. This would mean that the value of H would also change with time and can be found using:

$$H = \frac{\dot{a}}{a} \tag{6}$$

This equation can be expanded by using the Friedmann equation which takes into account the curvature of the universe and the total energy density of the universe. These studies of expansion rate has shown that the density of the universe at which it will continue to expand forever, dubbed as the critical density, is very close to the current energy density. The ratio of the density and the critical density is dubbed as the density parameter Ω where an $\Omega = 1$ would indicate critical density. The total density parameter of the universe is a sum of 4 different density parameters. These are denoted as follows: matter : Ω_m, radiation: Ω_R, curvature: Ω_k and cosmological constant Λ: Ω_Λ. The Hubble parameter can then be written as:

$$H(a) = H_0\sqrt{\Omega_k a^{-2} + \Omega_m a^{-3} + \Omega_R a^{-4} + \Omega_\Lambda} \tag{7}$$

where H_0 is the current value of the Hubble parameter also known as the "Hubble constant". Following the current standard cosmological model, also known as the ΛCDM model (see Planck, Ade et al., 2015) our universe consists of three major components: dark

energy, cold dark matter and ordinary matter. The universe is considered to be flat meaning $\Omega_k 0$ and observations of the radiation density parameter show that it is very small (so $\Omega_R \approx 0$). Following this methodology and the relation between a and redshift ($a = (1+z)^{-1}$), the Hubble parameter can then be written as:

$$H = H_0[\Omega_m(1+z)^3 + \Omega_\Lambda] \tag{8}$$

Using this relation between H and z, distances between two objects is calculated. The distance between two objects at a specific moment (given by cosmological time) is dubbed as proper distance. The constant distance between two objects in the Universe which are close to each other not effected by the expansion of the universe is called comoving distance. Depending on the redshift measurement of a source, the comoving distance can be found as:

$$D_C = \frac{c}{H_0}\int_0^z \frac{dz'}{\sqrt{\Omega_m(1+z)^3 + \Omega_\Lambda}} \tag{9}$$

The relationship between the luminosity of an object and the observed Flux is defined as the luminosity distance D_L of the object and is given by:

$$D_L^2 = \frac{L}{4\pi F} \tag{10}$$

The luminosity distance is related to the comoving distance by $D_L = (1+z)D_C$, which would mean that the comoving distance can be found using the luminosity distance equation as:

$$D_C^2 = \frac{L}{4\pi F(1+z)^2} \tag{11}$$

Using Equation 8, we can also calculate look back time, which is termed as the difference in the age of universe when a particular photon was emitted from an object and when it observed (in current time). If the age of the universe now is denoted by t_0 and the age of the universe when the photons were emitted at a redshift z, the look back time is

given as:

$$t_L = \frac{1}{H_0} \int_0^z \frac{dz'}{(1+z')\sqrt{\Omega_m(1+z')^3 + \Omega_\Lambda}} \tag{12}$$

Bibliography

Abdalla, H., Abramowski, A., Aharonian, F., et al. 2017, A&A, 606, A59

Abdo, A., Ackermann, M., Ajello, M., et al. 2009a, ApJL, 706, L138

Abdo, A. A., Ackermann, M., Arimoto, M., et al. 2009b, Science, 323, 1688

Abdollahi, S., Ackermann, M., Ajello, M., et al. 2017, ApJ, 846, 34

Abramowski, A., Acero, F., Aharonian, F., et al. 2012, A&A, 548, A38

—. 2013a, A&A, 550, A4

—. 2013b, A&A, 550, A4

Abramowski, A., Acero, F., Aharonian, F., et al. 2013, A&A, 550, A4

Acciari, V. A., et al. 2019, Mon. Not. Roy. Astron. Soc., 486, 4233

Acero, F., Ackermann, M., Ajello, M., et al. 2015, ApJS, 218, 23

—. 2016, ApJS, 223, 26

Acero, F., Ackermann, M., Ajello, M., et al. 2016, ApJS, 223, 26

Ackermann, M., Ajello, M., Asano, K., et al. 2011, The Astrophysical Journal, 729, 114

Ackermann, M., Ajello, M., Allafort, A., et al. 2012a, Science, 338, 1190

—. 2012b, Science, 338, 1190

Ackermann, M., Ajello, M., Albert, A., et al. 2013a, ApJ, 771, 57

Ackermann, M., Ajello, M., Allafort, A., et al. 2013b, ApJS, 209, 34

Ackermann, M., Ajello, M., Asano, K., et al. 2013c, ApJS, 209, 11

—. 2013d, ApJS, 209, 11

Ackermann, M., Ajello, M., Albert, A., et al. 2015a, arXiv:1508.04449, arXiv:1508.04449

Ackermann, M., Ajello, M., Atwood, W., et al. 2015b, ApJ, 810, 14

Ackermann, M., Ajello, M., Atwood, W. B., et al. 2015, ApJ, 810, 14

Actis, M., Agnetta, G., Aharonian, F., et al. 2011, Experimental Astronomy, 32, 193

Adams, F., Freese, K., Laughlin, G., Schwadron, N., & Tarlé, G. 1997, ApJ, 491, 6

Aharonian, F., Akhperjanian, A., Bazer-Bachi, A., et al. 2006, , 440, 1018

Ahnen, M. L., Ansoldi, S., Antonelli, L. A., et al. 2016, arXiv:1602.05239

Ajello, M., Alexander, D., Greiner, J., et al. 2012a, ApJ, 749, 21

Ajello, M., Greiner, J., Sato, G., et al. 2008, ApJ, 689, 666

Ajello, M., Shaw, M. S., Romani, R. W., et al. 2012b, ApJ, 751, 108

Ajello, M., Romani, R., Gasparrini, D., et al. 2014, ApJ, 780, 73

Ajello, M., Gasparrini, D., Sánchez-Conde, M., et al. 2015, ApJL, 800, L27

Ajello, M., Atwood, W., Baldini, L., et al. 2017, ApJS, 232, 18

Ajello, M., Atwood, W. B., Baldini, L., et al. 2017, ApJS, 232, 18

Albert, Albert, J., Aliu, E., et al. 2008, Science, 320, 1752

Álvarez Crespo, N., Masetti, N., Ricci, F., et al. 2016a, , 151, 32

Álvarez Crespo, N., Massaro, F., Milisavljevic, D., et al. 2016b, , 151, 95

Anchordoqui, L. A. 2019, Physics Reports, 801, 1 , ultra-high-energy cosmic rays

Andrews, S. K., Driver, S. P., Davies, L. J. M., Lagos, C. d. P., & Robotham, A. S. G. 2018, MNRAS, 474, 898

Andrews, S. K., Driver, S. P., Davies, L. J. M., et al. 2017, MNRAS, 470, 1342

Armstrong, T., Brown, A. M., & Chadwick, P. M. 2017, MNRAS, 470, 4089

Ashby, M. L. N., Willner, S. P., Fazio, G. G., et al. 2013, ApJ, 769, 80

Atek, H., Richard, J., Kneib, J.-P., & Schaerer, D. 2018, arXiv:1803.09747, arXiv:1803.09747:1803.09747

Atwood, W., Abdo, A., Ackermann, M., et al. 2009, ApJ, 697, 1071

Atwood, W., Baldini, L., Bregeon, J., et al. 2013, ApJ, 774, 76

Band, D., Matteson, J., Ford, L., et al. 1993, ApJ, 413, 281

Beckmann, V., & Shrader, C. 2012, in Proceedings of "An INTEGRAL view of the high-energy sky (the first 10 years)" - 9th INTEGRAL Workshop and celebration of the 10th anniversary of the launch (INTEGRAL 2012). 15-19 October 2012. Bibliotheque Nationale de France, 69

Bernstein, R. 2007, ApJ, 666, 663

Bernstein, R. A., Freedman, W. L., & Madore, B. F. 2002, ApJ, 571, 56

Berta, S., Magnelli, B., Lutz, D., et al. 2010, A&A, 518, L30

Bertone, G., Hooper, D., & Silk, J. 2005, , 405, 279

Béthermin, M., Dole, H., Beelen, A., & Aussel, H. 2010, A&A, 512, A78

Béthermin, M., Le Floc'h, E., Ilbert, O., et al. 2012, A&A, 542, A58

Bhat, P. N., Meegan, C. A., von Kienlin, A., et al. 2016, The Astrophysical Journal Supplement Series, 223, 28

Biteau, J., & Williams, D. 2015, ApJ, 812, 60

Biteau, J., & Williams, D. A. 2015, ApJ, 812, 60

Bond, J., Carr, B., & Hogan, C. 1986, ApJ, 306, 428

Bourne, N., Dunlop, J. S., Merlin, E., et al. 2017, MNRAS, 467, 1360

Bouwens, R., Illingworth, G., Oesch, P., et al. 2015a, ApJ, 803, 34

—. 2015b, ApJ, 803, 34

Bouwens, R. J., Oesch, P. A., Illingworth, G. D., Ellis, R. S., & Stefanon, M. 2017, ApJ, 843, 129

Bouwens, R. J., Illingworth, G. D., Oesch, P. A., et al. 2012, ApJ, 754, 83

—. 2014, ApJ, 793, 115

Bouwens, R. J., Aravena, M., Decarli, R., et al. 2016, ApJ, 833, 72

Boyle, B., Fong, R., Shanks, T., & Peterson, B. 1990, MNRAS, 243, 1

Brown, R. W., Mikaelian, K. O., & Gould, R. J. 1973, , 14, 203

Brown, T. M., Kimble, R. A., Ferguson, H. C., et al. 2000, The Astronomical Journal, 120, 1153

Brun, P. 2013, Journal of Physics: Conference Series, 460, 012015

Burgarella, D., Buat, V., Gruppioni, C., et al. 2013, A&A, 554, A70

Burke, C., Hilton, M., & Collins, C. 2015, MNRAS, 449, 2353

Burns, J. O., Lazio, J., Bale, S., et al. 2012, Advances in Space Research, 49, 433

Cambrésy, L., Reach, W., Beichman, C., & Jarrett, T. 2001, ApJ, 555, 563

Cardelli, J., Clayton, G., & Mathis, J. 1989, ApJ, 345, 245

Chabrier, G. 2003, , 115, 763

Churazov, E., Sunyaev, R., Revnivtsev, M., et al. 2007, A&A, 467, 529

Cole, S., Norberg, P., Baugh, C. M., et al. 2001, MNRAS, 326, 255

Collazzi, A. C., Kouveliotou, C., van der Horst, A. J., et al. 2015, The Astrophysical Journal Supplement Series, 218, 11

Cooray, A. 2016, Royal Society Open Science, 3, doi:10.1098/rsos.150555

Costamante, L., Cutini, S., Tosti, G., Antolini, E., & Tramacere, A. 2018, MNRAS, 477, 4749

Cowley, W. I., Lacey, C. G., Baugh, C. M., et al. 2018, arXiv e-prints, arXiv:1808.05208

CTA Consortium. 2019, Science with the Cherenkov Telescope Array, doi:10.1142/10986

Cucciati, O., Tresse, L., Ilbert, O., et al. 2012a, A&A, 539, A31

—. 2012b, A&A, 539, A31

Dahlen, T., Mobasher, B., Dickinson, M., et al. 2007, ApJ, 654, 172

de Palma, F., Bissaldi, E., Tajima, H., et al. 2009, GRB Coordinates Network, 9872

Desai, A., Helgason, K., Ajello, M., et al. 2019a, ApJL, 874, L7

Desai, A., Marchesi, S., Rajagopal, M., & Ajello, M. 2019b, ApJS, 241, 5

Desai, A., Ajello, M., Omodei, N., et al. 2017, ApJ, 850, 73

Desai, A., Ajello, M., Omodei, N., et al. 2017, ApJ, 850, 73

Di Mauro, M., Calore, F., Donato, F., Ajello, M., & Latronico, L. 2013, ApJ, 780, 161

Dole, H., Lagache, G., Puget, J. L., et al. 2006, A&A, 451, 417

Domínguez, A., & Ajello, M. 2015, ApJL, 813, L34

Domínguez, A., & Ajello, M. 2015, ApJL, 813, L34

Domínguez, A., Finke, J., Prada, F., et al. 2013, ApJ, 770, 77

Domínguez, A., & Prada, F. 2013a, ApJL, 771, L34

—. 2013b, ApJL, 771, L34

Domínguez, A., Primack, J., Rosario, D., et al. 2011, MNRAS, 410, 2556

Domínguez, A., Wojtak, R., Finke, J., et al. 2019, arXiv e-prints, arXiv:1903.12097

Driver, S., Andrews, S., Davies, L., et al. 2016, ApJ, 827, 108

Driver, S. P., Popescu, C. C., Tuffs, R. J., et al. 2008, ApJL, 678, L101

Driver, S. P., Andrews, S. K., da Cunha, E., et al. 2018, MNRAS, 475, 2891

Dwek, E. 2014, in American Astronomical Society Meeting Abstracts, Vol. 224, American Astronomical Society Meeting Abstracts #224, 401.01

Dwek, E., Arendt, R., & Krennrich, F. 2005, ApJ, 635, 784

Dwek, E., & Krennrich, F. 2013, AstropARTICLE Physics, 43, 112

E. Roach, F., & L. Smith, L. 1968, Geophys. J. R. Astron. Soc., 15, doi:10.1111/j.1365-246X.1968.tb05760.x

Edelstein, J., Bowyer, S., & Lampton, M. 2000, ApJ, 539, 187

Eggleton, P. P., Fitchett, M. J., & Tout, C. A. 1989, ApJ, 347, 998

Ellis, R. S., McLure, R. J., Dunlop, J. S., et al. 2013, ApJL, 763, L7

Essey, W., Ando, S., & Kusenko, A. 2011, AstropARTICLE Physics, 35, 135

Essey, W., & Kusenko, A. 2010, AstropARTICLE Physics, 33, 81

Fazio, G., & Stecker, F. 1970, , 226, 135

Fazio, G., Ashby, M., Barmby, P., et al. 2004, ApJS, 154, 39

Fermi-LAT Collaboration. 2012, arXiv:1206.1896

Fichtel, C. E., Simpson, G. A., & Thompson, D. J. 1978, ApJ, 222, 833

Finke, J. D., Razzaque, S., & Dermer, C. D. 2010, ApJ, 712, 238

Finkelstein, S. L., Papovich, C., Ryan, R. E., et al. 2012, ApJ, 758, 93

Finkelstein, S. L., Ryan, Jr., R. E., Papovich, C., et al. 2015a, ApJ, 810, 71

—. 2015b, ApJ, 810, 71

Fixsen, D. J. 2009, ApJ, 707, 916

Fixsen, D. J., Dwek, E., Mather, J. C., Bennett, C. L., & Shafer, R. A. 1998, The Astrophysical Journal, 508, 123

Foreman-Mackey, D., Hogg, D., Lang, D., & Goodman, J. 2013, , 125, 306

Fornengo, N., Lineros, R., Regis, M., & Taoso, M. 2011, Phys. Rev. Lett., 107, 271302

Franceschini, A., & Rodighiero, G. 2017, A&A, 603, A34

Franceschini, A., Rodighiero, G., & Vaccari, M. 2008, A&A, 487, 837

Furlanetto, S. R. 2006, MNRAS, 371, 867

Furniss, A., Williams, D., Danforth, C., et al. 2013, ApJL, 768, L31

Gardner, J., Brown, T., & Ferguson, H. 2000, ApJL, 542, L79

Gaté, F., Biteau, J., Batista, R., et al. 2017, International Cosmic Ray Conference, 301, 623

Ghisellini, G., Righi, C., Costamante, L., & Tavecchio, F. 2017, MNRAS, 469, 255

Ghisellini, G., Della Ceca, R., Volonteri, M., et al. 2010, MNRAS, 405, 387

Giacconi, R., Gursky, H., Paolini, F., & Rossi, B. 1962, Physical Review Letters, 9, 439

Gilmore, R. 2012, MNRAS, 420, 800

Gilmore, R., Somerville, R., Primack, J., & Domínguez, A. 2012, MNRAS, 422, 3189

Gilmore, R. C., Madau, P., Primack, J. R., Somerville, R. S., & Haardt, F. 2009, MNRAS, 399, 1694

Gong, Y., & Cooray, A. 2013, ApJL, 772, L12

Goodman, J., & Weare, J. 2010, Communications in Applied Mathematics and Computational Science, Vol.˜5, No.˜1, p.˜65-80, 2010, 5, 65

Gorjian, V., Wright, E. L., & Chary, R. R. 2000, The Astrophysical Journal, 536, 550

Gould, R., & Schréder, G. 1967a, Physical Review, 155, 1408

—. 1967b, Physical Review, 155, 1404

Greiner, J., Clemens, C., Krühler, T., et al. 2009a, A&A, 498, 89

—. 2009b, A&A, 498, 89

Grogin, N. A., Kocevski, D. D., Faber, S. M., et al. 2011, ApJS, 197, 35

Guiriec, S., Gehrels, N., McEnery, J., Kouveliotou, C., & Hartmann, D. 2017, ApJ, 846, 138

H.˜E.˜S.˜S. Collaboration, Abdalla, H., Abramowski, A., et al. 2017, A&A, 606, A59

Hartmann, D. 2007, in American Institute of Physics Conference Series, Vol. 921, The First GLAST Symposium, ed. S. Ritz, P. Michelson, & C. Meegan, 24–25

Hasinger, G., Miyaji, T., & Schmidt, M. 2005, A&A, 441, 417

Hauser, M., Arendt, R., Kelsall, T., et al. 1998, ApJ, 508, 25

Hauser, M. G., & Dwek, E. 2001, arXiv:0105539

Hauser, M. G., & Dwek, E. 2001, , 39, 249

Helgason, K., & Kashlinsky, A. 2012a, ApJL, 758, L13

—. 2012b, ApJL, 758, L13

Hopkins, A., & Beacom, J. 2006, ApJ, 651, 142

Horns, D., & Meyer, M. 2012, JCAP, 2, 33

Illingworth, G. D., Magee, D., Oesch, P. A., et al. 2013, ApJS, 209, 6

Inoue, Y., Inoue, S., Kobayashi, M. A. R., et al. 2013, ApJ, 768, 197

Inoue, Y., Inoue, S., Kobayashi, M. A. R., et al. 2013, ApJ, 768, 197

Inoue, Y., Tanaka, Y., Madejski, G., & Domínguez, A. 2014, ApJL, 781, L35

Ishigaki, M., Kawamata, R., Ouchi, M., et al. 2018, ApJ, 854, 73

Jenke, P. A., Linares, M., Connaughton, V., et al. 2016, The Astrophysical Journal, 826, 228

Kashlinsky, A. 2005, , 409, 361

Kashlinsky, A. 2005, , 409, 361

Kashlinsky, A. 2005, The Astrophysical Journal Letters, 633, L5

Kashlinsky, A., Arendt, R., Ashby, M., et al. 2012, ApJ, 753, 63

Kashlinsky, A., Arendt, R., Mather, J., & Moseley, S. 2005, , 438, 45

Kaur, A., Ajello, M., Marchesi, S., & Omodei, N. 2019, The Astrophysical Journal, 871, 94

Keenan, R., Barger, A., Cowie, L., & Wang, W.-H. 2010, ApJ, 723, 40

Kelsall, T., Weiland, J. L., Franz, B. A., et al. 1998, ApJ, 508, 44

Kennicutt Jr., R. 1998, , 36, 189

Khaire, V., & Srianand, R. 2015, ApJ, 805, 33

—. 2018, arXiv:1801.09693, arXiv:1801.09693

Khaire, V., & Srianand, R. 2018, arXiv e-prints, arXiv:1801.09693

Kistler, M. D., Yüksel, H., Beacom, J. F., Hopkins, A. M., & Wyithe, J. S. B. 2009, ApJL, 705, L104

Kneiske, T. M., Bretz, T., Mannheim, K., & Hartmann, D. H. 2004, A&A, 413, 807

Kneiske, T. M., & Dole, H. 2010, A&A, 515, A19

Kogut, A., Fixsen, D. J., Levin, S. M., et al. 2011, The Astrophysical Journal, 734, 4

Kumar, P., & Barniol Duran, R. 2009, MNRAS, 400, L75

—. 2010, MNRAS, 409, 226

Lagache, G., & Puget, J. L. 2000, A&A, 355, 17

Landoni, M., Paiano, S., Falomo, R., Scarpa, R., & Treves, A. 2018, ApJ, 861, 130

Landoni, M., Massaro, F., Paggi, A., et al. 2015, , 149, 163

Levenson, L. R., & Wright, E. L. 2008, The Astrophysical Journal, 683, 585

Levenson, L. R., Wright, E. L., & Johnson, B. D. 2007, The Astrophysical Journal, 666, 34

Livermore, R. C., Finkelstein, S. L., & Lotz, J. M. 2017, ApJ, 835, 113

Lotz, J. M., Koekemoer, A., Coe, D., et al. 2017, ApJ, 837, 97

Lusso, E., Worseck, G., Hennawi, J. F., et al. 2015, MNRAS, 449, 4204

Madau, P. 1999, in American Institute of Physics Conference Series, Vol. 470, After the Dark Ages: When Galaxies were Young (the Universe at 2 < Z < 5), ed. S. Holt & E. Smith, 299–311

Madau, P., & Dickinson, M. 2014, , 52, 415

Madau, P., Ferguson, H., Dickinson, M., et al. 1996, MNRAS, 283, 1388

Madau, P., & Haardt, F. 2015, ApJL, 813, L8

Madau, P., & Pozzetti, L. 2000, MNRAS, 312, L9

Marchesi, S., Kaur, A., & Ajello, M. 2018, ArXiv e-prints, arXiv:1809.05486

Marchesini, E., Masetti, N., Chavushyan, V., et al. 2016, A&A, 596, A10

Marshall, F., Boldt, E., Holt, S., et al. 1980, ApJ, 235, 4

Massaro, F., Masetti, N., D'Abrusco, R., Paggi, A., & Funk, S. 2014, , 148, 66

Massey, P. 1997

Matsumoto, T., Tsumura, K., Matsuoka, Y., & Pyo, J. 2018, , 156, 86

Matsumoto, T., Matsuura, S., Murakami, H., et al. 2005, ApJ, 626, 31

Matsuoka, Y., Ienaka, N., Kawara, K., & Oyabu, S. 2011, ApJ, 736, 119

Matsuura, S., Arai, T., Bock, J., et al. 2017, ApJ, 839, 7

Mattila, K., Väisänen, P., Lehtinen, K., von Appen-Schnur, G., & Leinert, C. 2017, MNRAS, 470, 2152

Mattila, K., & VÃisÃnen, P. 2019, Contemporary Physics, 0, 1

Mattox, J. R., Bertsch, D. L., Chiang, J., et al. 1996, ApJ, 461, 396

Maurer, A., Raue, M., Kneiske, T., et al. 2012, ApJ, 745, 166

Mazin, D., Domínguez, A., Fallah Ramazani, V., et al. 2017, in American Institute of Physics Conference Series, Vol. 1792, 6th International Symposium on High Energy Gamma-Ray Astronomy, 50037

Mazin, D., & Raue, M. 2007, A&A, 471, 439

Mazin, D., Raue, M., Behera, B., et al. 2013, Astroparticle Physics, 43, 241

McLure, R. J., Dunlop, J. S., Bowler, R. A. A., et al. 2013, MNRAS, 432, 2696

Meegan, C., Lichti, G., Bhat, P. N., et al. 2009, ApJ, 702, 791

Meyer, M., Horns, D., & Zechlin, H. S. 2010, A&A, 523, A2

Meyer, M., Raue, M., Mazin, D., & Horns, D. 2012, A&A, 542, A59

Miville-Deschênes, M.-A., Lagache, G., & Puget, J.-L. 2002, A&A, 393, 749

Nikishov, A. 1961, Sov. Phys. JETP, 14, 393? 394

Nikishov, A. 1962, JETP, 14, 393

Oesch, P. A., Brammer, G., van Dokkum, P. G., et al. 2016, ApJ, 819, 129

Orr, M. 2011, International Cosmic Ray Conference, 8, 121

Padovani, P. 1992, Monthly Notices of the Royal Astronomical Society, 257, 404

Paggi, A., Milisavljevic, D., Masetti, N., et al. 2014, , 147, 112

Paiano, S., Falomo, R., Franceschini, A., Treves, A., & Scarpa, R. 2017, ArXiv e-prints, arXiv:1711.05476

Park, N. 2018, arXiv e-prints, arXiv:1808.10495

Peña-Herazo, H., Marchesini, E., Álvarez Crespo, N., et al. 2017, , 362, 228

Penzias, A. A., & Wilson, R. W. 1965, ApJ, 142, 419

Planck, Ade, P., Aghanim, N., Arnaud, M., et al. 2015, ArXiv:1502.01589, arXiv:1502.01589

Planck Collaboration, Ade, P., Aghanim, N., et al. 2016, A&A, 594, A13

Primack, J., Bullock, J., & Somerville, R. 2005, in American Institute of Physics Conference Series, Vol. 745, High Energy Gamma-Ray Astronomy, ed. F.˜A.˜Aharonian, H.˜J.˜Völk, & D.˜Horns, 23–33

Raue, M., Kneiske, T., & Mazin, D. 2009, A&A, 498, 25

Raue, M., & Meyer, M. 2012, ApJ, 426, 1097

Razzaque, S., Dermer, C. D., & Finke, J. D. 2009, ApJ, 697, 483

Reddy, N. A., & Steidel, C. C. 2009, ApJ, 692, 778

Ricci, F., Massaro, F., Landoni, M., et al. 2015, , 149, 160

Roberts, O., Fitzpatrick, G., Stanbro, M., et al. 2018, Journal of Geophysical Research: Space Physics, 123, doi:10.1029/2017JA024837

Robertson, B. E., Ellis, R. S., Furlanetto, S. R., & Dunlop, J. S. 2015, ApJL, 802, L19

Robotham, A. S. G., & Driver, S. P. 2011, MNRAS, 413, 2570

Salpeter, E. E. 1955, ApJ, 121, 161

Schiminovich, D., Ilbert, O., Arnouts, S., et al. 2005, ApJL, 619, L47

Schlafly, E., & Finkbeiner, D. 2011, ApJ, 737, 103

Scully, S., Malkan, M., & Stecker, F. 2014, ApJ, 784, 138

Scully, S. T., Malkan, M. A., & Stecker, F. W. 2014, ApJ, 784, 138

Shaw, M., Romani, R., Cotter, G., et al. 2013, ApJ, 764, 135

Stecker, F., de Jager, O., & Salamon, M. 1992, ApJL, 390, L49

Stecker, F., Malkan, M., & Scully, S. 2006, ApJ, 648, 774

—. 2012, ApJ, 761, 128

Stecker, F., Scully, S., & Malkan, M. 2016, ApJ, 827, 6

Stecker, F. W. 1971, Cosmic gamma rays, Vol. 249 (NASA)

Strong, A., Moskalenko, I., & Reimer, O. 2004, ApJ, 613, 956

Takeuchi, T. T., Buat, V., & Burgarella, D. 2005, A&A, 440, L17

Tam, P.-H. T., Tang, Q.-W., Hou, S.-J., Liu, R.-Y., & Wang, X.-Y. 2013, The Astrophysical Journal Letters, 771, L13

Tang, Q.-W., Peng, F.-K., Wang, X.-Y., & Tam, P.-H. 2015, ApJ, 806, 194

The Fermi-LAT Collaboration. 2018, Science, 362, 1031

Thompson, D. 2018, Galaxies, 6, 117

Tody, D. 1986, in , Vol. 627, Instrumentation in astronomy VI, ed. D. Crawford, 733

Tramacere, A., Giommi, P., Perri, M., Verrecchia, F., & Tosti, G. 2009, A&A, 501, 879

Tramacere, A., Massaro, E., & Taylor, A. M. 2011, ApJ, 739, 66

Treister, E., Urry, C., & Virani, S. 2009, ApJ, 696, 110

Tresse, L., Ilbert, O., Zucca, E., et al. 2007, A&A, 472, 403

Ueda, Y., Akiyama, M., Hasinger, G., Miyaji, T., & Watson, M. G. 2014, The Astrophysical Journal, 786, 104

Urry, C., & Padovani, P. 1995, , 107, 803

Vianello, G., Omodei, N., & collaboration, F. 2015, ArXiv e-prints, arXiv:1502.03122

Vianello, G., Omodei, N., & Fermi LAT Collaboration. 2016, in American Astronomical Society Meeting Abstracts, Vol. 227, American Astronomical Society Meeting Abstracts, 416.01

Voyer, E., Gardner, J., Teplitz, H., Siana, B., & de Mello, D. 2011, ApJ, 736, 80

Wang, X.-Y., He, H.-N., Li, Z., Wu, X.-F., & Dai, Z.-G. 2010, The Astrophysical Journal, 712, 1232

Worsley, M., Fabian, A., Bauer, F., et al. 2005, MNRAS, 357, 1281

Wright, E. L. 2001, The Astrophysical Journal, 553, 538

Wright, E. L. 2004, NAR, 48, 465

Wright, E. L., & Reese, E. D. 2000, ApJ, 545, 43

Wyder, T. K., Treyer, M. A., Milliard, B., et al. 2005, ApJL, 619, L15

Xu, C., Donas, J., Arnouts, S., et al. 2005, ApJL, 619, L11

Yoshida, M., Shimasaku, K., Kashikawa, N., et al. 2006, ApJ, 653, 988

Yu, Hoi-Fung, Preece, Robert D., Greiner, Jochen, et al. 2016, A&A, 588, A135

Zemcov, M., Arai, T., Battle, J., et al. 2013, ApJS, 207, 31

Zemcov, M., Smidt, J., Arai, T., et al. 2014, Science, 346, 732

Zemcov, M., Smidt, J., Arai, T., et al. 2014, Science, 346, 732

Zhang, B.-B., Zhang, B., Liang, E.-W., et al. 2011, ApJ, 730, 141